ASSESSMENT OF POROSITY-PERMEABILITY VARIATION ON THE
RESPONSE OF SANDY SOILS VIA HYPOPLASTICITY MODEL

A THESIS SUBMITTED TO
THE GRADUATE SCHOOL OF NATURAL AND APPLIED SCIENCES
OF
MIDDLE EAST TECHNICAL UNIVERSITY

BY

HILMI BAYRAKTAROĞLU

IN PARTIAL FULFILLMENT OF THE REQUIREMENTS
FOR
THE DEGREE OF MASTER OF SCIENCE
IN
CIVIL ENGINEERING

JUNE 2019

Approval of the thesis:

ASSESSMENT OF POROSITY-PERMEABILITY VARIATION ON THE RESPONSE OF SANDY SOILS VIA HYPOPLASTICITY MODEL

submitted by **HILMI BAYRAKTAROĞLU** in partial fulfillment of the requirements for the degree of **Master of Science in Civil Engineering Department, Middle East Technical University** by,

Prof. Dr. Halil Kalıpçılar
Dean, Graduate School of **Natural and Applied Sciences**   _____

Prof. Dr. Ahmet Türer
Head of Department, **Civil Engineering**   _____

Assoc. Prof. Dr. Nejan Huvaj Sarıhan
Supervisor, **Civil Engineering, METU**   _____

Assoc. Prof. Dr. H. Ercan Taşan
Co-Supervisor, **Visiting Scholar Civil Engineering, METU**   _____

Examining Committee Members:

Prof. Dr. Erdal Çokça
Civil Engineering, METU   _____

Assoc. Prof. Dr. Nejan Huvaj Sarıhan
Civil Engineering, METU   _____

Prof. Dr. Kemal Önder Çetin
Civil Engineering, METU   _____

Assoc. Prof. Dr. Berna Unutmaz
Civil Engineering, Hacettepe University   _____

Assist. Prof. Dr. Salih Tileylioğlu
Civil Engineering, Çankaya University   _____

Date: 21.06.2019

I hereby declare that all information in this document has been obtained and presented in accordance with academic rules and ethical conduct. I also declare that, as required by these rules and conduct, I have fully cited and referenced all material and results that are not original to this work.

Name, Surname: Hilmi Bayraktaroğlu

Signature:

iv

ABSTRACT

ASSESSMENT OF POROSITY-PERMEABILITY VARIATION ON THE RESPONSE OF SANDY SOILS VIA HYPOPLASTICITY MODEL

Bayraktaroğlu, Hilmi
Master of Science, Civil Engineering
Supervisor: Assoc. Prof. Dr. Nejan Huvaj Sarıhan
Co-Supervisor: Assoc. Prof. Dr. H. Ercan Taşan

June 2019, 134 pages

Hydro-mechanical characteristic of the saturated sands is highly influenced by their porosity and permeability. During loading, unloading and reloading compaction of sands, loosening and re-compaction take place, which leads to changes in pore volume and permeability. In order to accurately simulate these real-life conditions, new variables and phenomena should be investigated using sophisticated numerical tools and equipment.

In this study, the behavior of water saturated sands subjected to cyclic and dynamic loading is analyzed numerically and experimentally. For the finite element analyses, a three-dimensional fully coupled two-phase finite element is developed and implemented on the basis of a two-phase model in order to consider the pore water pressure development in saturated sands. In addition, an extended hypoplastic constitutive model is used to describe the material behavior of sandy soils. The porosity-permeability variation is taken into account by implementation of Kozeny-Carman relationship. Using the experimental test results both performed in laboratory and documented in the literature, the influence of porosity-permeability variation on the mechanical behavior of sandy soils is investigated by comparing the strain and pore pressure accumulations. The necessity of the consideration of porosity-

permeability variation for realistic modeling of the cyclic and dynamic behavior of saturated sandy soils is assessed.

The laboratory experiments and numerical methods required to determine thirteen parameters of the hypoplastic constitutive model are explained systematically. The hypoplastic material parameters of a sandy soil is determined and then compared with the recommended parameters available in the literature for the same type of soil. In addition, hypoplastic model parameters of various sands that are commonly used in the modeling of the soil under dynamic loading are presented. This thesis will contribute to researchers working on the numerical modeling of material behavior using finite element method in geotechnical engineering.

Keywords: Porosity-permeability relationship, Hypoplasticity, Two-phase model, Finite element method, Laboratory experiments

ÖZ

BOŞLUK ORANI-GEÇİRİMLİLİK İLİŞKİSİNİN KUMLU ZEMİN DAVRANIŞINA ETKİSİNİN HİPOPLASTİSİTE MODELİ İLE DEĞERLENDİRİLMESİ

Bayraktaroğlu, Hilmi
Yüksek Lisans, İnşaat Mühendisliği
Tez Danışmanı: Doç. Dr. Nejan Huvaj Sarıhan
Ortak Tez Danışmanı: Doç. Dr. H. Ercan Taşan
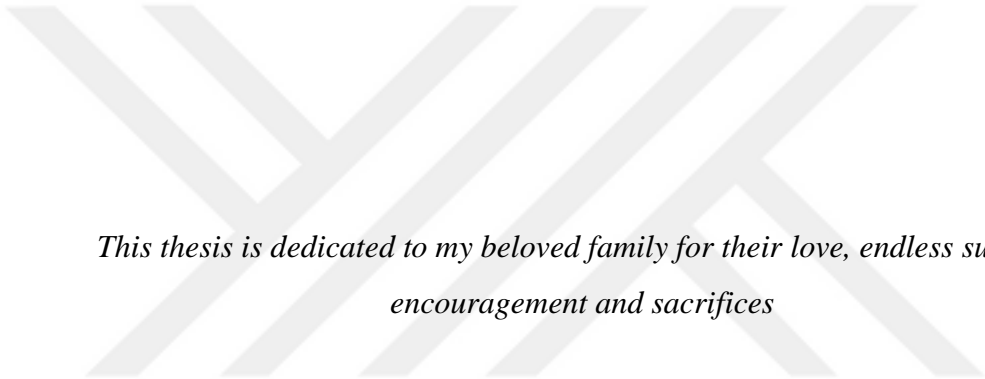
Haziran 2019, 134 sayfa

Suya doygun kumların hidromekanik davranışları zeminin gözeneklilik yapısı ve geçirimlilik özelliklerinden büyük ölçüde etkilenmektedir. Yükleme ve boşaltmanın birbirini takip ettiği deformasyon eğrilerinde kumlar sürekli olarak yumuşama ve sıkışmaya maruz kalırlar. Maruz kalınan yükler sonucu değişen boşluk hacimleri zeminin geçirgenlik katsayısını değiştirmektedir. Bahsedilen gerçek yaşam koşullarını doğru bir şekilde simüle etmek için, yeni değişkenlerin ve kavramların kullanıldığı gelişmiş nümerik modeller ve ekipmanlar kullanılmalıdır.

Bu çalışmada, suya doygun kumlu zeminlerin tekrarlı ve dinamik yüklemeler altındaki davranışı nümerik ve deneysel yöntemler kullanılarak analiz edilmiştir. Üç boyutlu sonlu elemanlar analizlerinde, aşırı boşluk suyu basıncı değişimleri iki fazlı modele dayanan üç boyutlu elemanlar yardımıyla incelenmiştir. Buna ek olarak zemin davranışının modellenmesi için genişletilmiş hipoplastik bünye modeli kullanılmıştır. Geçirimliliğin gözenekliliğe bağlı değişimi Kozeny-Carman ilişkisinin modele tanımlanmasıyla elde edilmiştir. Gerçekleştirilen deneyler ile birlikte, literatürde mevcut deneysel sonuçlarda kullanılarak gözeneklilik-geçirimlilik arasındaki ilişkinin kumlu zeminlerin mekanik davranışı üzerindeki etkisi, deformasyon ve boşluk suyu

basınçları karşılaştırılarak incelenmiştir. Suya doygun kumlu zeminlerin tekrarlı ve dinamik yük altındaki davranışlarının gerçekçi olarak modellenmesi sırasında gözeneklilik-geçirimlilik değişimlerinin göz önünde bulundurulması gerekliliği değerlendirilmiştir.

Bu çalışmada hipoplastik bünye modelinin on üç parametresinin belirlenmesi için gerekli laboratuvar deneyleri ve yöntemler sistematik bir şekilde açıklanmıştır. Kumlu bir zeminin model parametreleri belirlenmiş ve literatürde aynı zemin tipi için önerilen malzeme parametre değer aralıklarıyla karşılaştırılmıştır. Ayrıca dinamik yük etkisi altındaki zeminlerin modellenmesinde kullanılmış olan çeşitli kumların hipoplastik bünye model parametreleri de sunulmaktadır. Bu çalışmanın, geoteknik mühendisliğinde sonlu elemanlar yöntemi ile malzeme davranışının modellenmesi üzerine çalışan araştırmacılar için katkı sağlayacağı düşünülmektedir.

Anahtar Kelimeler: Gözeneklilik-geçirimlilik ilişkisi, Hipoplastisite, İki-fazlı model, Sonlu elemanlar metodu, Laboratuvar deneyleri

This thesis is dedicated to my beloved family for their love, endless support, encouragement and sacrifices

ACKNOWLEDGMENTS

TABLE OF CONTENTS

LIST OF TABLES

TABLES

LIST OF FIGURES

FIGURES

CHAPTER 1

INTRODUCTION

The application of numerical tools continues to increase within the geotechnical engineering community. New challenges in geotechnical engineering, increasing complexity and constraints both in time and space and difficult soil conditions force geotechnical engineers to go beyond the realm of their previous experience and knowledge. Numerical modeling represents an ideal approach to managing and addressing these challenges and aids decision makers in selecting among alternatives. It is extremely important to understand the mechanical behavior and possible failure mechanisms of geotechnical structures. Simulations and modeling help us to understand these mechanisms and provide safe designs by taking into account different loading scenarios to predict anticipating problems that can occur during the lifetime of a project. These virtual experiments enable us to perform complex deformation, soil-structure interaction and liquefaction analyses which are hard or impossible to do with analytical methods.

A constitutive model basically refers to a mechanism describing the relationship between the stress and the strain in a material. Considering the nature of the soil, numerical simulation of the mechanical behavior of complex coupled geotechnical problems require sophisticated constitutive models (Vakili et al. 2013). That is why selecting an appropriate constitutive model is the key for the accuracy of the numerical analyses. Type of the material, multi-phase calculations, loading scenario, complexity of the geometry and boundary conditions are some of the main parameters which should be considered while selecting a suitable material model. The knowledge of the capabilities, advantages and disadvantages of the selected material model enables us to determine limits where the accurate simulations can be performed.

1.1. Problem Statement

The finite element method (FEM) is one of the most commonly used numerical technique for simulating the mechanical behavior of soil and designing engineering problems. The FEM works on the principle of divide and rule which means transforming a physical system having infinite unknowns into small finite elements having a finite number of unknowns. These unknowns are called as degree of freedoms. Instead of solving the problem for the entire body in one operation, the solutions are formulated for each member and combined to obtain the solution for the entire body. In this regard, the analysis of a model is a mathematical description of the physical system where the validity of the calculations mainly depends on the material model used to describe the mechanical behavior, the applicable boundary conditions and assumptions implemented into the model to simplify the complexity of the physical system. Today, in order to overcome the effects of these simplifications and idealizations, predefined safety factors are used which most of the time lead us to overly safe designs and uneconomical solutions.

One of the commonly made assumptions in geotechnical engineering is related with the permeability of the soil which is one of the most important parameters controlling the hydromechanical behavior of the coupled two-phase systems, especially under cyclic and dynamic loading conditions. Because of the relatively high permeable characteristics of the sandy soils, the pore water pressure development observed during the deformation process dissipates very quickly. That is why the time dependent settlements are generally not considered for this type of soils. Based on this reasonable idealization, the effect of the deformation dependent porosity change on the permeability of the soil is ignored. In other words, together with the settlements and all the other deformations, permeability is also not considered as a time dependent variable and instead a constant value is assigned to idealize the dissipation mechanism of the two-phase sandy soil system.

The behavior of soils under cyclic and dynamic loading is recognized as one of the most challenging fields of soil mechanics due to the inherently strong coupling effects inside the two-phase physical system and lack of reliable constitutive models that realistically capture the mechanical behavior of soil under cyclic loading (Niemunis et al. 2005; Tang and Hededal 2014). Saturated soils under cyclic and dynamic loading conditions tend to build-up of pore pressure, shear strength degradation and softening (Martin et al. 1975; Andersen 2007; Cary and Zapata 2016). The accumulation of irreversible strains in the soil due to cyclic and dynamic loading leads to pore pressure development which has to be considered in the design of geotechnical structures. So that understanding the factors affecting the development process of pore pressure accumulation is critical for a proper description of the soil behavior under cyclic and dynamic loading.

As geotechnical engineers, we always assume that there is no time dependent settlements in sandy soils. This assumption is made by comparing the deformation process of sand and clay. In clayey soils consolidation may take years however in sandy soils it takes seconds, minutes or hours depending on the grain size distribution and loading type. Step by step small rate loading may not create a difference but in case of high frequency loading (e.g. earthquake) the hydro-mechanical behavior of the soil becomes much more complex that we cannot handle with this simplified permeability assumptions anymore. For example, for a liquefaction analysis, we have to consider the instantly changing, dynamic hydro-mechanical behavior of the soil. Under different types of structural and environmental loading, interconnected solid particles with intermediate pores filled with fluid may lead to built-up of pore pressure, shear strength degradation and yielding material softening. Therefore, it creates risks on the stability of the structures and foundation systems and difficulties during design process. The pore pressure accumulation caused by dynamic loading conditions should be investigated carefully in design of foundation systems. Especially, for the structures under heavy cyclic and dynamic loadings.

1.2. Research Objectives

In this thesis, complex drainage mechanism of the fully saturated sandy soils (two-phase system) is investigated and the effects of it on the mechanical behavior, especially under cyclic and dynamic loading conditions, are determined by using numerical and experimental simulations.

It is acknowledged that the compressibility and the permeability are two coupled factors that affect the hydro-mechanical behavior and overall response of the saturated soils (Liang et al. 2017). During the deformation, porosity of the soil changes and depending on that change, permeability of the soil also changes (Di and Sato 2003). One of the fundamental objectives of this thesis is to identify the geotechnical engineering problems where the porosity-permeability variation is considered necessary for a sufficiently accurate description of the complex deformation mechanisms such as compression, swelling or even liquefaction (Bayraktaroglu and Taşan 2018).

In order to achieve the above-mentioned objectives following steps are taken:

- Hypoplastic constitutive model with intergranular strain concept is implemented into the ANSYS to describe the stress-strain behavior of the soil.
- A sophisticated numerical model based on the three-dimensional fully coupled two-phase finite element is developed for the saturated sands.
- A comparison among the variety of porosity-permeability relationships available in the literature is carried out.
- The Kozeny-Carman relationship is selected and then implemented into the model to investigate the effect of porosity variation on the hydromechanical behavior of the saturated soil.
- The accuracy of the improved model is verified using the experimental data both obtained from literature and performed in the laboratory.
- The necessity of the porosity-permeability relationship is discussed for different type of geotechnical problems.

1.3. Scope

This thesis investigates the effect of permeability variation on the mechanical behavior of saturated sandy soils. Unlike the current application, the stress and the strain relationship is investigated by taking into account a porosity dependent permeability equation. The theoretical and experimental background of these equations is explained in Chapter 2. Moreover, a summary of the constitutive models used to simulate the mechanical behavior of the sandy soils are presented and two-phase model which is required for a coupled analysis of the fully saturated system is discussed within the same chapter. In Chapter 3, the accuracy of the finite element model developed for the predefined problem is verified by using element tests available in the literature and a laboratory experiment carried out in our department. Three different real-world case studies including an earthquake induced dyke centrifuge test and a jacket type gravity-based offshore wind turbine foundation subjected to cyclic loading are numerically modelled in Chapter 4. Last of all, in Chapter 5, based on the numerical results, the necessity of the consideration of porosity-permeability variation for the realistic modelling of geotechnical structures subjected to cyclic and dynamic loading is assessed. Conclusions and suggestions for future studies are presented.

1.4. Notation and Tensor Operations

In this thesis, the notations of the well known continuum mechanics books are adopted (Malvern 1969), (Truesdell and Noll 1965). Scalars are indicated by using regular symbols and characters (e.g. ε, F, α). Vectors and second-order tensors (rank 2) are distinguished by bold typeface (e.g. $\mathbf{N}$, $\mathbf{T}$, $\mathbf{v}$). Calligraphy letter is used for the fourth-order tensors (e.g. $\mathcal{L}$, $\mathcal{D}$). Kronecker's symbol, δ_{ij} equals to 1 for $i = j$ and zero otherwise. Permutation symbol, $e_{ijk} = 1$ for $\{i, j, k\} \subset \{\{1,2,3\}, \{2,3,1\}, \{3,1,2\}\}$ and $e_{ijk} = -1$ for $\{i, j, k\} \subset \{\{1,3,2\}, \{2,1,3\}, \{3,2,1\}\}$, $e_{ijk} = 0$ for any other scenario.

Proportional tensors are indicated by using tilde (e.g. $\mathbf{T} \sim \mathbf{D}$) and normalized tensors denoted by an arrow (e.g. $\vec{\mathbf{D}}$). The unit tensor of second and fourth order are denoted by $\mathbf{1}$ (or δ_{ij}) and $\boldsymbol{I}$ (or $I_{ijkl} = \delta_{ik}\delta_{jl}$) respectively.

The following tensor operations are used throughout this thesis:

Table 1.1. *Tensor operations*

Operations	Mathematical Representation	Explanations
$\mathbf{a} \cdot \mathbf{b}$	$a_i b_i$	Single contraction (multiplication with one dummy index)
$\mathbf{c} \cdot \mathbf{d}$	$c_{ij} d_{jk}$	
$\mathbf{A} : \mathbf{B}$	$A_{ij} B_{ij}$	Double contraction (multiplication with two dummy indices)
$\|\mathbf{D}\|$	$\sqrt{D_{ij} D_{ij}}$	Euclidean norm (or L_2 norm)
$\mathbf{a} \otimes \mathbf{b}$	$a_{ij} b_{kl}$	Dyadic multiplication
$(\mathbf{a} \times \mathbf{b})_i$	$e_{ijk} a_j b_k$	Vector multiplication
$\nabla \mathbf{a}$	$a_{i,j}$	Gradient
$\nabla \cdot \mathbf{a}$	$a_{ij,i}$	Divergence
$\nabla^s \mathbf{a}$	$^1/_2 \left(a_{i,j} + a_{j,i} \right)$	Symmetric part of the gradient
$\vec{\mathbf{A}} = \dfrac{\mathbf{A}}{\|\mathbf{A}\|}$		Normalized tensors
$\mathrm{tr}(\mathbf{a})$	a_{ii}	Trace
$\mathrm{tr}(\mathbf{A}^{\mathrm{T}} \cdot \mathbf{B})$	$A_{ij} B_{ij}$	Relation between trace and double contraction
$\mathrm{dev}(\mathbf{c})$	$c_{ij} - \mathrm{tr}(\mathbf{c})\delta_{ij}$	Deviator
$\dot{\mathbf{c}}$	$c_{ij,t}$ or $\partial \mathbf{c}/\partial t$	Time derivative

CHAPTER 2

RESEARCH BACKGROUND

Theoretical modeling of the geotechnical structures requires well-defined constitutive models that can capture the non-linear behavior of the soil. The formulation of the stress-strain response of the soil in these models is the key to successfully predict the mechanical behavior of the geotechnical structures (Carter 2006). However, it is a fact that none of the constitutive models can fully represent all aspects of the behavior of the soil but should consider some important features (Herle 2008). There are plenty of constitutive models available in the literature from very basic linear elastic models to complex plastic models and unfortunately, the important details and idealizations considered while developing these models are often poorly understood or ignored by the researchers and geotechnical engineers (Li and Borja 2005). In this chapter development of a complex constitutive model (both formulation and parameter determination), hypoplasticity, will be presented and prediction capabilities, application scope, merits and shortcoming of the model will be discussed.

In this thesis, fully saturated sandy soil is considered as a two-phase mixture consisting of solid grains and fluid occupying the pores in the skeleton. Computational procedure and formulations required for the coupled finite element analysis of the two-phase model are emphasized.

Using the permeability relationships developed for porous media available in the literature, effects of the permeability variation on the mechanical behavior of the saturated sandy soils are investigated under various loading conditions. The experimental and theoretical background of the selected relationships is discussed. The complexity of the fluid flow through the porous media is described together with the limitations of it. Numerical implementation of the porosity-permeability relationship into the two-phase model is formulated in order to accurately simulate the geotechnical engineering problems.

2.1. Constitutive Models

Prediction of the deformation mechanism of soil has always been one of the greatest interests in geotechnical engineering. The mathematical description of this mechanism is idealized by using constitutive models. In other words, the relationship between the stress and strain components are linked by using constitutive equations. Role of these equations and numerical modeling within geotechnical engineering is very well illustrated by (Burland 1987) and (Barbour and Krahn 2004) as shown in Figure 2.1.
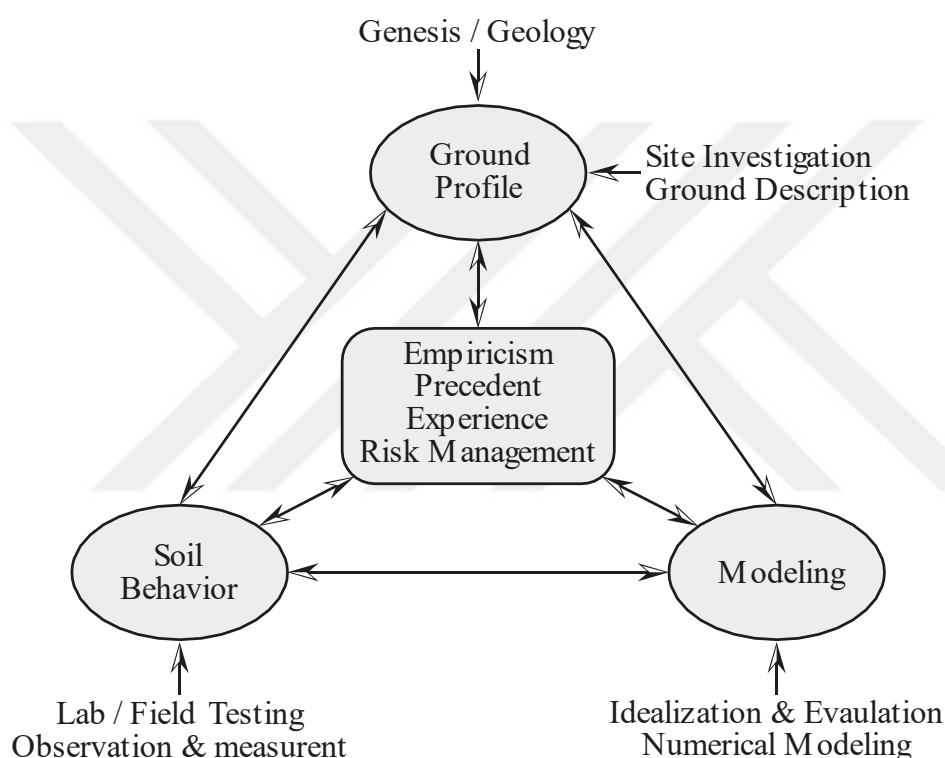
Figure 2.1. Modified Burland triangle

According to Professor Burland geotechnical engineering practice consists of three main activities. By linking these three activities which are the most important aspects of geotechnical engineering, what is called Burland Triangle is obtained. Burland triangle perfectly illustrates the relationship between the different aspects of geotechnical engineering and summarizes the considerations we need to keep in mind while performing numerical simulations and using various constitutive models. Figure also describes constitutive models as an idealized mathematical system which is

obtained from observation of site conditions and understanding of soil behavior through laboratory and field tests. On the other hand, understanding of these complex physical systems and predicting soil behavior require some conceptual knowledge of constitutive modeling (Carter 2006).

The continuum models developed for the numerical investigation of soil behavior cover a large spectrum from very simple elastic and perfectly plastic models to sophisticated models with several yield surfaces, including complex hardening and softening laws (Hofstetter et al. 2016). An example classification that shows the hierarchical relationship between the widely used constitutive models is given in Figure 2.2.
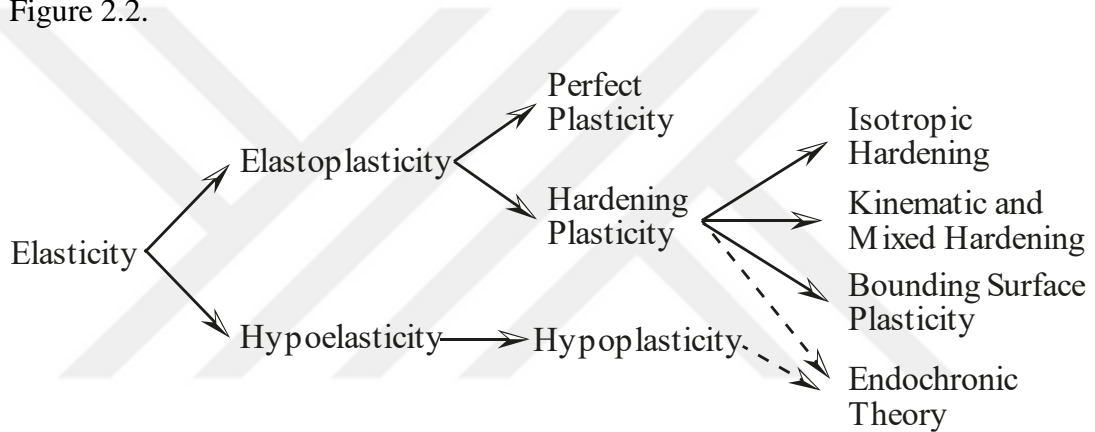
Figure 2.2. Example of a classification of constitutive models (Herle, 2008)

The selection of the constitutive model depends on the scope of the problem and the level of accuracy planning to be achieved. Even though it is mathematically possible to model a highly nonlinear system by using a linear material model, the results obtained at the end of the simulation will not be reliable and will not represent the real respond of the physical system, especially in case of large deformations. That is why the constitutive models used to predict the actual deformations should be selected very carefully in geotechnical engineering due to highly nonlinear, plastic and complex nature of the soil.

Today's increasing computational power enables and promotes engineer to simulate complex physical systems by using advanced highly accurate constitutive models.

However, together with the increasing complexity, it becomes more difficult to understand conceptual background and control the limitations of these mathematical expressions (Runesson 2006) and (Herle 2008).

In this thesis, elasticity has been used for the numerical validation of the two-phase element and determination of the initial conditions. In addition to the elasticity, hypoplasticity has been used for the numerical simulation of the mechanical behavior of the sandy soils. A detailed description of the constitutive models used in this thesis with the finite element analyses, procedure of parameter determination and calibration have been presented in the following sections.

2.1.1. Linear Elasticity

Linear elasticity is one of the simplest constitutive law which describes the material behavior using a linear relationship between stress, $\boldsymbol{\sigma}$ and strain, $\boldsymbol{\varepsilon}$ components. In elasticity, the stress-strain relationship at a point is considered as rate independent (sequence of operations and history of loading do not affect the current stress-strain state). The most general linear relation among all the components of the stress and strain tensor is defined by generalized Hooke's law as shown in the Equation (2.1),

$$\boldsymbol{\sigma} = \boldsymbol{C} \cdot \boldsymbol{\varepsilon} \tag{2.1}$$

For an elastic isotropic material, elasticity or stiffness tensor, $\boldsymbol{C}$ can be obtained by taking inverse of the compliance tensor,

$$\boldsymbol{C} = \frac{E}{(1+\nu)(1-2\nu)} \begin{bmatrix} 1-\nu & \nu & \nu & 0 & 0 & 0 \\ \nu & 1-\nu & \nu & 0 & 0 & 0 \\ \nu & \nu & 1-\nu & 0 & 0 & 0 \\ 0 & 0 & 0 & \frac{1-2\nu}{2} & 0 & 0 \\ 0 & 0 & 0 & 0 & \frac{1-2\nu}{2} & 0 \\ 0 & 0 & 0 & 0 & 0 & \frac{1-2\nu}{2} \end{bmatrix} \tag{2.2}$$

where E is Young's modulus and ν is Poisson's ratio.

The linear elasticity turns out to be an excellent predictor for the investigation of small strain deformations and can be used for the loose sands at small-strain level (Nader 2012). Considering the path dependent, nonlinear and inelastic response of the soil, the linear behavior can be considered valid only for the very small deformations with a strain value less than 10^{-5} (Jardine et al. 1984; Niemunis and Herle 1997).

In this thesis, linear elastic material model is used for the verification of the two-phase model by comparing the numerical result with the analytical solution. Even though the grain particles are considered as incompressible, at least under the loads geotechnical engineers dealing with, a linear elastic material model employed for consideration of grain compressibility. Finally, and most importantly, linear elasticity is used to calculate the initial stress state of the soil which is required for the initiation of the more complex hypoplastic constitutive model.

2.1.2. Hypoplasticity

The stress-strain behavior of the cohesionless soils can be realistically modeled by using an incrementally non-linear constitutive model, hypoplasticity. Unlike the elastoplastic models, the hypoplasticity does not distinguish between the elastic and plastic deformation and does not contain any yield surface, plastic potential, flow and hardening rule (Kolymbas 1985; Bauer, Calibration of a comprehensive hypoplastic model for granular materials 1996). In addition, hypoplasticity provides an alternative mathematical description for granular soils by means of a single tensorial equation. In other words, switch functions that are used in elastoplastic models to differentiate the loading and unloading paths are replaced by a single nonlinear tensorial equation that can capture the dissipative behavior, plastic flow and nonlinearity with a more comprehensible and easier way (Kolymbas 1993; Chatra and Dadagoudar 2010). The model is suitable to consider the effects of stress level (barotropy), densification (pyknotropy), dilatancy and material softening which is observable during shearing of granular materials (Bayraktaroglu and Taşan 2018; Gudehus, A comprehensive

11

constitutive equation for granular materials 1996; Bauer, Calibration of a comprehensive hypoplastic model for granular materials 1996).

The effects of deformation direction and soil state on stiffness, dilatation, shrinkage and peak friction angle are considered in hypoplastic model. The influence of the stress distributions and unit weight change on the mechanical behavior of the soil is also taken into account.

In hypoplastic model, granular medium (skeleton and pore volume) is considered as a continuum and the state of representative volume is characterized by the current granular effective stress (Cauchy stress), **T** and the void ratio, **e** as shown in Equation (2.8) (Herle and Mayer 2009). Therefore, instead of modeling each grain, which is what discrete element method (DEM) is based on (Yun et al. 2008; Siu and Lee 2004), behavior of the soil is considered in a general manner (macro-scale modeling) in hypoplasticity. This approach enables us to perform efficient and relatively fast numerical analyses especially for the full-scale geotechnical engineering problems such as dams and offshore foundations. Indeed, it would be great to be able to analyze such huge problems using more detailed micro-scale modeling with DEM and predict the mechanical behavior from granulometric properties. But, considering the current computational power of the computers, numerical micro-scale modeling of samples with more than 10^5 particles, which includes the consideration of the deformation path (movement) of each individual grains and their contact forces, is not feasible and far from being practical (Niemunis 2002; Chavez Abril 2017).

Over the years, various hypoplastic formulations have been proposed to model nonlinear stress-strain relationship (stiffness) of the system and all these different versions of the hypoplastic models have been developed over similar tensorial expressions such as $\mathcal{L}$ and **N** as shown in Equation (2.3).

$$\overset{\circ}{\mathbf{T}} = \mathcal{L} : \mathbf{D} + \mathbf{N} \cdot \|\mathbf{D}\| \qquad (2.3)$$

In above given equation, the rate of nonlinear stress propagation (or objective stress rate tensor), $\mathring{\mathbf{T}}$ which is the Jaumann stress rate of the effective stresses $\mathbf{T}$ is formulated using fourth and second order constitutive tensors $\mathcal{L}$ and $\mathbf{N}$. These tensors control the linearity and nonlinearity in strain rate (stretching) tensor, $\mathbf{D}$ respectively (Heeres 2001; Wu et al. 1993). The first term of the Equation (2.3), $\mathcal{L}:\mathbf{D}$ is linear in $\mathbf{D}$ and used to identify the particular case where the soil behavior is hypoelastic; on the other hand, the second term, $\mathbf{N}\cdot\|\mathbf{D}\|$ is nonlinear in $\mathbf{D}$ and responsible from the path dependent deformations. Remember that, the Euclidean norm of strain rate equals to: $\|\mathbf{D}\| = \sqrt{D_{ij}D_{ij}}$ and tensorial double multiplication is denoted by $\mathcal{L}:\mathbf{D} = L_{ijkl}D_{kl}$ (Table 1.1).

Hypoplasticity is a path-dependent and rate-independent constitutive model (Niemunis 2002), that is, rather than the duration of the deformation process, the sequence of deformations is used to formulate the stress response of the granular system. Due to this rate-independency, the first derivative of the $\mathbf{T}$ is positively homogeneous of the first degree with respect to $\mathbf{D}$ as indicated in Equation (2.4) (Kolymbas 1999).

$$h(\mathbf{T}, \mathbf{e}, \lambda\mathbf{D}) = \lambda h(\mathbf{T}, \mathbf{e}, \mathbf{D}) \text{ for } \lambda > 0 \qquad (2.4)$$

The change of stiffness and corresponding effects on nonlinear behavior is controlled by changing the sign of the strain rate, $\mathbf{D}$ (Meißner 2014). Note that, due to the nonlinear nature of the model, Equation (2.5) is not linear in $\mathbf{D}$ which also provides the differentiation of the loading and unloading paths.

$$h(\mathbf{T}, \mathbf{e}, -\mathbf{D}) \neq -h(\mathbf{T}, \mathbf{e}, \mathbf{D}) \qquad (2.5)$$

Hypoplastic model has been developed based on phenomenological and macroscopic approach (Niemunis 2002). Similar to the previously developed phenomenological models, the mathematical formulations describing the stress-strain relationship have been derived from the experimental data obtained from well-defined physical tests and relevant principles of physics (Winde H. P. 2015) and (Runesson 2006). Unlike the data-based empirical models and physics-based analytical models which rely purely

on the fundamental laws of physics (e.g. conservation of mass and energy), phenomenological hypoplastic model relates these two approaches and link them to formulate the mechanical behavior of the soil (Aubram et al. 2015).

Before going into further detail about hypoplasticity, the important assumptions and considerations required to idealize granular system and formulate the stress-strain relationship using hypoplasticity will be given as follows:

- The state of the soil is defined solely by the stress tensor **T** and void ratio **e**.
- The model is defined within the pressure dependent lower and upper void ratio limits (Figure 2.7.
- During the deformation process, each individual grain is considered as mechanically and granulometrically permanent (simple grain skeleton). Deformation of a single grain, (i.e. abrasion or crushing), is ignored. The displacement of the granular system is considered to be the result of the rearrangement of the particles (Herle and Gudehus 1999).
- The formation of the macrovoids which is observed in case of the existence of the voids larger than mean particle size ($e > e_{max}$), Figure 2.3 and formation of clumps and flocculation (especially in the existence of water) are not taken into account in hypoplasticity (Niemunis 2002). For $e > e_{max}$ grain contacts disappear, so that a skeleton no longer exists (Herle and Gudehus 1999).
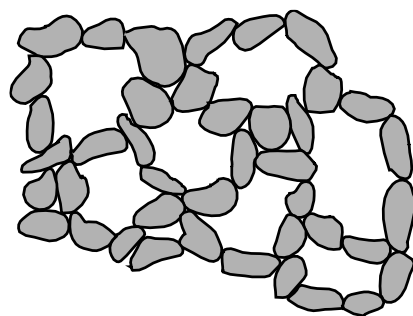
Figure 2.3. Macrovoids

- Physico-chemical effects and cementation between the particles are not taken into account (Kolymbas 1985).

- The deformation and strain accumulations are formulated based on homogeneous boundary conditions so that shear localizations are ignored (Niemunis and Herle 1997; Niemunis 2002).

- Since the model is rate independent, time dependent behavior such as creep and relaxation cannot be investigated by using hypoplastic model (visco-hypoplastic models developed by Niemunis or Wu can be used for the consideration of rate dependency).

In the following parts of the Chapter 2, a review of the mathematical background and applicability of the hypoplastic constitutive model for the cyclic loaded granular soils are presented. The laboratory experiments and numerical methods required to determine the model parameters are explained systematically.

2.1.2.1. Basic Hypoplasticity

The theory of hypoplasticity was developed by Kolymbas in 1985 as an alternative to elastoplastic models (Kolymbas 1985). Over the years, various modifications and improvements have been proposed by (Wu et al. 1993; Wu and Bauer 1994; Kolymbas et al. 1995; Bauer 1996; Gudehus 1996; Wu et al., Hypoplastic constitutive model with critical state for granular materials 1996). In this thesis, Wolffersdorff 's version of hypoplasticity (von Wolffersdorff 1996) with the so-called intergranular strain concept (Niemunis and Herle 1997) has been used to simulate the mechanical behavior of the granular soil (Molenkamp et al. 2010). In order to point out the difference between the hypoplastic models, the terms so-called "basic hypoplasticity" and "reference model" have been used for the hypoplastic models defined without intergranular strain concept and the version improved by von Wolffersdorff respectively.

Although the basic hypoplastic models perform very accurate simulations for granular materials subjected to monotonic loading conditions, prediction capability of them under cyclic and dynamic loadings are not that good (Anaraki, Hypoplasticity Investigated: Parameter Determination and Numerical Simulation 2008; Dung 2010;

Molenkamp et al. 2010). Numerical simulations performed using basic hypoplasticity revealed some shortcomings in the small strain region as an excessive accumulation of plastic deformation and pore pressure, especially during the change of loading direction (i.e. loading and unloading) (Niemunis and Herle 1997). The detailed information regarding the outcomes of these shortcomings and the solution proposed by (Niemunis and Herle 1997) are presented in the next part: "Extended Hypoplasticity".

The first version of the hypoplastic constitutive law, which is developed by (Kolymbas 1985), was defined with a single state variable, granular effective stress $\mathbf{T}$ and sets of material constants C_1, C_2, C_3 and C_4 determined from the critical state Equation (2.6) and (2.7) (Kolymbas 1985; Wu 1992).

$$\mathring{\mathbf{T}} = \mathring{\mathbf{T}}(\mathbf{T}, \mathbf{D}) \tag{2.6}$$

$$\mathring{\mathbf{T}} = C_1 \frac{1}{2}(\mathrm{tr}\mathbf{T})\mathbf{D} + C_2 \frac{\mathrm{tr}(\mathbf{T} \cdot \mathbf{D})}{\mathrm{tr}\mathbf{T}}\mathbf{T} + \left[C_3 \frac{\mathbf{T} \cdot \mathbf{T}}{\mathrm{tr}\mathbf{T}} + C_4 \frac{\mathbf{T}^* \cdot \mathbf{T}^*}{\mathrm{tr}\mathbf{T}}\right]\|\mathbf{D}\| \tag{2.7}$$

Later, these material constants were formulated in terms of the void ratio $\mathbf{e}$. Determination of material parameters from the granulometric properties of the soil made the calibration procedure easier. Also, with that improvement, constitutive model gained the ability of investigating the effects of changing void ratio (Bauer 1996; von Wolffersdorff 1996). The general form of the void ratio dependent hypoplastic equation took the following form,

$$\mathring{\mathbf{T}}(\mathbf{T}, \mathbf{e}, \mathbf{D}) = \mathcal{L}(\mathbf{T}, \mathbf{e}) : \mathbf{D} + \mathbf{N}(\mathbf{T}, \mathbf{e}) \cdot \|\mathbf{D}\| \tag{2.8}$$

The above given Equation (2.8), was further modified by (Gudehus 1996) to include the influence of the stress level (barotropy) and the densification (pyknotropy) on the mechanical behavior of the soil. This modification led model to a consistent description of the SOM state (Sweeping out of memory) (Bauer et al. 2003). The modified constitutive equation proposed by Gudehus reads as,

$$\mathring{\mathbf{T}} = f_s \mathcal{L} : \mathbf{D} + f_s f_d \mathbf{N} \cdot \|\mathbf{D}\| \tag{2.9}$$

$$\text{OR}$$

$$\overset{\circ}{\mathbf{T}} = f_s[\mathcal{L} : \mathbf{D} + f_d \mathbf{N} \cdot \|\mathbf{D}\|] \tag{2.10}$$

Here the constitutive tensors $\mathcal{L}$ and $\mathbf{N}$ are factorized with the void ratio dependent dimensionless scalar factors f_s and f_d to control the influence of the barotropy and pyknotropy. The influence of the current void ratio and the mean pressure is taken into account by the barotropy factor f_s and the pyknotropy factor f_d is used to incorporate strain softening and critical state concepts into the model (Bauer 1995).

Soils have a unique characteristic that they can change in volume when they sheared. Referring to the fundamental knowledge of the soil mechanics, under continuous shearing, depending on the initial condition, soil contracts or dilates and independent from the initial condition, comes into a state where the material keeps deforming at constant stress and volume. The mathematical correspondence of the previous sentence is implemented into the elastoplasticity with the critical state concept. The counterpart of this approach in hypoplasticity can be obtained as follows,

For $\mathbf{e} = \mathbf{e}_c$ and $\mathbf{T} = \mathbf{T}_c$, continued shear takes place at a stationary stress state and constant void ratio,

$$\dot{\mathbf{e}} = 0 \text{ (or } \dot{\varepsilon}_v = 0) \text{ and } \overset{\circ}{\mathbf{T}} = 0 \tag{2.11}$$

Using the general form of the hypoplastic constitutive relationship given in the Equation (2.10),

$$\overset{\circ}{\mathbf{T}} = f_s[\mathcal{L} : \mathbf{D} + f_d \mathbf{N} \cdot \|\mathbf{D}\|] = 0 \tag{2.12}$$

By definition, in order to describe the critical state, the factor f_d is formulated such that $f_d = 1$ must be satisfied for $\mathbf{e} = \mathbf{e}_c$, see Equation (2.34). Then the direction of the strain rate (a kind of flow rule) is obtained as,

$$\vec{\mathbf{D}} = \frac{\mathbf{D}}{\|\mathbf{D}\|} = -\mathcal{L}^{-1} : \mathbf{N} \tag{2.13}$$

By using the definition of the Euclidean norm given in the Table 1.1, left hand side of the Equation (2.13) can be written as,

$$\vec{\mathbf{D}} : \vec{\mathbf{D}} = \|\vec{\mathbf{D}}\|^2 = \frac{\mathbf{D} : \mathbf{D}}{\|\mathbf{D}\|^2} = 1 \tag{2.14}$$

Inserting the Equation (2.13) into the relation given in the Equation (2.14) we obtain,

$$\left(\mathcal{L}^{-1}:\mathbf{N}\right):\left(\mathcal{L}^{-1}:\mathbf{N}\right) - 1 = 0 \tag{2.15}$$

So far, for all the derivations, only one of the conditions ($\overset{\circ}{\mathbf{T}} = 0$) stated in Equation (2.11) has been used. But, in order to fully satisfy the critical state conditions given in the Equation (2.11), $\dot{\mathbf{e}} = 0$ (or $\dot{\varepsilon}_v = 0$) should also be incorporated.

By definition, the volumetric strain can be written as,

$$\varepsilon_v = \varepsilon_{11} + \varepsilon_{22} + \varepsilon_{33} \tag{2.16}$$

$$\text{OR}$$

$$\varepsilon_v = \text{tr}(\boldsymbol{\varepsilon}) \tag{2.17}$$

The constant volume at failure is,

$$\dot{\varepsilon}_v = \text{tr}(\dot{\boldsymbol{\varepsilon}}) = \text{tr}(\mathbf{D}) = 0 \tag{2.18}$$

$$\frac{1}{\|\mathbf{D}\|}\text{tr}(\mathbf{D}) = \text{tr}\left(\frac{\mathbf{D}}{\|\mathbf{D}\|}\right) = \text{tr}(\vec{\mathbf{D}}) = 0 \tag{2.19}$$

Finally, combining the Equation (2.13) and the Equation (2.19), a failure surface defined by tensors $\mathcal{L}$ and $\mathbf{N}$ is obtained, Equation (2.20).

$$\text{tr}\left(\mathcal{L}^{-1}:\mathbf{N}\right) = 0 \tag{2.20}$$

For a better mathematical representation, Equation (2.20) can be rewritten as follows,

$$\text{tr}\left(\mathcal{L}^{-1}:\mathbf{N}\right) = \text{tr}\left(\mathbf{1}:\left(\mathcal{L}^{-1}:\mathbf{N}\right)\right) \tag{2.21}$$

$$\text{tr}\left(\mathbf{1}:\left(\mathcal{L}^{-1}:\mathbf{N}\right)\right) = 0 \tag{2.22}$$

$$\mathbf{1}:\left(\mathcal{L}^{-1}:\mathbf{N}\right) = 0 \tag{2.23}$$

where $\mathbf{1}$ is the unit tensor.

For all $\mathbf{T} \in \left\{\mathbf{T}\middle|\overset{\circ}{\mathbf{T}} = \mathbf{0}\right\} \cap \mathbf{e} \in \{\mathbf{e}|\dot{\mathbf{e}} = 0\}$, Equation (2.23 or 2.20) describes the critical stress state. This stress and void ratio dependent yield function can be generalized as,

$$y(\mathbf{T}, \mathbf{e}) = \mathbf{1}:\left(\mathcal{L}^{-1}:\mathbf{N}\right) = 0 \tag{2.24}$$

Unlike the previous versions of the hypoplasticity, (von Wolffersdorff 1996) implemented a predefined well-established critical state concept adopted from (Matsuoka and Nakai 1974) into the model previously developed by (Gudehus, A comprehensive constitutive equation for granular materials 1996). This model which is referred as the reference model nowadays considered as a standard basic hypoplastic model for granular soils. The mathematical representation of the modified $\mathcal{L}$ and $\mathbf{N}$ tensors, which include the (Matsuoka and Nakai 1974) failure criterion, can be written as,

$$\mathcal{L} = f_s \frac{1}{\widehat{\mathbf{T}} : \widehat{\mathbf{T}}} \left(F^2 \boldsymbol{I} + a^2 \widehat{\mathbf{T}} \otimes \widehat{\mathbf{T}} \right) \tag{2.25}$$

$$\mathbf{N} = f_s f_d \frac{a \cdot F}{\widehat{\mathbf{T}} : \widehat{\mathbf{T}}} \left(\widehat{\mathbf{T}} + \widehat{\mathbf{T}}^* \right) \tag{2.26}$$

Using these modified tensor Equations (2.25 and 2.26), the constitutive equation of the von Wolffersdorff's hypoplastic model can be written as,

$$\mathring{\mathbf{T}} = f_s \frac{1}{\mathrm{tr}(\widehat{\mathbf{T}}^2)} \left(F^2 \mathbf{D} + a^2 \mathrm{tr}(\widehat{\mathbf{T}} \mathbf{D}) \widehat{\mathbf{T}} + f_d a F (\widehat{\mathbf{T}} + \widehat{\mathbf{T}}^*) \|\mathbf{D}\| \right) \tag{2.27}$$

where,

- ❖ $\widehat{\mathbf{T}} = \mathbf{T}/\mathrm{tr}(\mathbf{T})$ is dimensionless (normalized) stress obliquity and $\widehat{\mathbf{T}}^* = \widehat{\mathbf{T}} - \frac{1}{3}\mathbf{1}$ is dimensionless stress deviator. Note that, $\mathrm{tr}(\mathbf{T})/3$ corresponds to mean pressure.

- ❖ The term $\boldsymbol{I}$ (fourth order unit tensor) is given by,

$$\boldsymbol{I}_{ijkl} = 0.5 \cdot \left(\delta_{ik}\delta_{jl} + \delta_{il}\delta_{jk} \right) \tag{2.28}$$

- ❖ The scalar coefficients a and F are adapted from the Matsuoka-Nakai failure criterion. The yield surface and the shape of the deviatoric plane obtained using these coefficients are given in Figure 2.5.

$$a = \frac{\sqrt{3}(3 - \sin \varphi_c)}{2\sqrt{2} \sin \varphi_c} \tag{2.29}$$

19

φ_{c}: critical state friction angle (Hypoplastic model parameter)

$$F = \sqrt{\frac{1}{8}\tan^2\psi + \frac{2 - \tan^2\psi}{2 + \sqrt{2}\tan\psi\cos 3\theta}} - \frac{1}{2\sqrt{2}}\tan\psi \qquad (2.30)$$

with,

$$\tan\psi = \sqrt{3}\|\hat{\mathbf{T}}^*\| \qquad (2.31)$$

$$\cos 3\theta = -\sqrt{6}\frac{\text{tr}(\hat{\mathbf{T}}^* \cdot \hat{\mathbf{T}}^* \cdot \hat{\mathbf{T}}^*)}{[\hat{\mathbf{T}}^* : \hat{\mathbf{T}}^*]^{3/2}} \qquad (2.32)$$

The geometrical representation of the $\tan\psi$ and Lode angle θ are given in Figure 2.4.

❖ The scalar barotropy (stress level) factor f_{s},

$$f_{\text{s}} = \frac{\frac{h_{\text{s}}}{n}\left(\frac{e_{\text{i}}}{e}\right)^{\beta}\left(\frac{1 + e_{\text{i}}}{e_{\text{i}}}\right)\left(\frac{-\text{tr}(\mathbf{T})}{h_{\text{s}}}\right)^{1-n}}{3 + a^2 - a\sqrt{3}\left(\frac{e_{\text{i}0} - e_{\text{d}0}}{e_{\text{c}0} - e_{\text{d}0}}\right)^{\alpha}} \qquad (2.33)$$

❖ The scalar pyknotropy (densification) factor f_{d},

$$f_{\text{d}} = \left(\frac{e - e_{\text{d}}}{e_{\text{c}} - e_{\text{d}}}\right)^{\alpha} \qquad (2.34)$$

The parameters used to formulate above given equations: φ_{c}, h_{s}, n, $e_{\text{d}0}$, $e_{\text{c}0}$, $e_{\text{i}0}$, α and β are the hypoplastic constitutive model parameters obtained from the laboratory experiments. The physical meanings of these parameters are given in Table 2.1 and methods used to determine them are detailly explained in section 2.1.2.3.

Table 2.1. *Hypoplastic Model parameters (Bayraktaroglu 2018, Reyes et al. 2009)*

Parameter	Physical Meaning
φ_c	Critical state friction angle
h_s and n	Controls the shape of the compression curve
e_{d0}, e_{i0} and e_{c0}	Reference void ratios (minimum, maximum and critical respectively) controlling limiting void ratios at zero pressure (stress free state)
α	Describes the transition between peak and critical stress and controls the dilatancy
β	Controls the relation between the relative density and stiffness

The angles ψ and θ, which are used to formulate coefficients a and F, locates the position of Cauchy stress **T** in the space of principal stresses as shown in Figure 2.4.

Figure 2.4. The geometrical representation of the tan ψ and Lode angle θ in the stress space.

Implementation of a failure criterion into a constitutive model is essential for the realistic representation of the soil behavior upon failure. For that purpose, within the framework of the constitutive model, an admissible stress range should be defined

using a failure criterion (Puzrin 2012). Furthermore, a control mechanism should be employed such that the stresses beyond the predefined range are projected back to yield surface together with a flow (preferably non-associative) and a hardening rule (Wichtmann, Explicit Accumulation Model for Non-cohesive Soils under Cyclic Loading 2005).

Among the many failure criteria (e.g. Tresca, von-Mises, Mohr-Coulomb) hypoplasticity incorporates the Matsuoka-Nakai failure criterion. Compare to the other failure criteria, Matsuoka-Nakai has neither a circular (von-Mises) nor a hexagonal (Mohr-Coulomb) deviatoric plane. Similar to the relation between Tresca and von-Mises criteria; Matsuoka-Nakai criterion is formulated by averaging the Mohr-Coulomb in such a way that both criteria match at Mohr-Couloms's hexagonal corners (triaxial compression and extension) Figure 2.6 (Matsuoka and Nakai 1974). The shape of the failure criterion is illustrated in Figure 2.5.

(a)　　　　　　　　　　(b)
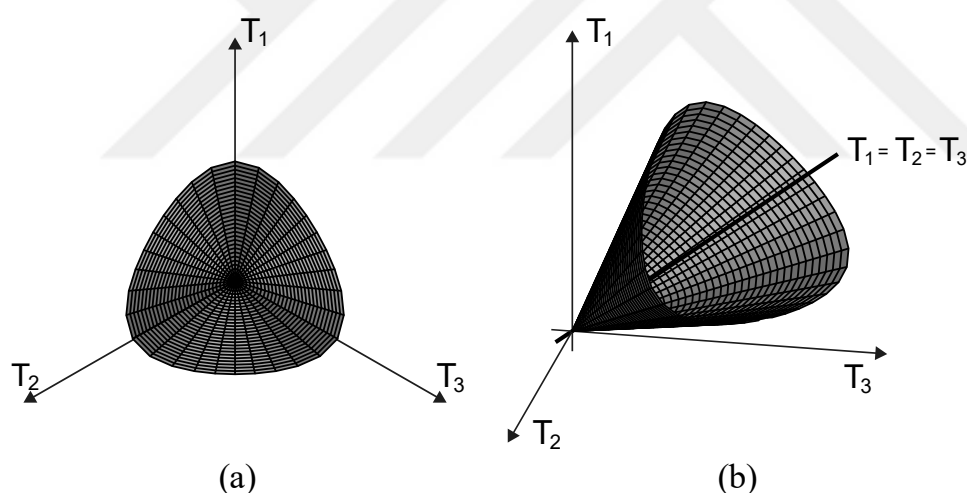
Figure 2.5. Matsuoka-Nakai failure criterion (a) in deviatoric plane (b) in 3D principal stress space

The implementation of the Matsuoka-Nakai criterion do not just provide a better approximation of the soil behavior, but also the smoothened path provides a better numerical efficiency at the corners. From computational point of view, it is a known fact that vertices at failure surfaces require more computational power (Bocchi 2014; Winde H. P. 2015).
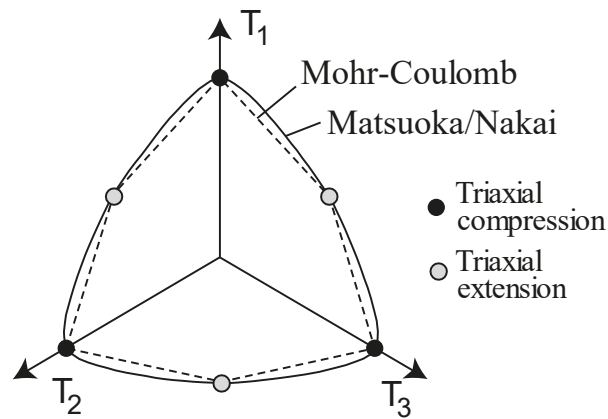
Figure 2.6. Failure criterion of Matsuoka-Nakai and Mohr-Coulomb (Wichtmann, 2005)

The influence of the stress level (barotropy) and densification (pyknotropy) on the stiffness of the system is taken into account by using Equation 2.33 and 2.34 respectively. In these equations, reference void ratios with "0" indices (e_{d0}, e_{i0} and e_{c0}, given in Table 2.1) and mean stress dependent limiting void ratios e_d, e_i and e_c are used. Here, e_d and e_i defines admissible states (in other words, possible minimum and maximum void ratios) at any stress, p. The shaded area in Figure 2.7. represents the inadmissible area.
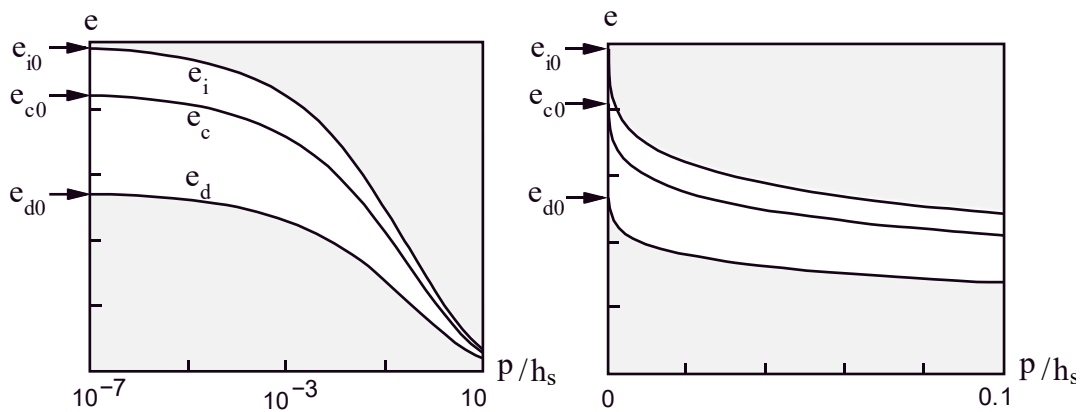
Figure 2.7. Relation between limiting void ratios and mean effective stress

According to (Bauer 1996) the void ratio curves are affinitive to each other as a function of the mean effective stress and asymptotically approach a threshold value at high stresses. This coincides with the investigations of (Lee and Seed 1967). The mathematical formulation of the afore-mentioned relation is given in Equation 2.35,

23

$$\frac{e_\text{i}}{e_\text{i0}} = \frac{e_\text{c}}{e_\text{c0}} = \frac{e_\text{d}}{e_\text{d0}} = \exp\left[-\left(\frac{3 \cdot \text{p}}{h_\text{s}}\right)^{n}\right] \tag{2.35}$$

where mean effective stress $\text{p} = \text{tr}(\mathbf{T})/3$.

In this part, the mathematical description of the von Wolffersdorff's version of hypoplasticity, reference model, is summarized. Development of the single tensorial equation that describes the stress change due to the rearrangements of the particles is formulated. Flow rule, switching functions and failure surface are emerged as by-products of the model (they are not defined explicitly in hypoplasticity) (Tejchman 2008).

Although the model has a good predictive capability for the soils subjected to monotonic loading conditions, it is hard to say the same thing for the repetitive (e.g. cyclic and dynamic) loadings. The limitations of the model and the proposed solution by (Niemunis and Herle 1997) is explained in detail and outputs of both models compared in the next part of the thesis.

2.1.2.2. Extended Hypoplasticity

The extended hypoplastic model which is also referred as hypoplastic model with intergranular strain (IGS) was developed by (Niemunis and Herle 1997) based on the von Wolffersdorff's reference model.

Even though the effect void ratio is taken into account and loading/unloading path is differentiated with a single tensorial equation, the increase of the stiffness due to change of loading direction is not reproduced adequately in the basic hypoplastic models (Wichtmann, Explicit Accumulation Model for Non-cohesive Soils under Cyclic Loading 2005). According to the (Niemunis 2002), basic hypoplastic models exhibit a too low shear stiffness in case of shear deformations near *p*-axis. As a result, model yields excessive deformation and pore pressure accumulations, especially at small stress cycles. Unlike the hysteresis loops, a saw-tooth like behavior (ratcheting) is produced. For a better illustration of the ratcheting effect, a consolidated undrained

(CU) triaxial test is simulated both with and without intergranular strain concepts, Figure 2.8.
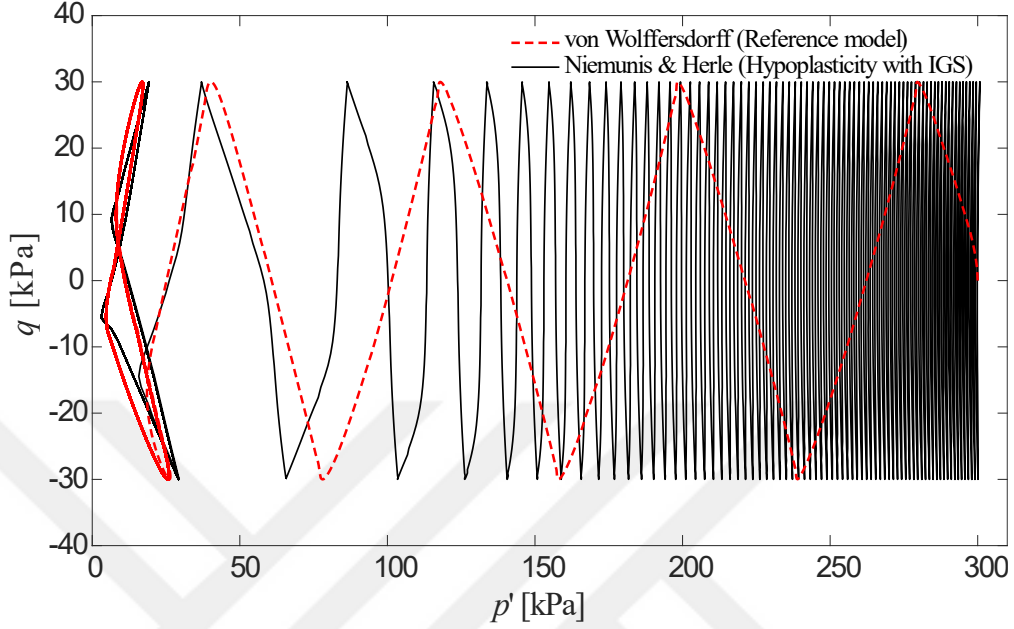
Figure 2.8. Simulation of an undrained cyclic triaxial (CU) test with and without intergranular strain

Let's also mathematically investigate the excessive stress and strain accumulations and corresponding ratcheting effect. For the simplicity of the tensorial calculations, assume a 1D consolidation problem where the general form of the hypoplastic constitutive model, Equation 2.3 can be converted to a scalar form,

$$\mathring{T} = L \cdot D + N \cdot |D| \tag{2.36}$$

assuming a small stress and void ratio change we can conclude that $\pm\Delta\varepsilon = \pm D \cdot \Delta t$ where the sign "$\pm$" refers to loading and unloading. Multiplying the both side of the Equation 2.36 with Δt, the corresponding stress increment ΔT can be obtained as,

$$\Delta T = L \cdot \Delta\varepsilon + N \cdot |\Delta\varepsilon| \tag{2.37}$$

For a full small strain cycle with a path: $0 \rightarrow \Delta\varepsilon \rightarrow 0 \rightarrow -\Delta\varepsilon \rightarrow 0$, stress accumulation becomes,

$$\Delta T^{acc} = L \cdot \Delta\varepsilon + N \cdot |\Delta\varepsilon| - L \cdot \Delta\varepsilon + N \cdot |-\Delta\varepsilon| = 2N|\Delta\varepsilon| \tag{2.38}$$

Similarly, for a small stress cycle, strain accumulation becomes,

$$\Delta\varepsilon^{acc} = \frac{\Delta T}{L+N} + \frac{-\Delta T}{L-N} = \frac{-2N}{L^2 - N^2}\Delta T \qquad (2.39)$$

In both calculations, the results are overpredicted. Graphical representation of the small strain induced stress accumulation and small stress induced strain accumulation are presented in Figure 2.9.
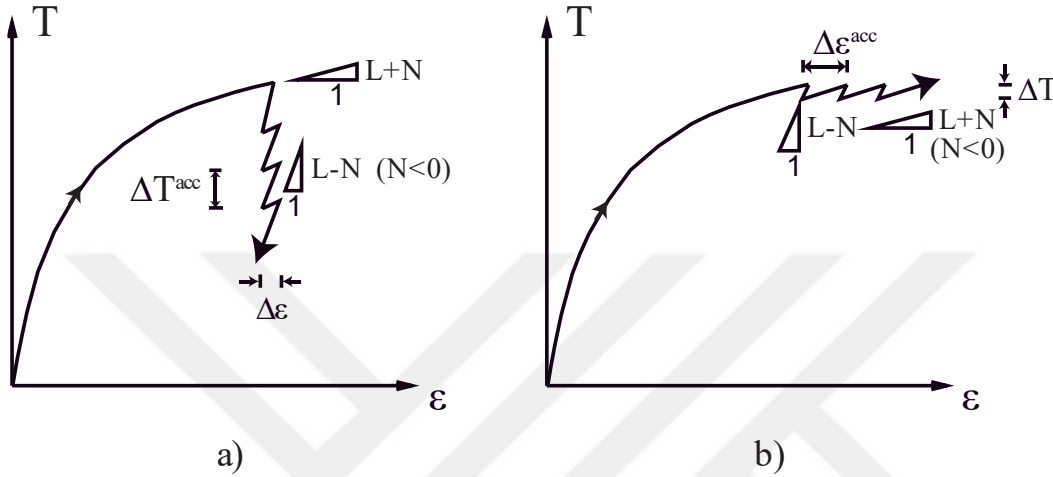
Figure 2.9. Excessive (a) stress and (b) strain accumulations during small strain and stress cycles

The effects of small strain deformation and path dependence on the soil stiffness are started to be investigated with the advancements in the laboratory experiments (Jardine et al. 1984; Tatsuoka 1988; Viggiani and Atkinson 1995). Together with that experimental data, engineers started to improve their constitutive model so that the path dependent behavior is taken into account. In elastoplasticity, the term "hardening" is used for that and today most of the advanced elastoplastic models include that rule. Theoretical background of the IGS concept is actually similar to the kinematic-hardening rule. Both are developed to take into account the stiffness change upon reversal of loading or deformation directions.

In order to overcome these shortcomings and enhance the cyclic capability of the model, a new state parameter so-called intergranular strain, $\mathbf{h}$ is introduced to the model, $\mathring{\mathbf{T}}(\mathbf{T}, \mathbf{e}, \mathbf{D}, \mathbf{h})$, by (Niemunis and Herle 1997). The main idea behind this new concept is to create an interface zone that captures the large micro-deformations (macroscopic measure of micro-deformations) and stores recent deformation history

26

(Niemunis and Herle 1997). Figure 2.10 very well illustrates the intergranular strain concept. In this figure, at the end of the three different deformation paths, soils reach a state at point * where they have the same current stress, void ratio and strain rates, but different stiffness. Here, bold arrow ends represent the recent deformation history and strain rate tensor, **D** is independent from them, however, **h** is defined according to them.
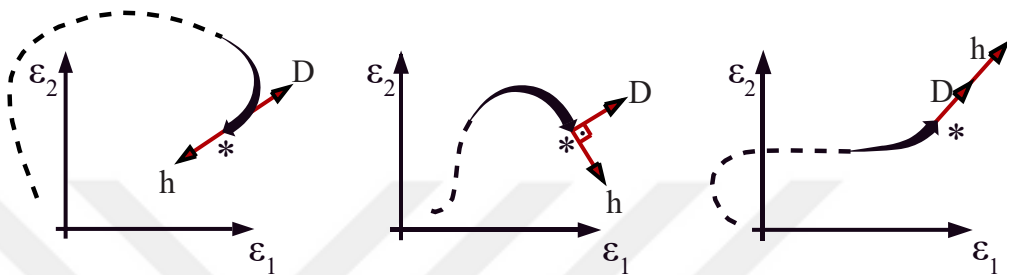
Figure 2.10. Relation between intergranular strain, h and deformation history (Niemunis, 2002)

During deformation, the intergranular strain, **h** increases up to its maximum value, R and remain constant under further deformation. For a better understanding, 1D representation of the micro-level deformations between two particles is given in Figure 2.11. According to the extended version of the model, the total deformation is composed of two stage: first small strain deformations occur in the intergranular zone ($\varepsilon < R$), and then together with the sliding, irreversible rearrangement of particles takes place (Masin 2012).
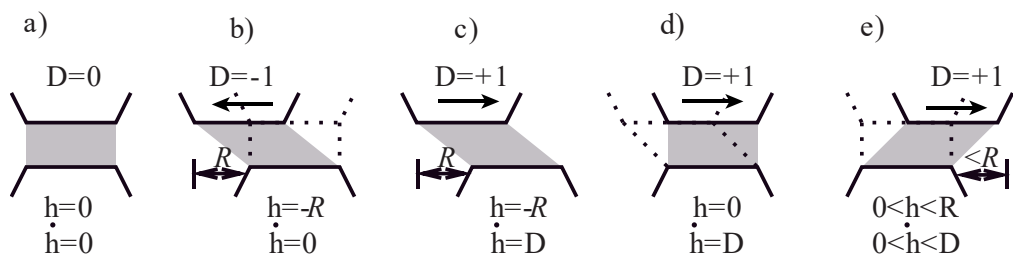
Figure 2.11. 1-D interpretation of the intergranular strain (Niemunis & Herle, 1997)

Depending on the change in deformation direction, stiffness of soil changes. According to the measures, maximum stiffness occurs upon a complete (i.e. 180°) strain rate reversal (Atkinson et al. 1990). The stiffness increase after 180° and 90°

reversals are represented by E_R and E_T respectively, in Figure 2.12. In other words, E_R is the stiffness of the soil when the angle between $\vec{h}$ and $\vec{D}$ is equal to 180°.
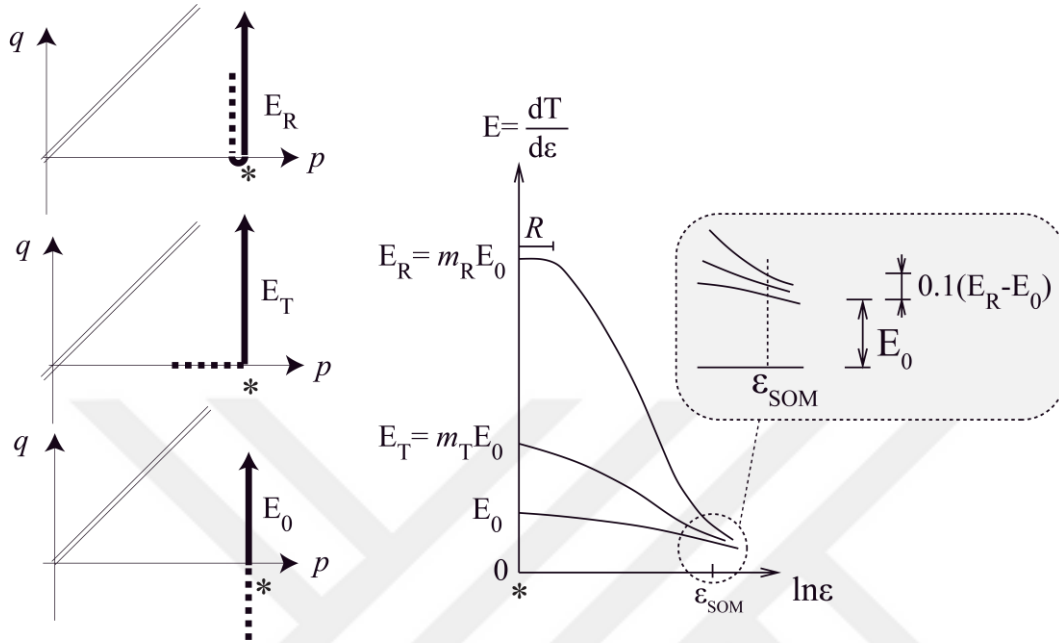
Figure 2.12. Characteristic stiffness values for model calibration

Immediately after the reversal, if shearing continues in the same direction, the stiffness values start to decrease and become "almost" equal to each other at $\varepsilon = \varepsilon_{SOM}$ (The subscript SOM is an abbreviation for "swept-out memory"). Here the important point is, the response of the model highly depends on the deformation history until the strain reaches ε_{SOM}. After that point, the strain reversal at point * is assumed to be no longer affecting the actual respond of the system. At point ε_{SOM}, soil reaches a state in which deformation history (or memory) is forgotten (Gudehus 2011). From a mathematical point of view, it is assumed that ε_{SOM} is reached when the additional stiffness due to change in deformation direction (e.g. $E_R - E_0$) decreases 10% of its maximum value.

The mathematical formulation of the extended model is constructed over the von Wolffersdorff's reference model. Different from the general form given in Equation 2.3, instead of the tensors $\mathcal{L}$ and $\mathbf{N}$, a fourth order stiffness tensor, $\mathcal{M}$ is used as shown in Equation 2.40.

$$\mathring{\mathbf{T}} = \mathcal{M}(\mathbf{T}, \mathbf{e}, \mathbf{h}) : \mathbf{D} \tag{2.40}$$

In this equation, stiffness tensor $\mathcal{M}$ is calculated using two hypoplastic tensors $\mathcal{L}(\mathbf{T}, \mathbf{e})$ and $\mathbf{N}(\mathbf{T}, \mathbf{e})$ and additional state variable $\mathbf{h}$.

For an arbitrary value of intergranular strain $(0 \leq \mathbf{h} \leq R)$, depending on the angle between $\vec{\mathbf{h}}$ and $\mathbf{D}$, two distinct conditions need to be formulated:

- reversal angle is less than $90°$ $\left(\text{or } \vec{\mathbf{h}} : \mathbf{D} > 0\right)$
- reversal angle is greater or equal to $90°$ $\left(\text{or } \vec{\mathbf{h}} : \mathbf{D} \leq 0\right)$

The general form of the "interpolated" stiffness tensor $\mathcal{M}$ for any arbitrary $\mathbf{h} \in \{\mathbf{h} | 0 \leq \mathbf{h} \leq R\}$ can be written as,

$$\mathcal{M} = [\rho^\chi m_{\mathrm{T}} + (1 - \rho^\chi) m_{\mathrm{R}}] \mathcal{L} + \begin{cases} \rho^\chi (1 - m_{\mathrm{T}}) \mathcal{L} : \vec{\mathbf{h}}\vec{\mathbf{h}} + \rho^\chi \mathbf{N}\vec{\mathbf{h}} & \text{for } \vec{\mathbf{h}} : \mathbf{D} > 0 \\ \rho^\chi (m_{\mathrm{R}} - m_{\mathrm{T}}) \mathcal{L} : \vec{\mathbf{h}}\vec{\mathbf{h}} & \text{for } \vec{\mathbf{h}} : \mathbf{D} \leq 0 \end{cases} \tag{2.41}$$

where,

The normalized magnitude of the intergranular strain, ρ is equal to,

$$\rho = \frac{\|\mathbf{h}\|}{R} \tag{2.42}$$

The direction of the intergranular strain is defined as,

$$\vec{\mathbf{h}} = \begin{cases} \dfrac{\mathbf{h}}{\|\mathbf{h}\|} & \text{for } \mathbf{h} \neq 0 \\ 0 & \text{for } \mathbf{h} = 0 \end{cases} \tag{2.43}$$

m_{T}, m_{R} and χ are material constants (Table 2.2).

The stress envelopes developed by Equation 2.41 for $\rho = 1$ and $\rho = 0$ are depicted in the Figure 2.13. Let's make a deep review for these two special cases and try to understand why the term interpolated is used for Equation 2.41:

First, the case with a fully mobilized intergranular strain, $\rho = 1$ or $\mathbf{h} = R$ (point B in Figure 2.13):

29

- For a monotonic deformation with $\mathbf{D} \sim \vec{\mathbf{h}}$ in which the angle between $\mathbf{D}$ and $\vec{\mathbf{h}}$ is equal to $0°$ and $\vec{\mathbf{h}}\colon \mathbf{D} > 0$, Equation 2.41 can be simplified to,

$$\mathcal{M} = \mathcal{L} + \mathbf{N}\vec{\mathbf{h}} \tag{2.44}$$

Here note that, $\mathbf{D} = \vec{\mathbf{h}}\|\mathbf{D}\|$ and $\mathbf{N}\vec{\mathbf{h}}\colon \mathbf{D} = \mathbf{N}\|\mathbf{D}\|$. So, if both sides of the Equation 2.44 is multiplied by $\mathbf{D}$, we obtain:

$$\overset{\circ}{\mathbf{T}} = \mathcal{M}\colon \mathbf{D} = \mathcal{L}\colon \mathbf{D} + \mathbf{N}\cdot\|\mathbf{D}\| \tag{2.45}$$

which corresponds to hypoplastic behavior <u>without intergranular strain.</u>

- For a complete strain reversal with $\mathbf{D}\sim -\vec{\mathbf{h}}$ in which the angle between the tensors is equal to $180°$ and $\vec{\mathbf{h}}\colon \mathbf{D} < 0$, Equation 2.41 can be simplified to,

$$\mathcal{M} = m_\mathrm{R}\,\mathcal{L} \tag{2.46}$$

where the stiffness value takes the maximum value.

- For a $90°$ change in the direction of deformation, $\mathbf{D} \perp \vec{\mathbf{h}}$ and $\vec{\mathbf{h}}\colon \mathbf{D} = 0$, Equation 2.41 can be simplified to,

$$\mathcal{M} = m_\mathrm{T}\,\mathcal{L} \tag{2.47}$$

with a range $m_\mathrm{R} > m_\mathrm{T} > 1$

Second, the case with $\rho = 0$ (point A in Figure 2.13):

- Independent from the direction of $\mathbf{D}$,

$$\mathcal{M} = m_\mathrm{R}\,\mathcal{L} \tag{2.48}$$

Above the boundaries of the ρ, (i. e. $\mathbf{h} = R$ and $\mathbf{h} = 0$) are defined. But what will be the stiffness for $\rho \in \{\rho|0 < \rho < R\}$? Answer: The stiffness tensor will be interpolated by a weighted factor ρ^χ as shown in Equation 2.41.

The evolution of the deformation dependent intergranular strain tensor is given as,

$$\overset{\circ}{\mathbf{h}} = \begin{cases} \mathcal{I} - \vec{\mathbf{h}}\vec{\mathbf{h}}\rho^{\beta_\mathrm{R}} & \text{for } \vec{\mathbf{h}}\colon \mathbf{D} > 0 \\ \mathbf{D} & \text{for } \vec{\mathbf{h}}\colon \mathbf{D} \leq 0 \end{cases} \tag{2.49}$$

where, β_R is a material constant that controls the evolution of the intergranular strain rate. The evolution of intergranular strains for $\beta_R = 1$ is illustrated for a simple 1-D model in Figure 2.14.
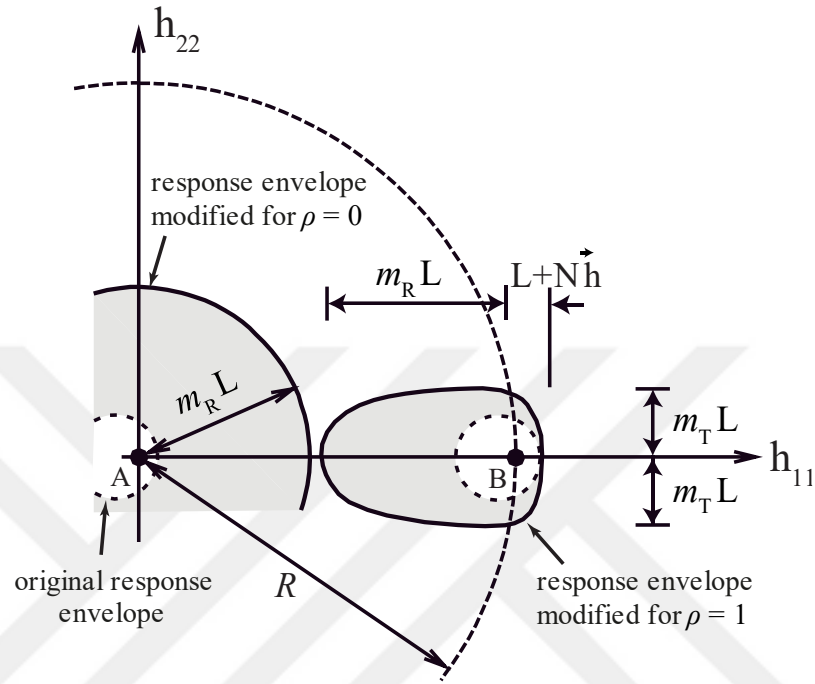
Figure 2.13. Modification of stiffness with mR and mT (Niemunis, 2002)
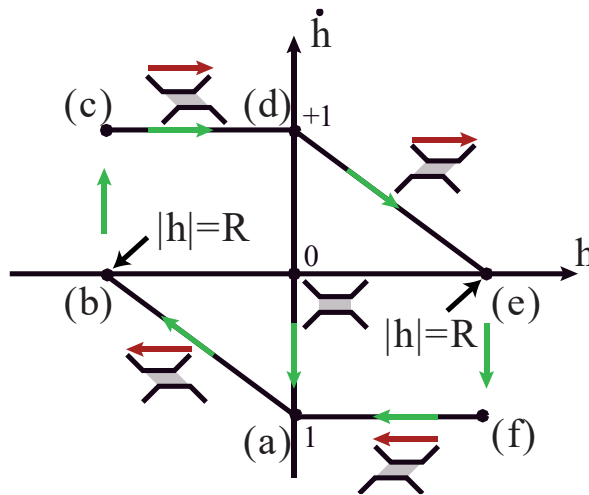
Figure 2.14. Evolution of the intergranular strain (Niemunis & Herle, 1997)

31

Table 2.2. *Additional material parameters for intergranular strain*

Parameter	Physical Meaning
m_T	Multiplier for stiffness increase after 90° reversal
m_R	Multiplier for stiffness increase after 180° reversal
R	Radius of intergranular strain range
β_R	Exponent controlling the rate $\overset{\circ}{\mathbf{h}}$
χ	Exponent controlling the stiffness degradation

One of the best ways of understanding a constitutive model and finding out the limitations of it is to understand the role of each parameter within their constitutive framework. In the next part, the laboratory experiments and numerical methods required to determine thirteen parameters of the hypoplastic constitutive model are explained systematically.

2.1.3. Parameter Determination

The extended hypoplastic model developed by Niemunis and Herle (1997) requires thirteen material parameters in which eight of them are coming from the basic hypoplasticity and remaining five parameters are added later to properly simulate the soil behavior and increase the accuracy under repetitive loading conditions. While these eight parameters listed in Table 2.1 are determined from the simple laboratory tests and granulometric properties (Herle 1997; Herle and Gudehus 1999); intergranular properties are used for the remaining five parameters given in Table 2.2 (Niemunis and Herle 1997; Niemunis 2002).

According to my personal experience, understanding the physical or mathematical role of a parameter within the constitutive model it belongs provides a comprehensive perspective and also helps during the calibration procedure of the model parameters. In the previous part, hypoplastic constitutive model is formulated using material parameters and now, the methods and experiments required to determine these parameters will be discussed in detail.

As you noticed during the formulation of the constitutive relations, together with some physical parameters (e.g. φ_c, e_{max}, e_{min}), theoretical parameters (e.g. e_{i0}, α and β) are also introduced to the system. Some of these parameters are obtained "directly" from the standard geotechnical tests such as angle of repose, triaxial tests; however, some of them, especially the theoretical parameters, are calibrated to simulate true behavior in a most realistic way. For the determination of these theoretical parameters, the general form given in Equation 2.27 is reduced to two-dimensional, axially symmetric triaxial compression test conditions, $T_1 > T_2 = T_3$, as follows,

$$\dot{T}_1 = f_s \frac{(T_1 + 2T_2)^2}{T_1{}^2 + 2T_2{}^2}\left(D_1 + a^2 \frac{T_1 D_1 + 2T_2 D_2}{(T_1 + 2T_2)^2}T_1 + f_d \frac{a}{3}\frac{5T_1 - 2T_2}{T_1 + 2T_2}\sqrt{D_1{}^2 + 2D_2{}^2}\right) \quad (2.50)$$

$$\dot{T}_2 = f_s \frac{(T_1 + 2T_2)^2}{T_1{}^2 + 2T_2{}^2}\left(D_2 + a^2 \frac{T_1 D_1 + 2T_2 D_2}{(T_1 + 2T_2)^2}T_2 + f_d \frac{a}{3}\frac{4T_2 - T_1}{T_1 + 2T_2}\sqrt{D_1{}^2 + 2D_2{}^2}\right) \quad (2.51)$$

Note that, $F = 1$ for axially symmetric condition. For more detail check Equation 2.30 and Figure 2.4.

Within the scope of this thesis, a set of laboratory experiments were conducted and hypoplastic material parameters of the sand used in these experiments are determined in our laboratory. Additional useful methods to determine these model parameters are developed and also some improvements are presented.

2.1.3.1. Critical Friction Angle, φ_c

The internal friction angle of a soil at critical state is called as the critical friction angle, φ_c. Since the friction angle, φ is a relative density dependent material parameter, during a deformation, depending on the change in density, it's magnitude changes. So, it is not a material specific parameter. However, independent from the initial relative density and deformation path, after a large monotonic shearing, soil reaches a steady state (or critical state) where the material keeps deforming under constant stress and volume. During this unique state, both the stress and volumetric strain rate vanishes as it previously described in Equation 2.11.

The critical friction angle, φ_c can be determined from simple shear, direct shear or triaxial tests. However, considering the simplicity and repeatability, angle of repose test proposed by (Miura et al. 1997) is suggested as an alternative to these tests by (Herle and Gudehus 1999). According to the data available in the literature, it is reasonable to assume $\varphi_c \approx \varphi_{rep}$, Table 2.3.

Table 2.3. *Comparison of angle of repose and critical friction angle (Herle & Gudehus, 1999)*

Material	Angle of repose, $\boldsymbol{\varphi_{rep}}(°)$	Critical angle of friction, $\boldsymbol{\varphi_c}(°)$	Test Type*
Hochstetten gravel	35.7	36.5	ds
Hochstetten sand	34.0	34.0	txd, ds
Hostun RF sand	32.0	32.0	txd
Karlsruhe sand	29.1	30.0	txd
Lausitz sand	33.0	32.2	txd
Toyoura sand	30.4	30.9	txu
Zbraslav sand	30.8	29.7	ds

* ds: direct shear test, txd: drained triaxial test, txu: undrained triaxial test

The angle of repose is the angle of a soil heap formed by slowly pouring the material (Figure 2.15). The procedure of the determination of the angle of repose is detailly described in (JGS 1996; Miura et al. 1997). In this method, the factors affecting the φ_{rep} can be listed as: amount of material used to form heap, pouring speed and the surface that heap is created. All these factors affecting the φ_{rep} is investigated in (Miura et al. 1997).
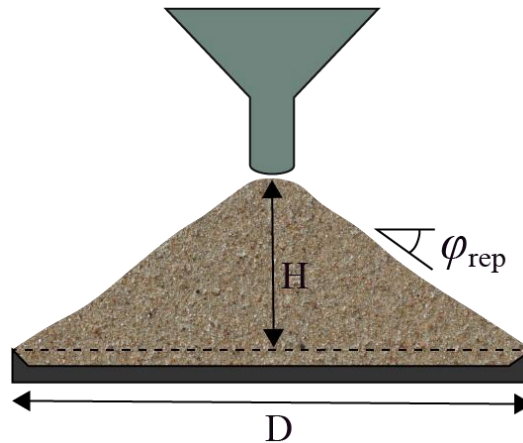
Figure 2.15. Determination of angle of repose

The angle of repose is determined as,

$$\tan(\varphi_{rep}) \cong \frac{2H}{D} \qquad (2.52)$$

Due to the nature of the soil material, grains are not perfectly spherical and because of that even though the height of the heap is constant from every angle of view; the actual angle of the slope is not. In order to eliminate this error, during the experiment instead of manually measuring H and D values, an image processing tool that captures the slopes is developed in MATLAB. The angle of the heap is measured from eight different angles with high accuracy and the average value is taken as φ_{rep}. The proposed method briefly includes the following steps:

- First, the camera is stabilized using a tripod.
- Each heap formation is photographed from eight different angles by rotating the plate each time with an angle of $45°$.
- Considering the possible lens distortion (fisheye effect), all the images are calibrated using computer vision toolbox "undistortFisheyeImage". For details: www.mathworks.com/help/vision/ug/fisheye-calibration-basics.html
- Images are first converted to gray scale (Figure 2.17) and then binary images (Figure 2.18), note that a black backdrop is used to ease these procedures.
- An algorithm that traces the boundaries of the sand is found.

- Finally, using the position of the dots near boundaries, a first-degree regression line is fitted and then the slope of the line is calculated.
- The detailed description of the method and the code is available on: https://blog.metu.edu.tr/e187152/applications/

Figure 2.16. Lens distortion corrected image before the processing
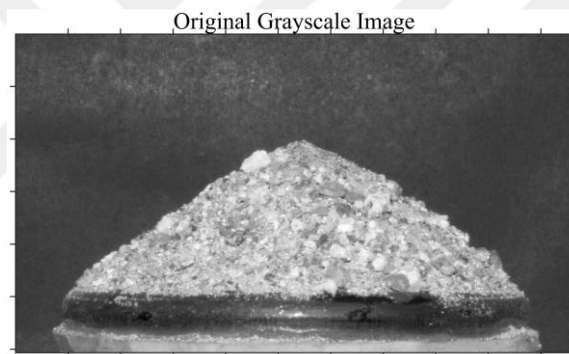
Figure 2.17. Original image is converted to grayscale
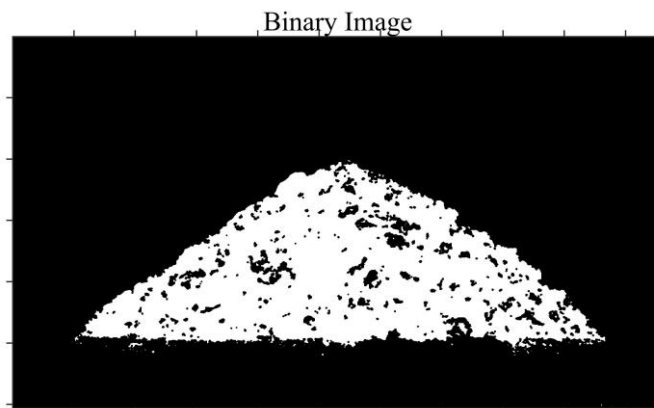
Figure 2.18. Grayscale image is converted to binary image
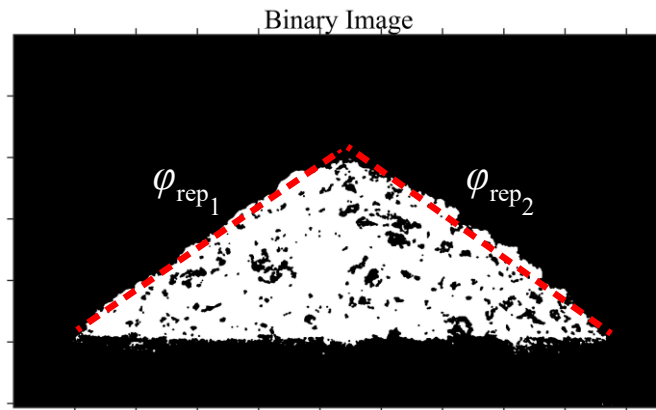
Figure 2.19. Binary image with outputs

In this thesis, using the above-mentioned image-processing method, three angle of repose tests have been performed. The results obtained from these tests are proposed in Figure 2.20. Here, y-axis represents the cumulative average value of the φ_{rep}.
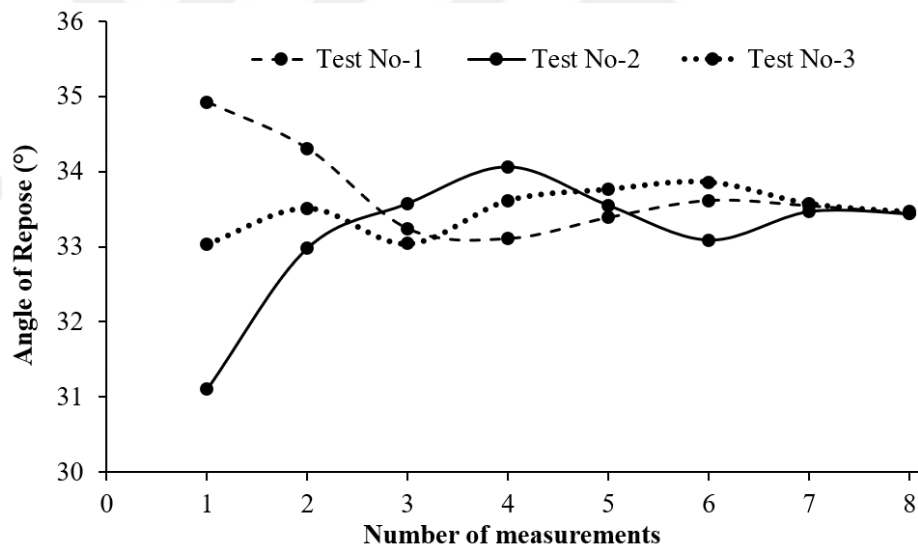
Figure 2.20. Output of the proposed new method

As a result, φ_c (or φ_{rep}) is determined as 33.45° with a standard deviation of 0.01°. Note that, the critical friction value determined from angle of repose test is used for the determination of the Matsuoka-Nakai failure criterion, Equation 2.29.

An additional comment: while performing the angle of repose test and observing the flow of sand particles, I have noticed that after a certain point any additional sand

particle poured on the heap continues to flow without negligible change in volume and angle of the heap just like the soil behavior we observe during the continuous shearing in critical state.

2.1.3.2. Granulate Hardness, h_s and Exponent n

The granulate hardness h_s and exponent n are two main parameters controlling the stiffness of the system. The parameter h_s is the only model parameter with the dimension of stress and referred as reference pressure. Note that, h_s do not represent the stiffness of the individual grains but skeleton as a whole. On the other hand, the exponent n accounts for the pressure sensitivity and controls the nonlinear relationship between h_s and mean pressure $p_s = \text{tr}(\mathbf{T})/3$.

Referring to Equation 2.35, for any particular initial void ratio at zero pressure, e_{p0} in which $e_{d0} \leq e_{p0} \leq e_{i0}$, the change in void ratio under a mean pressure p_s can be formulated using Equation 2.53,

$$e_p = e_{p0} \cdot \exp\left[-\left(\frac{3 \cdot p_s}{h_s}\right)^n\right] \qquad (2.53)$$

The influence of parameters h_s and n on compression curve is described in Figure 2.21. While the exponent n changes the curvature; granulate hardness h_s changes the slope of the compression curve.
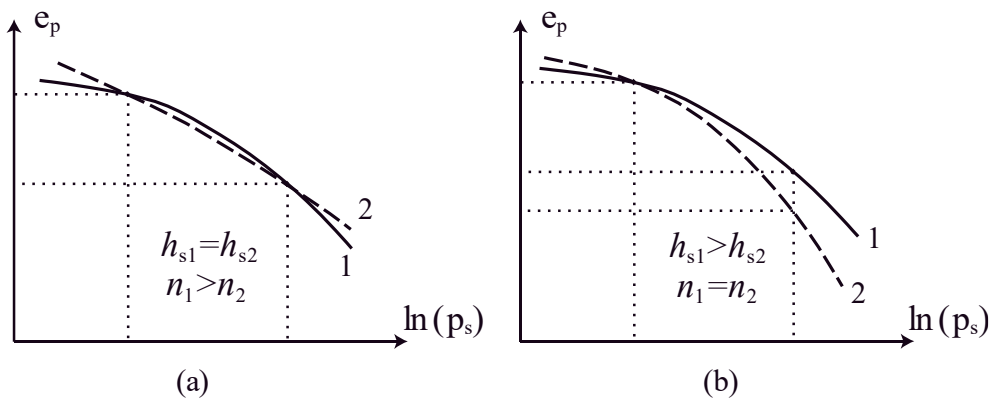
Figure 2.21. Influence of exponent n (a) and granulate hardness hs (b) on compression curve

In order to determine h_s and n parameters, an isotropic compression test or oedometer test with initially very loose specimen needs to be performed.
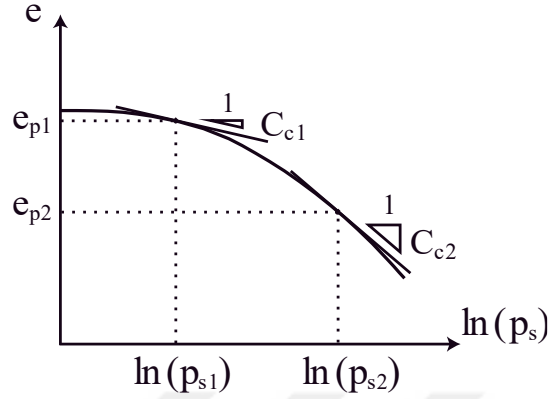
Figure 2.22. Determination of the exponent n from compression curve, Herle (1997)

Using a compression test result (e.g. Figure 2.22), h_s and n values can be calculated as follows,

$$n = \frac{\ln\left(e_{p1}C_{c2} / e_{p2}C_{c1}\right)}{\ln\left(p_{s2}/p_{s1}\right)} \tag{2.54}$$

$$h_s = 3 \cdot p_s \left(\frac{n \cdot e_p}{C_c}\right)^{1/n} \tag{2.55}$$

where,

$$p_s = \frac{1}{3}(T_{s1} + 2 \cdot T_{s2})$$

T_{s1} : vertical stress and T_{s2} : lateral stress

For an oedometer test => $T_{s2} = K_0 * T_{s1}$

$$K_0 = 1 - \sin\varphi_c$$

Note that Jaky's equation valid only for the normally consolidated soils. In order to make sure that initially loose specimen should be prepared.

In Equation 2.55, C_c and e_p values correspond to p_s where $p_{s1} \leq p_s \leq p_{s2}$

Note that, in order to calculate h_s, first we need to calculate exponent n.

In Equation 2.54, p_{s1} and p_{s2} and corresponding void ratios e_{p1} and e_{p2} values define the range at which the parameters h_s and n will be valid. So that, it is important to select a reasonable range that will include the stresses planning to be investigated.

In this thesis in order to calculate h_s and n parameters, a series of oedometer tests have been conducted. Among them, the one with the highest initial void ratio was selected to calculate these stiffness parameters. First, a polynomial equation is fitted to oedometer data and then derivative of it used to calculate C_{c1} and C_{c2} values corresponding to $p_{s1} = 10$ kPa and $p_{s2} = 600$ kPa stress ranges Figure 2.23.
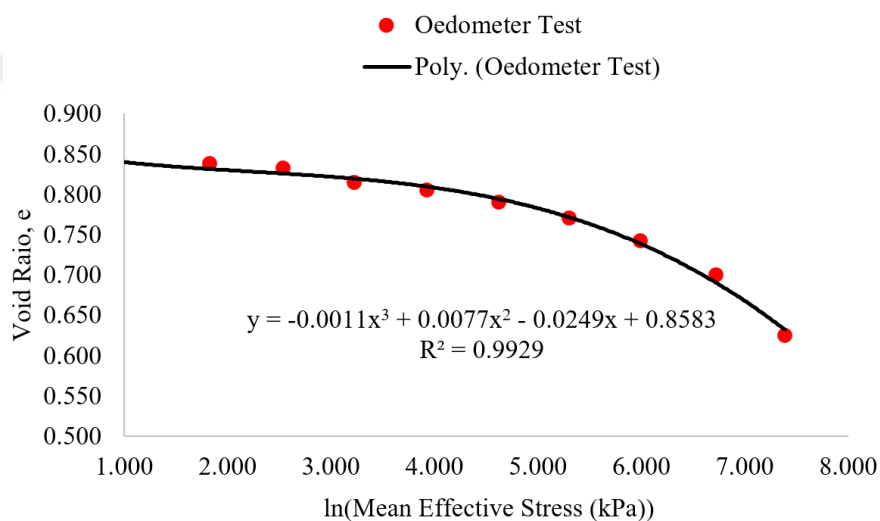
Figure 2.23. Oedometer test result and corresponding polynomial fit

The next part is the determination of the granulate hardness h_s, but the question is which p_s value should be selected between 10 and 600 kPa. In order to investigate the p_s dependent h_s variation, another graph p_s vs. h_s is plotted, Figure 2.24. At the end, the average value of the h_s within the selected range is selected.
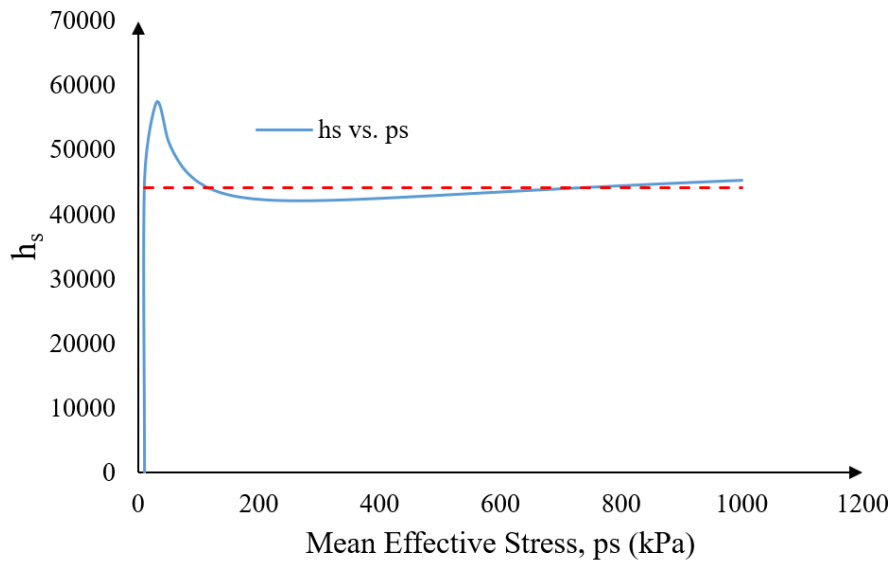
Figure 2.24. Variation of hs with mean stress, ps

2.1.3.3. Void Ratio Parameters

The void ratio is one of the three state parameters used to describe the state of the system in hypoplasticity and the way it is used is little different. In this part, other than the maximum and minimum void ratio terms which are used in classical soil mechanics; an additional term called void ratio at zero pressure will be used.

Considering the environment that we live where all the objects expose to gravitational acceleration, it is difficult to state a variable without mention about quantity of it. For example, let's discuss the following statement: "Maximum void ratio of the type A soil is 0.94". The statement would be true if the mass of soil used to measure this maximum void ratio value were given. Otherwise, as the amount of the soil increase, the maximum void ratio will decrease due to the Newton's second law ($F = m \cdot a$). Another imaginative alternative that would make this statement correct is performing this test at a gravity free environment. In that case, quantity no longer influences the result.

In the next part, methods to determine limiting void ratios e_{i0}, e_{d0} and critical void ratio e_{c0} will be discussed. Note that, in this thesis, any void ratio with zero indices refers to void ratio at zero pressure (or gravity free space).

2.1.3.3.1. Minimum Void Ratio, e_{d0}

The parameter e_{d0} is the minimum void ratio at zero pressure and slightly lower than the minimum void ratio e_{min} which is obtained from standard index tests. Among these tests, a small amplitude cyclic shearing under constant pressure is the most effective densification method (Youd 1972). For example, comparing two different densification paths: one under monotonic increasing mean stress (blue line in Figure 3.13) and other one under constant pressure with cyclic shearing (green line in Figure 3.13), how effective the cyclic shearing can be observed easily.
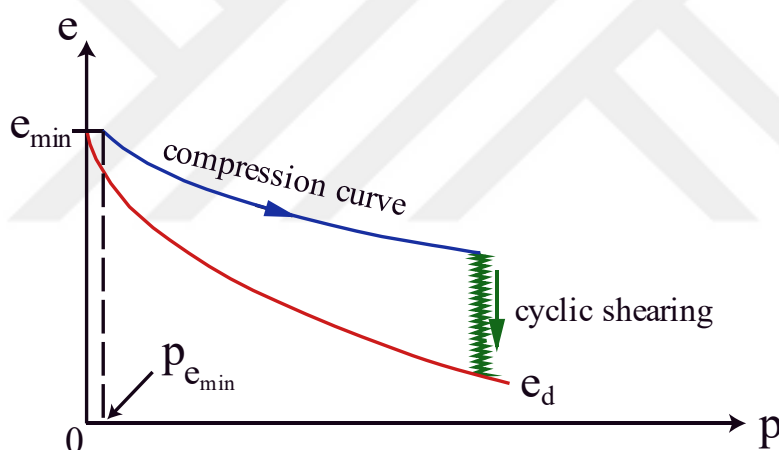
Figure 2.25. Pressure dependent change of minimum void ratio

Note that, the red line in Figure 3.13 represents the lower boundary limit (or densest state) soil can reach under the corresponding mean pressure, p and the formulation of that pressure dependent lower boundary limit is given in the Equation 2.35. Using this information, once we get the stiffness parameters (h_s, n) and perform cyclic shearing test under a constant mean pressure measure p, using the Equation 2.35 we can back calculate the minimum void ratio at zero pressure, e_{d0}.

As an alternative to the proposed back calculation method, a comparison between e_{d0} and e_{min} values obtained from index tests reveal the following useful relationship,

$$e_{d0} \approx e_{min} \tag{2.56}$$

Here, the imperfect densifications in the standard index tests are compensated by the vanishing pressure at e_{d0}. Finally, the popular standard tests used to find the minimum void ratio, e_{min} can be listed as: ASTM D4253, DIN 18126, JGS 0161 and Muszynski (2006).

2.1.3.3.2. Maximum Void Ratio, e_{i0}

The maximum void ratio at zero pressure, e_{i0} is a state where all the particles are just in contact with each other with zero contact force in a gravity free space. Considering the described environment, the experimental determination of the e_{i0} is almost impossible and the classical index tests used to calculate maximum void ratio, e_{max} always underestimates the actual value of the e_{i0} due to gravitational force. One way to approximate this quantity is idealizing the granular structure using granulometric properties of the soil such as grain shape, angularity, distribution of grain size etc.

Let's consider a case in which equal size spherical particles are packed as shown in Figure 2.26 (a). In that case the theoretical maximum void ratio, e_{i0} will be equal to,

$$(e_{i0})_{spheres} = \frac{(4r)^3 - 8 \cdot \left(\frac{4}{3}\pi r^3\right)}{8 \cdot \left(\frac{4}{3}\pi r^3\right)} \cong 0.91 \tag{2.57}$$

Comparing the above given theoretical result with experimental e_{max} value obtained from standardized tests (e.g. ASTM D4254, DIN 18126) yields,

$$e_{i0} = 1.2\, e_{max} \tag{2.58}$$

Similarly, for an idealized soil consisting of identical cubes, Figure 2.26 (b), the ratio becomes,

$$e_{i0} = 1.3\, e_{max} \tag{2.59}$$
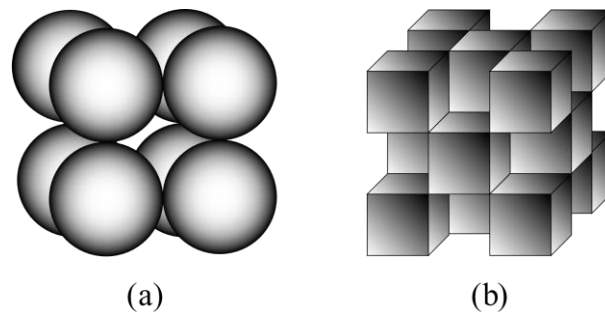
Figure 2.26. Idealized packing of spheres and cubes at minimum density

Note that, these idealized geometric representations do not take into account the grain size distribution effects. So, let's think what would be the e_{i0}/e_{max} ratio if the previous idealizations were repeated with different sizes of spheres or cubes? According to (Herle 1997), for natural quartz sands, the ratio e_{i0}/e_{max} can be assumed as 1.15.

The popular standard tests used to find the maximum void ratio, e_{max} are ASTM D4254, DIN 18126, JGS 0161 and Muszynski 2006.

2.1.3.3.3. Critical Void Ratio, e_{c0}

The parameter e_{c0} can be defined as the zero-pressure extrapolation of the critical void ratio, e_c. Analogously to the back-calculation method that is used for the determination of the e_{d0}; e_{c0} can be calculated using the e_c value at critical state. After the determination of the e_c with conventional triaxial tests, using the Equation 2.35 the critical void ratio at zero pressure, e_{c0} can be back calculated.

Although the critical state parameters φ_c and e_c can be determined from the triaxial tests, it is difficult to keep a homogeneous deformation up to the critical state (Santamarina and Cho 2001; Been et al. 1991). A comparison between e_{c0} and e_{max} for different sands, Table 2.4, reveals that maximum void ratio, e_{max} determined from standard index test can be used as an estimate of e_{c0}.

Table 2.4. *Comparison of critical void ratio at zero pressure and maximum void ratio, Herle 1997*

Material	$e_{\max}$	e_{c0}
Hostun sand	0.98	0.96
Lausitz sand	0.85	0.85
Ottawa sand	0.79	0.76
Toyoura sand	0.98	0.98
Zbraslav sand	0.82	0.80

As a result, the void ratio parameters e_{d0}, e_{i0} and e_{c0} can be estimated in terms of the $e_{\min}$ and $e_{\max}$ values determined from simple standard geotechnical tests. Based on the experimental results and theoretical estimations performed by (Herle and Gudehus 1999), following relations are obtained,

$$e_{d0} \approx e_{\min} \qquad (2.60)$$
$$e_{c0} \approx e_{\max} \qquad (2.61)$$
$$e_{i0} \approx (1.1 - 1.3) \cdot e_{\max} \qquad (2.62)$$

2.1.3.4. Exponent α

The exponent α is introduced into the constitutive model during the formulation of the pyknotropy factor, f_d in Equation 2.34. The role of the exponent α can be described as controlling the relation between the relative density and peak friction angle. In other words, the exponent α differentiates the loose and dense soil behaviors and controls the transition between peak and critical states as shown in Figure 2.27.
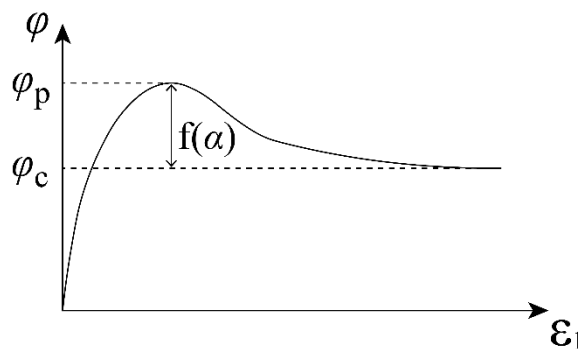
Figure 2.27. Transition from peak to critical state with exponent α

In order to determine exponent α, a triaxial test with a dense specimen needs to be performed. It is important to use dense specimen for the investigation of the peak state. In that case, before reaching the critical state soil will experience a peak state where the vertical stress rate, $\dot{T}_1$ will be vanished. So, introducing the peak state condition $\dot{T}_1 = 0$, into Equation 2.50, α can be obtained as,

$$\alpha = \frac{\ln\left(3\dfrac{D_1 + a^2 T_1{}^2 D_1 + 2a^2 T_1 T_2 D_2}{a(5T_1 - 2T_2)\sqrt{D_1{}^2 + 2D_2{}^2}}\right)}{\ln\left(\dfrac{e - e_d}{e_c - e_d}\right)} \tag{2.63}$$

Inserting the peak ratios,

$$K_p = \frac{T_1}{T_2} \quad , \quad \sin\varphi_p = \frac{T_1 - T_2}{T_1 + T_2} \quad \text{and} \quad \tan\nu_p = -\frac{D_1 + 2D_2}{D_1} \tag{2.64}$$

where,

K_p: peak ratio, φ_p: peak friction angle and ν: dilatancy angle

into the Equation 2.63, α can be rewritten as,

$$\alpha = \frac{\ln\left(6\dfrac{(2 + K_p)^2 + a^2 K_p(K_p - 1 - \tan\nu_p)}{a(2 + K_p)(5K_p - 2)\sqrt{4 + 2(1 + \tan\nu_p)}}\right)}{\ln\left(\dfrac{e - e_d}{e_c - e_d}\right)} \tag{2.65}$$

2.1.3.5. Exponent β

The exponent β is introduced into the constitutive model during the formulation of the pyknotropy factor, f_s in Equation 2.33. The role of this parameter is to control the incremental stiffness modulus. Using Equation 2.50, the effect of f_s can be clarified as, $\dot{T}_1 = f_s \cdot f(T_1, T_2, D_1, D_2)$ with incremental stiffness, $E = \dot{T}/D$. What this simplification tells us is the stress increment at any point (in this case the current stress and strain rate are represented by T_1, T_2 and D_1, D_2) is not just controlled by the current

stress and strain rate but also with a factor so-called f_s. Let's also simplify the parameter f_s,

$$f_s = \left(\frac{e_i}{e}\right)^\beta \cdot f(e_i, \mathbf{T}, \text{material constants}) \tag{2.66}$$

Here the factor f_s is controlled with exponent β, current stress state $\mathbf{T}$, current void ratio e and corresponding upper boundary limit e_i. The function of β is to control the effect of density on the soil stiffness. For example, in case of a dense material where $e \ll e_i$, the influence of β will be higher compared to a loose material with $e \approx e_i$.

In order to determine the exponent β, isotropic compression test can be used. In case of an isotropic compression test ($T_1 = T_2 = T_3$), using Equation 2.50, the stress rate can be written as,

$$\dot{T}_1 = f_s(3 + a^2 - f_d a\sqrt{3})D_1 \tag{2.67}$$

Then the incremental stiffness E becomes,

$$E = \frac{\dot{T}_1}{D_1} = f_s(3 + a^2 - f_d a\sqrt{3}) \tag{2.68}$$

Substituting the Equation 2.33 into the incremental stiffness, the exponent β becomes,

$$\beta = \frac{\ln\left(E\dfrac{3 + a^2 - f_{d0} a\sqrt{3}}{3 + a^2 - f_d a\sqrt{3}}\dfrac{e_i}{1 + e_i}\left(\dfrac{3p}{h_s}\right)^{n-1}\right)}{\ln\left(e_i/e\right)} \tag{2.69}$$

where,

$$f_{d0} = \frac{e_{i0} - e_{d0}}{e_{c0} - e_{d0}}$$

In order to simplify the calculation of β, you may also perform two different tests with different initial densities and formulate β at same mean pressure, p and then Equation 2.69 takes the following form,

$$\beta = \frac{\ln\left(\dfrac{E_2}{E_1}\left(\dfrac{3 + a^2 - f_{d1} a\sqrt{3}}{3 + a^2 - f_{d2} a\sqrt{3}}\right)\right)}{\ln\left(e_1/e_2\right)} \tag{2.70}$$

Although it is not suggested, oedometer test can also be used for the determination of the exponent β.

Unless the sample is very dense, the effect of parameter β is negligible. So that, in case of a very loose sample, it is sufficient to assume $\beta \approx 1$.

Concluding remark for the first part of the parameter determination:

As you noticed hypoplasticity requires a certain number of parameters. The above-mentioned formulations which are derived from the constitutive equation itself are used for the determination of these parameters. Considering the inevitable small errors that occur during the experiments, it is certain that these calculated parameters have some $\pm$ errors. In order to eliminate the effect of these errors, after the determination of each parameter, I have numerically simulated each test using these parameters and then calibrated some of them to get more consistent results.

In this thesis, the tests performed for the determination of the hypoplastic constitutive model parameters are summarized in Table 2.5.

Table 2.5. *Summary of parameter determination*

Parameter	Test and Methodology
φ_c	Angle of repose test proposed by Miura (1997)
h_s, n	Oedometer test with initially loose dry soil
e_{d0}, e_{c0}, e_{i0}	Standard index tests, for comparison purposes tests proposed by JGS and Muszynski (2006) are performed.
α	Drained triaxial test with initially dense specimen
β	Two drained triaxial tests with initially different densities.

So far, all the parameters required for the basic hypoplasticity is investigated and the way to calculate them is explained in detail. In the next part, intergranular model parameters required for the extended hypoplasticity will be investigated.

2.1.3.6. Intergranular Strain Parameters

The intergranular strain effects upon stress or strain reversals are introduced to hypoplasticity with additional five parameters. Similar to the previous eight parameters, these five parameters are also determined from the experimental test results using calibration techniques and parametric studies. As a brief summary,

- The parameter R corresponds to the maximum value of the intergranular strain **h** and represents the intergranular strain range in which the soil behaves elastically. For the determination of this parameter it is suggested to perform a small strain triaxial test with several path reversals. Immediately after the path reversals (180° change in strain direction) the stiffness of the system remains constant within the range of R as shown in Figure 2.12 with E_R.

- The parameter m_R controls the stiffness increase upon 180° change in strain path, Figure 2.12. In addition, for soil without a deformation history **h** = 0 or $\rho = 0$, the initial stiffness of the soil is also governed by $m_R E_0$. In order to determine the stiffness factor m_R, a small strain triaxial test with a path reversal can be used. Immediately after the reversal, the stiffness becomes $m_R E_0$. In order to calculate E_0, an additional small strain monotonic triaxial test with the same initial density should be performed. But note that, reliability of the results is questionable due to the limit of accuracy of the strain transducers. As an alternative shear wave experiment such as bender element test is suggested by (Mašín 2019).

- The parameter m_T controls the stiffness increase upon 90° change in strain path, Figure 2.12. Compare to the m_R the determination of the stiffness factor m_T is more difficult. Unfortunately, wave propagation tests cannot be used for the determination of m_T. The way of calculation is similar to the m_R, after the 90° change in strain path stiffness of the soil increases to $m_T E_0$. Triaxial tests with accurate local strain measurements are required.

- The exponent χ ($\chi > 1$) which is incorporated into the constitutive framework in Equation 2.41, is used to interpolate the stiffness degradation from E_R to E_0.

Upon 180° strain reversal, using Equation 2.41, the stiffness degradation given in Figure 2.12 can be approximated as follows:

$$E = \begin{cases} m_R E_0 \ (\text{or } E_R) & \text{for } \varepsilon < R \quad (a) \\ E_0 + E_0(m_R - 1)[1 - \rho^\chi] & \text{for } \varepsilon > R \quad (b) \end{cases} \tag{2.71}$$

For the determination of the exponent χ, a triaxial test with a complete strain reversal can be used. Following to strain reversal, a continued monotonic deformation for $\varepsilon > R$ results in a stiffness degradation approximated by Equation 2.71(b), this relation can be used for the calibration of exponent χ.

- The parameter β_R controls the evolution of intergranular strain as shown in Equation 2.49. In this equation, β_R introduces a kind of power law interpolation with ρ^{β_R}. Following the determination of the R, χ and ε_{SOM}, the exponent β_R can be predicted using the diagram given in Figure 2.28. As an alternative, stiffness degradation curve can also be used for the calibration of β_R.
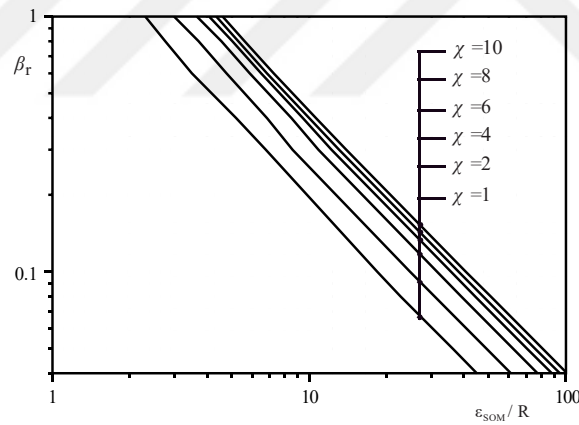
Figure 2.28. Corrolation of Br vs. εsom/R for different X, Niemunis & Herle (1997)

Due to the complexity of the intergranular strain parameters, very limited data of calibrated sands are available in the literature. Besides their complexity, the determination of these five additional parameters is also difficult and requires sensitive LVDT, sophisticated dynamic and static test setups (e.g. bender element test setup, cyclic triaxial tests). Therefore, for most practical applications, parametric studies are performed to calibrate these parameters.

50

For a complete description of the experimental and parametric determinations of these additional five parameters it is recommended to read:

- Extended hypoplastic models for soils (Niemunis 2002)
- Modelling of soil behaviour with hypoplasticity (Mašín 2019)

In this thesis, a calibration procedure based on the limited data available in the literature is carried out, Table 2.6. Checking the granulometric properties of the sands, an initial set of parameters are selected as follows:

R	m_R	m_T	β_R	χ
10^{-4}	5.0	2.0	0.5	6.0

Then using the stiffness degradation curves and cyclic test results model parameters are calibrated over R and χ so that the numerical results are fitted to the experimental test results, Appendix A.

Table 2.6. *Extended hypoplastic model parameters for different types of sands*

Material	R	m_R	m_T	β_R	χ
Berlin Sand	10^{-4}	5.0	2.0	0.4	6.0
Toyoura Sand	$2\mathrm{x}10^{-5}$	8.0	4.0	0.1	1.0
Baskarp Sand	10^{-4}	6.0	6.0	0.15	1.0
Castro Sand	10^{-4}	5.0	2.0	0.5	6.0
Hochstetten Sand	10^{-4}	5.0	2.0	0.5	6.0

During the calibration procedure, it is important to know the range of the parameters. Otherwise, even though numerical prediction fits well with a single experimental test, results will be inconsistent for remaining tests. Considering true soil behavior following ranges will be helpful while calibrating the model parameters:

- The stiffness factors $m_R > m_T > 1$
- The exponent $\chi > 1$
- The exponent $\beta_R < 1$
- The maximum intergranular strain $R \approx 10^{-5} - 10^{-4}$

2.2. Two-Phase Model

The nature of the soil consists of three phases which are solid grains, liquid and gas. Since this study investigates the behavior of the fully saturated sands, two phase system consisting of a solid phase, skeleton and a fluid phase occupying the pores are adopted as shown in Figure 2.29. The heterogeneous structure of the soil and dissipation of the fluid within the porous media are idealized with the principles of continuum mechanics.
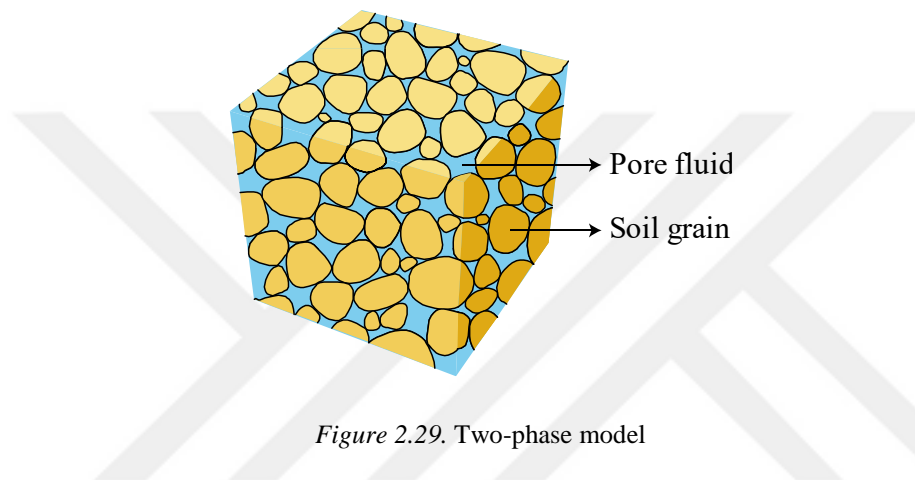
Figure 2.29. Two-phase model

The existence of water highly influences the mechanical behavior of the soil. Considering a fully saturated system, deformation occurs depending on the rate at which the water is being squeezed out of the voids. In order to accurately simulate this dissipation phenomenon in which pressurized water flows through pore voids, a so-called two-phase model is required. A two-phase implemented finite element accounts for the pore pressure accumulations and allows effective stress based constitutive models to simulate mechanical behavior properly.

Two-phase model was first formulated by (Biot 1941) for quasi-static condition and the presence of the fluid flow was taken into account with a Darcy's law implemented poroelasticity theory. Later, the model was extended for the investigation of the transient effects (i.e. wave propagation within the porous media) by introducing dynamic coupling between fluid and solid particles (Biot 1956; Biot 1962).

Zienkiewicz & Shiomi (1984) further modified (and also simplified) the model to take into account material nonlinearity and large deformation problems.

In this thesis, the u-p model developed by Zienkiewicz & Shiomi (1984) is used for the coupled FE analysis. Here, u and p stand for the absolute displacements of the solid skeleton and pore water pressure respectively. In this model, Terzaghi's principle of effective stresses is used and the fluid velocity is described by the Darcy's law.

The total stress (Equation 2.72) applied to the two-phase system is split into two part: pore pressures (Equation 2.73) and skeleton (or effective) stress (Equation 2.74).

$$\boldsymbol{\sigma} = \begin{bmatrix} \sigma_x & \sigma_y & \sigma_z & \tau_{xy} & \tau_{yz} & \tau_{zx} \end{bmatrix}^T \qquad (2.72)$$

$$\mathbf{p} = -\alpha \mathbf{m} p \qquad (2.73)$$

$$\boldsymbol{\sigma}' = \boldsymbol{\sigma} + \alpha \mathbf{m} p \qquad (2.74)$$

where,

The parameter $\alpha = 1 - K/K_s$ controls the deformation of the skeleton. K and K_s are the bulk modulus of skeleton and single grain respectively. If the grains are considered as incompressible ($K_s \gg K$),
$$\alpha \to 1 \text{ and } \mathbf{p} = -\mathbf{m} p$$

The parameter $\mathbf{m} = \begin{bmatrix} 1 & 1 & 1 & 0 & 0 & 0 \end{bmatrix}^T$ is used to convert scalar hydrostatic pressure, p into a vector form, $\mathbf{p}$.

In the porous media, the velocity of fluid relative to the solid particles is referred as Darcy (or filter) velocity, $\mathbf{w}$. Using Darcy's law, filter velocity of a flow taking place between two points with a pressure difference of ∇p is defined as,

$$\mathbf{w} = \mathbf{v}_f - \mathbf{v}_s = \frac{\mathbf{k}_p}{\eta_w}(-\nabla p + \rho_w \mathbf{b}) \qquad (2.75)$$

where,

$\mathbf{v}_f$: Velocity of fluid	η_w : Dynamic viscosity of water
$\mathbf{v}_s$: Velocity of solid	∇p : Gradient of pore pressure
$\mathbf{k}_p$: Permeability matrix	$\mathbf{b}$: Body force acceleration
ρ_w : Density of water	

The conservation equations required to be solved in order to formulate the coupled two-phase model are given as follows:

- Using the Terzaghi's effective stress definition (Equation 2.74), the balance of momentum for the solid-fluid mixture can be written as:

$$\mathbf{L^T}(\boldsymbol{\sigma}' - \mathbf{m}p) + \rho\mathbf{b} = \rho\ddot{\mathbf{u}} + \zeta\dot{\mathbf{u}} + \rho_w[\dot{\mathbf{w}} + \mathbf{w}\nabla^T\mathbf{w}] \qquad (2.76)$$

where,

$\boldsymbol{\sigma}'$: Effective stress vector ρ : Density of the total body

ζ : Damping ratio

$\mathbf{L^T}$ is a divergence operator and given as,

$$\mathbf{L^T} = \begin{bmatrix} \partial/\partial x & 0 & 0 & \partial/\partial y & 0 & \partial/\partial z \\ 0 & \partial/\partial y & 0 & \partial/\partial x & \partial/\partial z & 0 \\ 0 & 0 & \partial/\partial z & 0 & \partial/\partial y & \partial/\partial x \end{bmatrix}$$

The term $\rho_w[\dot{\mathbf{w}} + \mathbf{w}\nabla^T\mathbf{w}]$ given in right hand side of the Equation (2.76), represents the acceleration of the relative movement between the components of two-phase model. According to (Zienkiewicz et al. 1999; Lewis and Schrefler 1998), this value is small enough to neglect and also elimination of this inertial component increases the computational efficiency. For $\rho_w[\dot{\mathbf{w}} + \mathbf{w}\nabla^T\mathbf{w}] \to 0$, Equation (2.76) is simplified to,

$$\mathbf{L^T}(\boldsymbol{\sigma}' - \mathbf{m}p) + \rho\mathbf{b} = \rho\ddot{\mathbf{u}} + \zeta\dot{\mathbf{u}} \qquad (2.77)$$

- For the flow conservation, ignoring the effects of thermal changes, the mass balance (or continuity equation) of the flow can be written as:

$$\nabla^T\mathbf{w} + \mathbf{m^T}\mathbf{L}\dot{\mathbf{u}} + \frac{\dot{\mathbf{p}}}{Q^*} = 0 \qquad (2.78)$$

- Combining the conservation Equations (2.75) and (2.78) we obtain,

$$\nabla^T\frac{\mathbf{k_p}}{\eta_w}(-\nabla p + \rho_w\mathbf{b}) + \mathbf{m^T}\mathbf{L}\dot{\mathbf{u}} + \frac{\dot{\mathbf{p}}}{Q^*} = 0 \qquad (2.79)$$

where,

Q^* : Volumetric stiffness of the two-phase system $\quad\nabla p$: Gradient of pore pressure

Here the coupled volumetric stiffness of the two-phase system expressed as,

$$\frac{1}{Q^*} = \frac{n}{K_w} + \frac{1-n}{K_s} \tag{2.80}$$

K_w : Bulk modulus of water $\quad K_s$: Bulk modulus of solid grains

n : Porosity of the soil

Note that the permeability matrix, $\mathbf{k}_p$ given in the Equation (2.79) is defined as Darcy's permeability which is different from the hydraulic conductivity that we use in soil mechanics. For an isotropic case, the permeability matrix, $\mathbf{k}_p$ can be defined as,

$$\mathbf{k}_p = k_p \cdot \mathbf{I} \tag{2.81}$$

where,

k_p : Darcy's permeability (m^2) $\quad\mathbf{I}$: Unit matrix

The relation between the hydraulic conductivity of the soil and Darcy's permeability can be defined as,

$$k_d = \frac{\rho_w \cdot g}{\eta_w} k_p \tag{2.82}$$

k_d : Hydraulic conductivity (m/s) $\quad g$: Gravitational acceleration

The conservation equations (2.77) and (2.79) are differential equations that are used for the formulation of the two-phase, u-p model. While using these equations, be aware that they are obtained through some modifications such as the variable **w** is eliminated, so that only two variables are left: u and p, both solid and fluid are considered as incompressible. All these simplifications and modifications are performed either for increasing computational efficiency or omitting negligible quantities like thermal effects.

The finite element implementation of the u-p model is essential when we consider the complex problems that we are dealing with. To do that first, previously defined

differential equations needs to be converted into their weak form. And then the weak form of the original conservation equations should be approximated using weighted residual methods. The detailed weak formulation and discretization of the Equations (2.77) and (2.79) are provided in (Albers et al. 2012; Taşan H. E. 2011; Potts and Zdravković 1999; Papadrakakis and Stavroulakis 2009). In these articles, weighted residual method (or in particular Galerkin method) is used to obtain weak formulations. In the next part, the discretized system obtained from Equations (2.77) and (2.79) are summarized.

Consider a domain Ω surrounded by a boundary Γ is filled with a two-phase mixture. Within that domain displacement and pore pressure fields are approximated as,

$$\mathbf{u} = \mathbf{N}_\mathrm{u}\bar{\mathbf{u}} \tag{2.83}$$

$$p = \mathbf{N}_\mathrm{p}\bar{\mathbf{p}} \tag{2.84}$$

where,

$\mathbf{N}_\mathrm{u}$ and $\mathbf{N}_\mathrm{p}$ represents the appropriate shape functions.

$\bar{\mathbf{u}}$ and $\bar{\mathbf{p}}$ are corresponding nodal vector of unknowns

The resulting local coupled system of equations are formulated as,

$$\mathbf{M}\ddot{\bar{\mathbf{u}}} + \mathbf{C}\dot{\bar{\mathbf{u}}} + \mathbf{K}\bar{\mathbf{u}} - \mathbf{Q}\bar{\mathbf{p}} = \mathbf{f}_\mathrm{u} \tag{2.85}$$

and

$$\mathbf{Q}^\mathrm{T}\dot{\bar{\mathbf{u}}} + \mathbf{S}\dot{\bar{\mathbf{p}}} + \mathbf{H}\bar{\mathbf{p}} = \mathbf{f}_\mathrm{p} \tag{2.86}$$

or combining the Equations (2.85) and (2.86),

$$\begin{bmatrix} \mathbf{M} & \mathbf{0} \\ \mathbf{0} & \mathbf{0} \end{bmatrix} \begin{bmatrix} \ddot{\bar{\mathbf{u}}} \\ \ddot{\bar{\mathbf{p}}} \end{bmatrix} + \begin{bmatrix} \mathbf{C} & \mathbf{0} \\ \mathbf{Q}^\mathrm{T} & \mathbf{S} \end{bmatrix} \begin{bmatrix} \dot{\bar{\mathbf{u}}} \\ \dot{\bar{\mathbf{p}}} \end{bmatrix} + \begin{bmatrix} \mathbf{K} & -\mathbf{Q} \\ \mathbf{0} & \mathbf{H} \end{bmatrix} \begin{bmatrix} \bar{\mathbf{u}} \\ \bar{\mathbf{p}} \end{bmatrix} = \begin{bmatrix} \mathbf{f}_\mathrm{u} \\ \mathbf{f}_\mathrm{p} \end{bmatrix} \tag{2.87}$$

within that system of equations,

$\mathbf{M}$: Mass matrix $\mathbf{C}$: Damping matrix

$\mathbf{K}$: Stiffness matrix $\mathbf{Q}$: Coupling matrix

$\mathbf{f}_\mathrm{u}$: The load vector of solid $\mathbf{H}$: Permeability matrix

$\mathbf{f}_{\mathrm{p}}$: The load vector of fluid

Formulation of these matrices are given as,

$$\mathbf{M} = \int_{\Omega} \mathbf{N}_{\mathrm{u}}^{\mathrm{T}} \rho \mathbf{N}_{\mathrm{u}} \mathrm{d}\Omega \qquad\qquad \mathbf{C} = \int_{\Omega} \mathbf{N}_{\mathrm{u}}^{\mathrm{T}} \zeta \mathbf{N}_{\mathrm{u}} \mathrm{d}\Omega$$

$$\zeta : \text{Damping ratio}$$

$$\mathbf{K} = \int_{\Omega} \mathbf{B}^{\mathrm{T}} \mathbf{D}_{\mathrm{t}} \mathbf{B} \mathrm{d}\Omega \qquad\qquad \mathbf{Q} = \int_{\Omega} \mathbf{B}^{\mathrm{T}} \mathbf{m} \mathbf{N}_{\mathrm{p}} \mathrm{d}\Omega$$

$$\mathbf{S} = \int_{\Omega} \mathbf{N}_{\mathrm{p}}^{\mathrm{T}} \frac{1}{Q^*} \mathbf{N}_{\mathrm{p}} \mathrm{d}\Omega \qquad\qquad \mathbf{H} = \int_{\Omega} \mathbf{B}_{\mathrm{p}}^{\mathrm{T}} \mathbf{k}_{\mathrm{p}} \mathbf{B}_{\mathrm{p}} \mathrm{d}\Omega$$

$$\mathbf{f}_{\mathrm{u}} = \int_{\Omega} \mathbf{N}_{\mathrm{u}}^{\mathrm{T}} \rho \mathbf{b} \mathrm{d}\Omega + \oint_{\Gamma} \mathbf{N}_{\mathrm{u}}^{\mathrm{T}} \tilde{\sigma} \mathrm{d}\Gamma \qquad \mathbf{f}_{\mathrm{p}} = \int_{\Omega} \mathbf{B}_{\mathrm{p}}^{\mathrm{T}} \mathbf{k}_{\mathrm{p}} \rho_{\mathrm{w}} \mathbf{b} \mathrm{d}\Omega - \oint_{\Gamma} \mathbf{N}_{\mathrm{p}}^{\mathrm{T}} \tilde{q} \mathrm{d}\Gamma$$

Note that, $\mathbf{B} = \mathbf{L}\mathbf{N}_{\mathrm{u}}$ and $\mathbf{B}_{\mathrm{p}} = \nabla \mathbf{N}_{\mathrm{p}}$ are derivative of the shape functions; $\tilde{\sigma}$ and $\tilde{q}$ are surface traction and pore pressure at Γ and $\mathbf{D}_{\mathrm{t}}$ is the tangential modulus matrix.

To solve the system of Equations (2.87), a time integration procedure is carried out by using the Newmark method (Taşan H. E. 2011).

Based on the pre-defined u-p model, a three-dimensional 20-node coupled element called u20p8 is implemented in ANSYS. Triquadratic and trilinear shape functions have been used for the displacement and pore pressure respectively. In u20p8 coupled element: 20 represents the total number of nodes within the element and 8 represents the number of the nodes with additional pressure degree of freedom. To sum up, this element is defined by 20 nodes having four degrees of freedom (u_x, u_y, u_z and p) at each corner, Figure 2.30.

u20p8 Element

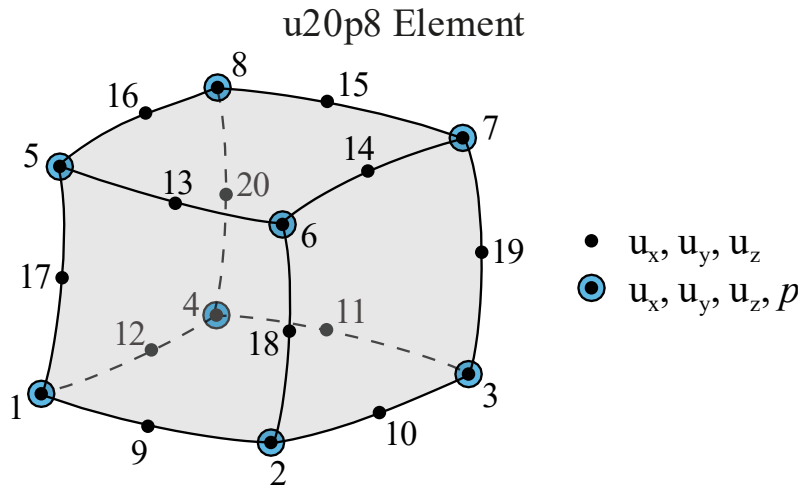u_x, u_y, u_z

u_x, u_y, u_z, p

Figure 2.30. Three-dimensional coupled two-phase element, u20p8

The choice of a higher order (20 nodes) is due to ensure the stability of the element (Zienkiewicz et al. 1986). Coupled problems under static and dynamic loading present pore pressure oscillations if the permeability is very low and the fluid is quasi-incompressible when formulated in the framework of a low order numerical model with equal order interpolation in displacements and pore pressure. In order to avoid this problem, the order of interpolation for the displacement field must be higher than for the pressure field (Zienkiewicz and Shiomi 1984).

Finally, let's discuss the reason why we need to implement a coupled element in a finite element software such as ANSYS or ABAQUS. Even though these highly advance softwares have some predefined coupled elements (e.g. CPT212-217 in ANSYS), they are not allowed to be used with the user-defined constitutive models. So, you have to either select a constitutive model that already available in the ANSYS material model library (currently, none of them is suitable to investigate the cyclic behavior of soil) and then you can use available coupled CPT elements or implement a constitutive model that meets your expectations and then also implement a suitable element for the coupled analyses, just like we did in this thesis work.

The verification of the finite element model with u-p approximated coupled two-phase element (u20p8) is performed in Chapter 3.

2.3. Porosity-Permeability Relationship

Permeability is one of the main parameters that control the drainage, pore pressure build-up, dissipation, and settlements, briefly overall mechanical behavior of saturated soils. Therefore, in the previous section, a permeability dependent dissipation function is incorporated into the system with the implementation of the two-phase model. Although this implementation has provided ability of taking into account pore pressure developments and dissipation induced nonlinear deformations, a single predefined permeability constant is used for all of those operations.

Under cyclic and dynamic loading conditions, loosening and re-compaction take place which lead to change in porosity. Depending on that change, permeability of soil also changes. To properly simulate this dynamic behavior, it is important to take permeability variation into account (Shahir et al. 2012). Otherwise, using initial permeability coefficient obtained through standard geotechnical tests (e.g. constant head permeability test) in dynamic problems such as earthquake simulations may cause erroneous pore pressure and settlement calculations. For example, according to an experiment carried out by (Ueng et al. 2015) permeability of soil increased 4 times its original value during the liquefaction and then decreased back to 0.9 times its original value after all the excess pore pressures dissipated. Also, (Ishihara, Review of the predictions for model 1 in the VELACS Program 1994) reviewed the VELACS centrifuge shaking table tests where the permeability again increased 6 to 7 times its original value during the liquefaction and commented on the necessity of the consideration of the permeability variation.

Even though there are variety of equations in the literature that establish a relation between porosity and permeability, numerical implementation of these equations to geotechnical problems is rare.

Evaluation of variation of permeability is a highly complicated topic and depends on many factors. Before going into further detail about it, let's first discuss the factors affecting the permeability and fluid flow within the porous media.

2.3.1. Factors affecting Permeability

Permeability is affected by several factors. The most effective factors can be listed as:

- degree of saturation
- particle size and shape
- particle size distribution
- void ratio
- mineral composition
- properties of permeating fluid (mainly viscosity and density)
- geometrical structure of the porous network
- surface interaction between the permeating fluid and the soil skeleton

Among these factors except the void ratio, all the remaining parameters can be assumed constant during deformation. Although the geometrical structure of the porous network changes, especially during the large shear deformations, within the continuum framework, its effect on permeability is neglected.

Many researchers (Hazen 1892; Kozeny 1927; Carman 1956; Terzaghi et al. 1964; Kenney et al. 1984; Alyamani and Sen 1993) have attempted to develop empirical equations for predicting permeability from grain size distribution parameters. In the next part selected two relationships reflecting the influence of the soil characteristics on permeability is discussed in a comparative way.

2.3.2. Hazen's Equation

Allen Hazen (1982) developed an empirical relationship for predicting the permeability of granular materials:

$$k = C_H \cdot (D_{10})^2 \tag{2.88}$$

where,

k : coefficient of permeability (m/sec)

C_H : Hazen's empirical coefficient (ranges from 40 to 120) ≈ 100

D_{10} : Particle size (cm) for which 10% of the soil is finer

It has been more than a century since it was developed, and Hazen's equation is still one of the most commonly used empirical equation to determine permeability. However, this method does not account for the permeability change that we are looking for and includes several limitations that create a potential source of bias such as it does not cover the whole fraction of a soil sample, but only the D_{10}.

2.3.3. Kozeny-Carman Relationship

The Kozeny-Carman equation is a well-known, widely accepted, semi-empirical, semi-theoretical formula developed for predicting the permeability of porous media. The equation is first developed by (Kozeny 1927) and later modified by (Carman 1937) and took the following form:

$$k = \frac{\gamma}{\mu} \frac{1}{C_{KC}} \frac{1}{S_0{}^2} \left(\frac{e^3}{1+e}\right) \tag{2.89}$$

where,

γ : unit weight of permeant

μ : viscosity of permeant

C_{KC} : Kozeny-Carman coefficient

S_0 : specific surface area per unit volume of particles (1/cm)

e : void ratio

The specific surface area S_0 is not a common parameter and there is no specific ASTM standard for the calculation of it. However, the geotechnical textbooks use some idealizations as follows:

- Assuming all the particles are equal spheres, S_0 becomes:

$$S_0 = \frac{\text{Surface Area}}{\text{Volume}} = \frac{\pi D^2}{1/6 \, \pi D^3} = \frac{6}{D}$$

- Considering the fact that the particle shapes are not spherical, S_0 can be re-calculated using a shape factor, SF.

$$S_0 = \frac{SF}{D}$$

For the determination of the particle shape factor SF, (Fair et al. 1933) carried out an experimental study on different type of sands and suggested following values given in Table 2.7.

Table 2.7. *Particle shape factors, Fair, Hatch, & Hudson, (1933)*

Shape of Sand	Shape Factor
Spherical	6.0
Rounded	6.1
Sharp	7.0
Angular	7.7

- In this step, instead of a constant D value, an effective particle diameter D_{eff} is defined, so that the particle size distribution (both varying particle sizes and corresponding % portions) is taken into account.

$$D_{eff} = \frac{100\ \%}{\sum (f/D_{ave})_i}$$

in which,
   f : fraction of particles between two sieve sizes %
   D_{ave} : average particle diameter corresponding to smaller and larger sieve sizes (cm)

$$D_{ave} = D_{larger,i}{}^{0.404} \times D_{smaller,i}{}^{0.595}$$

Note that the exponents, 0.404 and 0.595 are selected considering the log-linear particle size distribution.

Finally, Equation 2.89 takes the following form,

$$k = \frac{\gamma}{\mu}\ \frac{1}{C_{KC}} \left(\frac{100\ \%}{\sum \left[f_i / \left(D_{larger,i}{}^{0.404} \times D_{smaller,i}{}^{0.595} \right) \right]} \right)^2 \frac{1}{SF^2} \left(\frac{e^3}{1+e} \right) \qquad (2.90)$$
$$\gamma/\mu = 9.93 \times 10^4\ \text{1/cm·s for 20°C}$$

It is now clear how the theory of the model is based on the direct relation between the media properties and flow resistance in pore channels. Comparing to Hazen's equation, in Kozeny-Carman equation, rather than the effective particle size D_{10}, the entire particle size distribution and particle shape are taken into account.

Similar to many other permeability relationships, the Kozeny-Carman equation is also valid for the laminar flow conditions. However, under dynamic and cyclic loading as a result of the repetitive pore pressure build-up and relaxation, the condition of flow continuously changes. At this point, it would be more convenient to develop a relationship that accounts for the dynamic flow conditions. Although the actual dissipation mechanism, which is resulted from pore water generation/dissipation, is not simulated adequately (due to the complex porous flow), it is noted that Kozeny-Carman equation can still improve the cyclic and dynamic prediction of the soil behavior.

The main reason of selecting Kozeny-Carman relationship among the many alternatives is due to fairly good results obtained in estimating the permeability of sandy soils. Some of these results taken from various studies are shown in Figure 2.31, 2.32, 2.33 and 2.34.
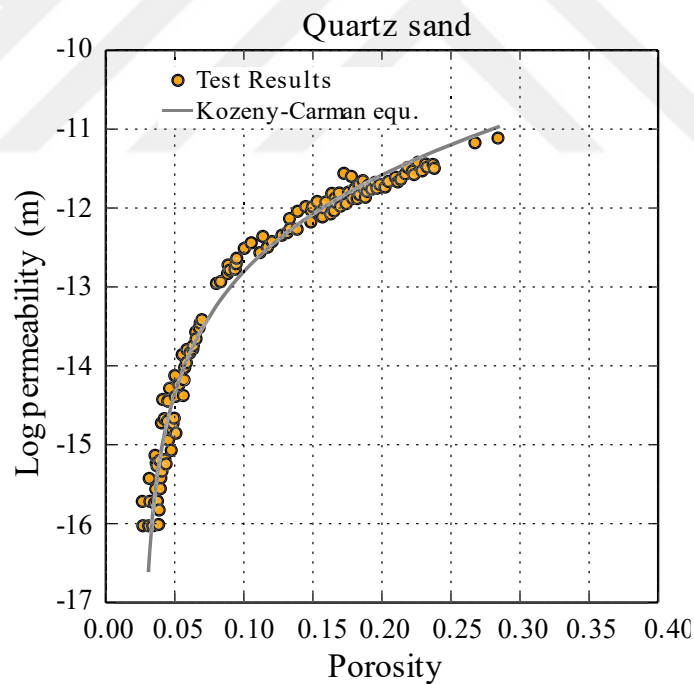

Figure 2.31. Comparison of measured and predicted permeabilities, Luijendijk & Gleeson (2015)

According to the experimental research carried out by (Luijendijk and Gleeson 2015), Figure 2.31, predictions obtained using Kozeny-Carman equation are quite accurate.
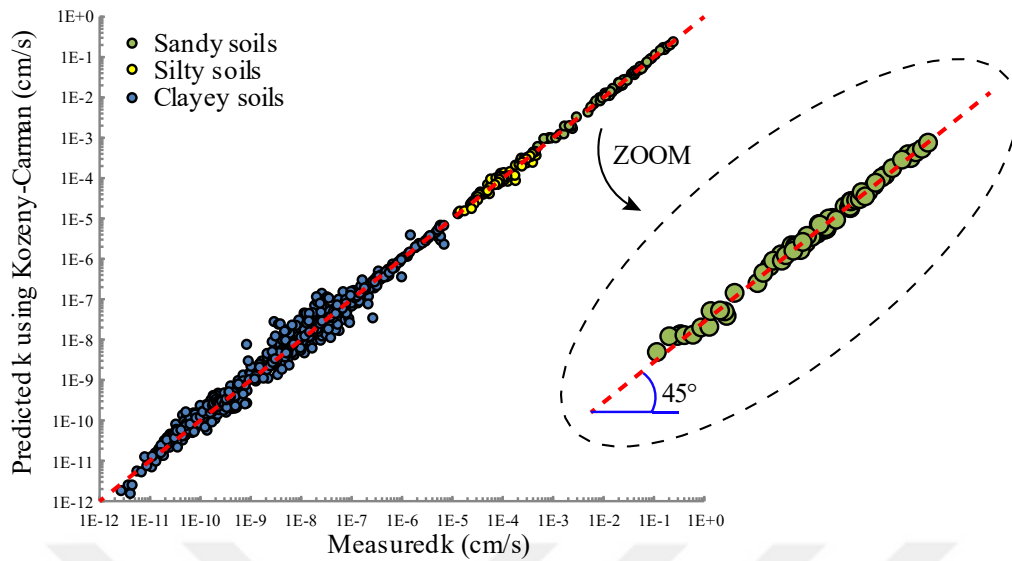
Figure 2.32. Comparison of measured and predicted permeabilities, Ren et al., (2016)

Another set of permeability tests are carried out by (Ren et al. 2016) which is given in Figure 2.32, also shows a good agreement with Kozeny-Carman equation. Note that, Kozeny-Carman equation is not suggested for the soils with high fines content, as you can see from the Figure 2.32, there is a relatively high deviation in clayey soils and deviation decreases as the particle size increases, towards to sandy soils.
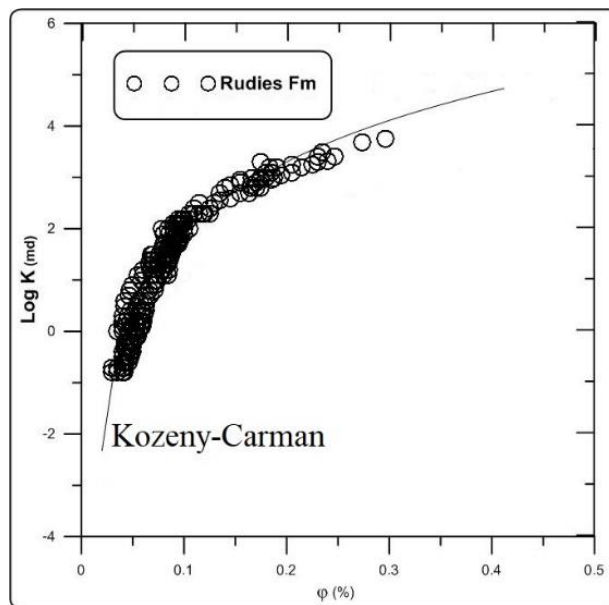

Figure 2.33. Comparison of measured and predicted permeabilities, (Lala, 2017)
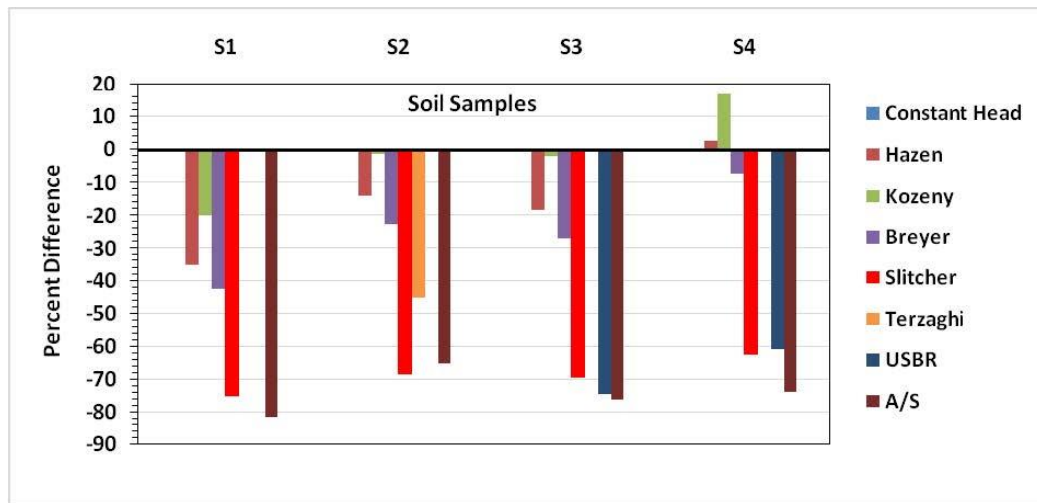
Figure 2.34. Comparison of empirical relations, Hussain & Nabi, (2016)

Finally, (Hussain and Nabi 2016) carried out a research and compared different permeability prediction equations based on the constant head permeability test as shown in Figure 2.34. Among them, the maximum accuracy is obtained through the Kozeny-Carman equation.

The flow in porous media is idealized using the two-phase model and a void ratio and particle size dependent Kozeny-Carman equation. During deformation, together with the void ratio values, the permeability of each finite element is also updated after each loading steps and so that not just the overall permeability change, but also local permeability changes are calculated. An element-based solution is used for the local permeability variations.

The Kozeny-Carman implemented a fully coupled model is validated by conducting a laboratory experiment which is detailly explained in the next chapter.

CHAPTER 3

VERIFICATION AND VALIDATION OF NUMERICAL MODEL

In the previous chapter, all the implementations and numerical approximations that are used for the investigation of the cyclic and dynamic behavior of the saturated sandy soils are described:

- A fully coupled two-phase model is implemented into the finite element framework for the investigation of the pore pressure accumulations and corresponding effects on dynamic soil behavior.
- The stress-strain relationship of the soil is described using a constitutive model called hypoplasticity.
- Finally, porosity-permeability relationship is implemented for a more realistic representation of the flow characteristics within the porous media.

In this chapter, all these steps are verified and validated using experimental test results or comparing with analytical solutions.

3.1. Verification and Validation of the Two-Phase Model

In this part, the implementation of the previously described two-phase model is verified using an analytical solution proposed by (Booker 1974). Booker's coupled analytical solution shows a satisfactory agreement with the experimental results available in the literature (Meroi and Schrefler 1995; Gambolati et al. 1984) so that verification procedure can also be considered as a validation of the model.

The complex nonlinear behavior of fully saturated soil can be divided into two rather less complex components: one the nonlinearity within the solid phase itself due to the rearrangements of particles and the other one is due to the solid-fluid interaction during the pore volume change. These two are highly connected to each other (coupled problem) and they are difficult to be solved together. One simplistic approach is to model these two behaviors independently from each other and then couple them to

form a realistic soil behavior, an inductive approach. For example, remember the Terzaghi's and Biot's poroelasticity theory where the soil is idealized with a poroelastic model, so that they could investigate the nonlinear behavior arises from the time dependent dissipation of fluid.

Similar to Biot and Terzaghi, in the Booker's 3D consolidation problem, the soil medium is idealized with a linear elastic material model and then time dependent consolidation of a fully saturated soil layer subjected to a static surcharge loading was investigated using two-phase u20p8 element. The geometry of the problem and its finite element implementation with corresponding boundary conditions are given in Figure 3.1 and Figure 3.2, respectively.
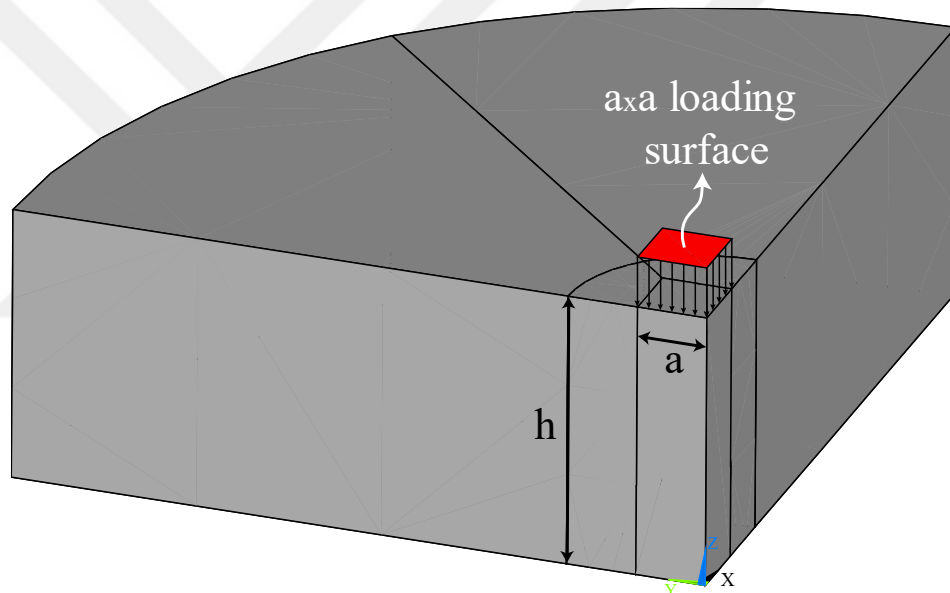

Figure 3.1. Model geometry and description

In Booker's article, the problem is solved both for the rough and smooth base boundary conditions. In the rough case, the nodes at $z = 0$ m are clamped in all directions (fixed support). In this thesis, comparisons are also performed using rough base boundary conditions. All the boundaries are set to be impermeable except the ground surface. Note that, the loading surface area is also permeable.
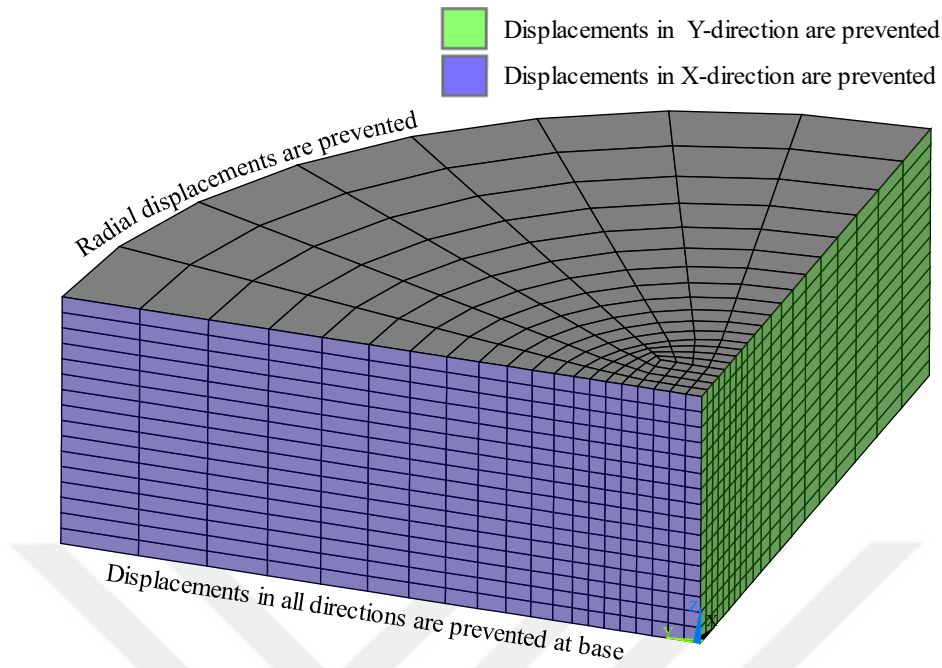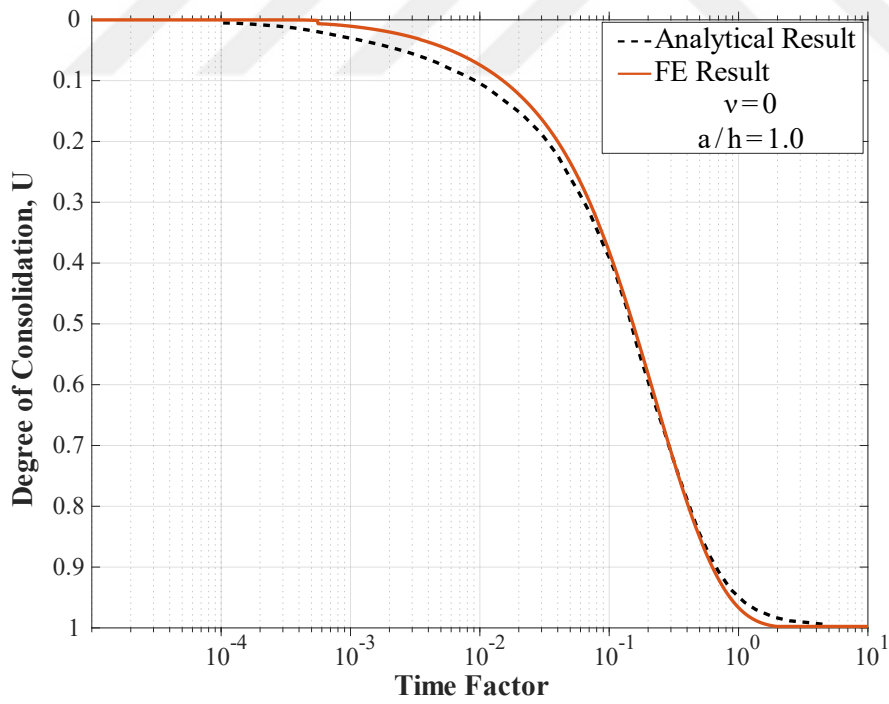
Figure 3.2. Finite element model with boundary conditions

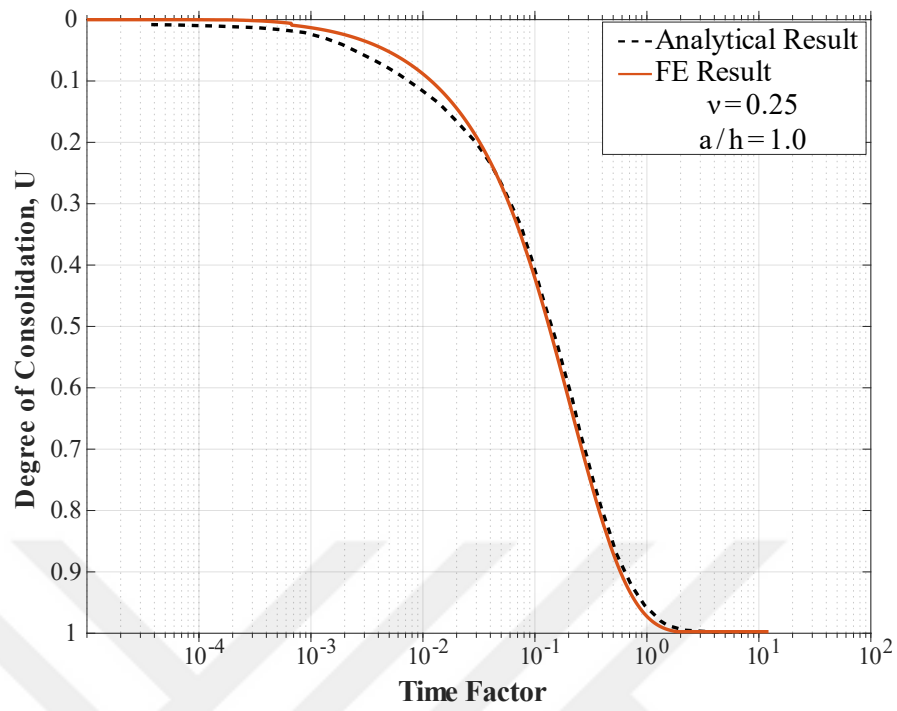*Figure 3.3.* Comparison of degree of consolidation for a finite layer

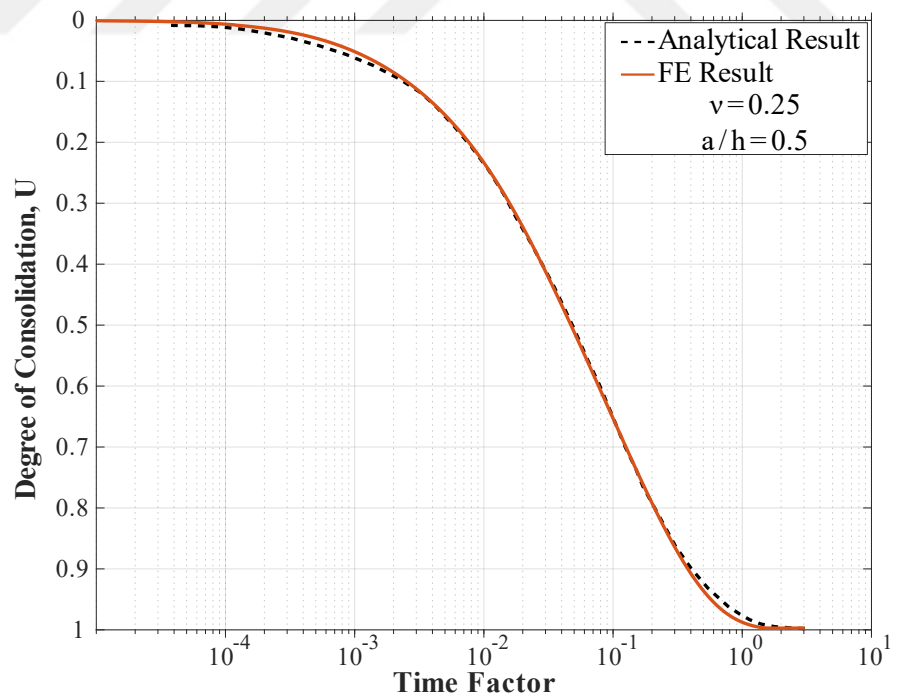*Figure 3.4.* Comparison of degree of consolidation for a finite layer

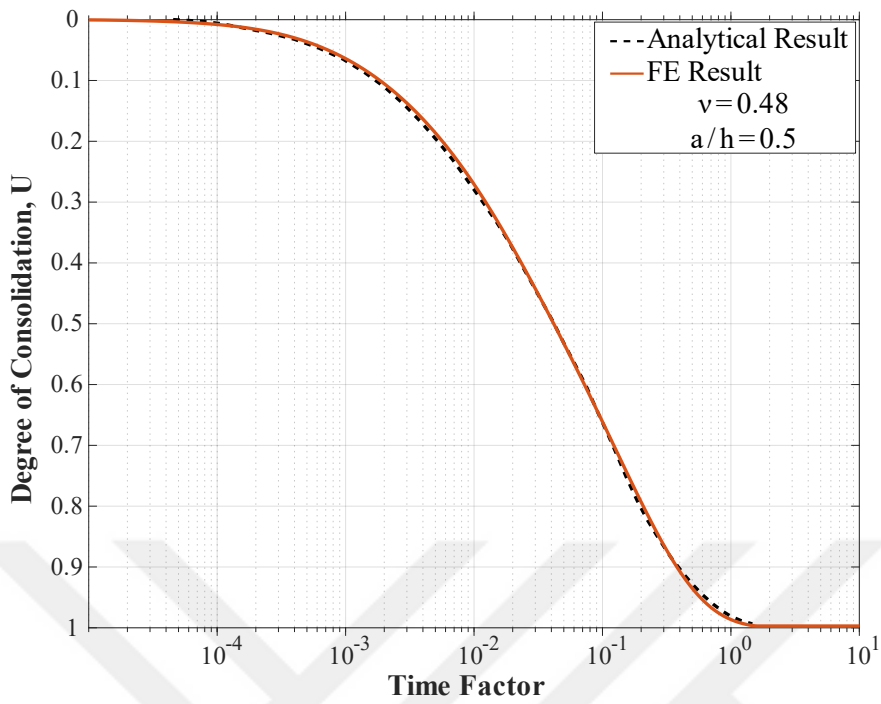*Figure 3.5.* Comparison of degree of consolidation for a finite layer

69

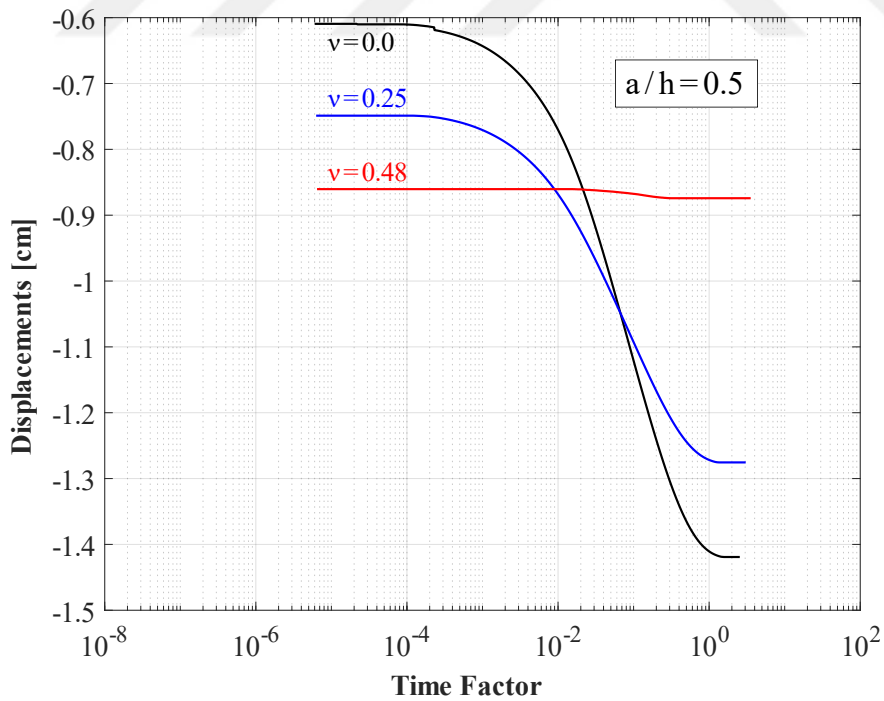*Figure 3.6.* Comparison of degree of consolidation for a finite layer

Figure 3.7. Displacement comparisons for different Poisson's ratio values

70

The finite element results and Booker's analytical solutions which are compared for different a/h and Poisson's ratios in Figure 3.3, 3.4, 3.5 and 3.6 are in perfect agreement. The finite element results given in Figure 3.7 are also coherent. As the Poisson's ratio approaches to $\nu \rightarrow 0.5$ model behaves undrained. Even though the model is permeable due to the high Poisson's ratio, not much settlements are observed for $\nu = 0.48$. The material parameters used in the finite element analyses are listed in the Table 3.1.

In all these comparisons, the width of the loading surface is selected as $a = 4$ m and the depth of the soil layer changed according to the given a/h ratio. Considering the elastic soil behavior, degree of consolidation and time factor are formulated as follows,

$$U = \frac{u_z - u_{z0}}{u_{z\infty} - u_{z0}} \tag{3.1}$$

u_{z0} and $u_{z\infty}$ are displacements at the ground surface under the loading surface at $t = 0$ and $t \rightarrow \infty$, respectively.

$$\text{Time factor, } T_v = \frac{c^* \cdot t}{h^2} \tag{3.2}$$

Note that c^* is an adjusted consolidation coefficient which uses Young's modulus of the soil,

$$c^* = \frac{k \cdot E}{\gamma_w} \frac{(1 - \nu)}{(1 - 2\nu) \cdot (1 + \nu)}$$

Table 3.1. *Material parameters used in FE analysis and analytical solutions*

Description	Symbol	Value
Young's Modulus	E	4×10^4 kN/m^3
Poisson's Ratio	ν	0.0, 0.25, 0.48
Hydraulic Conductivity	k	2×10^{-6} m/s
Unit weight of water	γ_w	9.81 kN/m^3

Dissipation of the water is illustrated by using the contour plots given in Figure 3.8, 3.9 and 3.10 obtained directly from the finite element analyses. At t ≈ 0 sec., the applied surface load is resisted by an increase in pore pressure and then together with the dissipation loads are transferred to the solid skeleton. Figures below prove that the coupled behavior is simulated successfully.
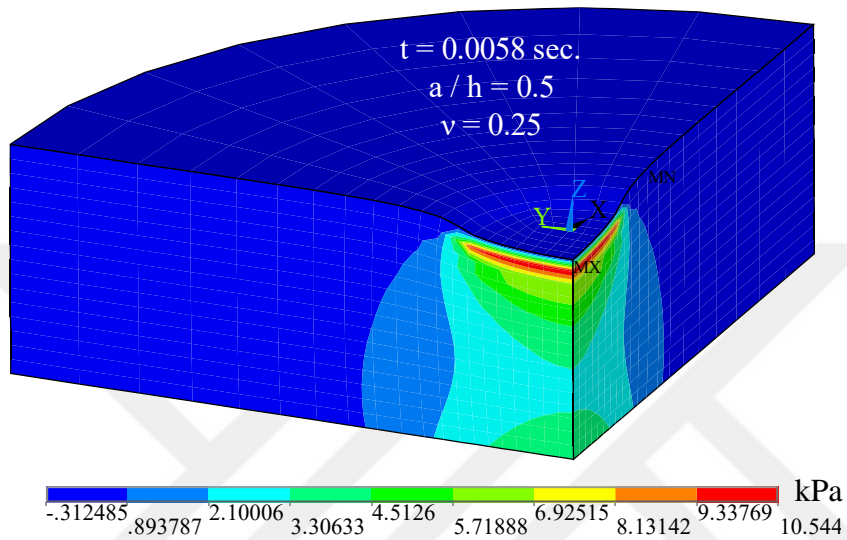

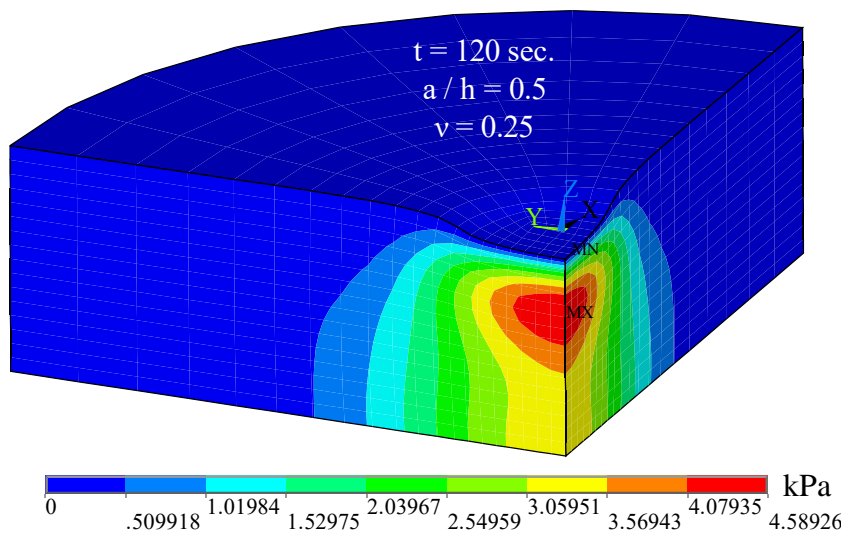*Figure 3.8.* Pore pressure contour plots at t ≈ 0 sec.

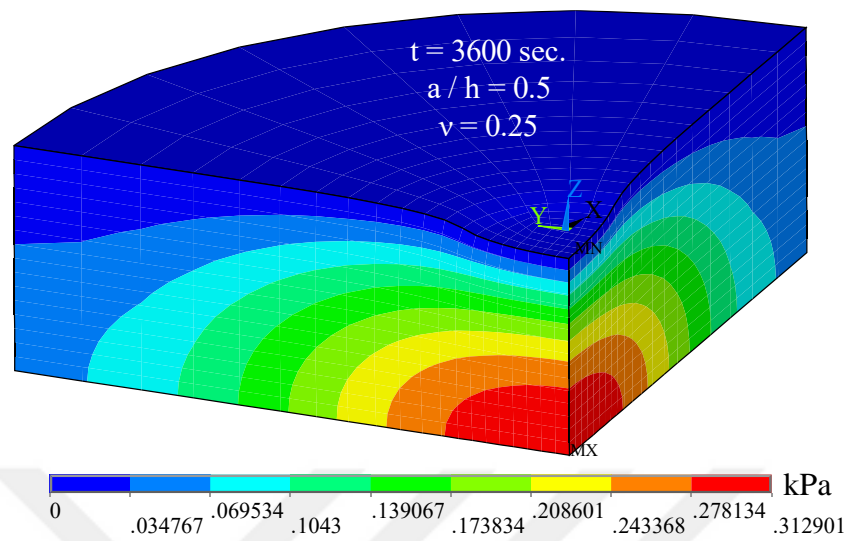*Figure 3.9.* Pore pressure contour plots at t = 15 sec.

Figure 3.10. Pore pressure contour plots at t = 3600 sec.

3.2. Verification and Validation of the Coupled Numerical Model

In this thesis, the extended hypoplasticity developed by (Niemunis and Herle 1997) has been used and all the simulations are performed using the ANSYS. The implementation of the model in ANSYS is already verified by (Taşan H. E. 2011). Here also the verification procedure is repeated using an undrained cyclic triaxial simulation. Note that, it is important to have a validated two-phase model before conducting an undrained simulation where the excess pore pressure developments expected to occur.

Since the two-phase model is already validated in the previous part, now using coupled analysis (both hypoplasticity and two-phase model together) an undrained cyclic triaxial test is simulated and then compared with the simulation result provided by Niemunis & Herle (1997), results show satisfactory agreement as shown in the Figure 3.11.

In this simulation, first, the specimen is consolidated under 300 kPa cell pressure and then cyclic deviatoric stress with an amplitude of 30 kPa is applied for shearing. The hypoplastic material parameters of the Hochstetten sand used in this simulation are available in (Niemunis and Herle 1997).
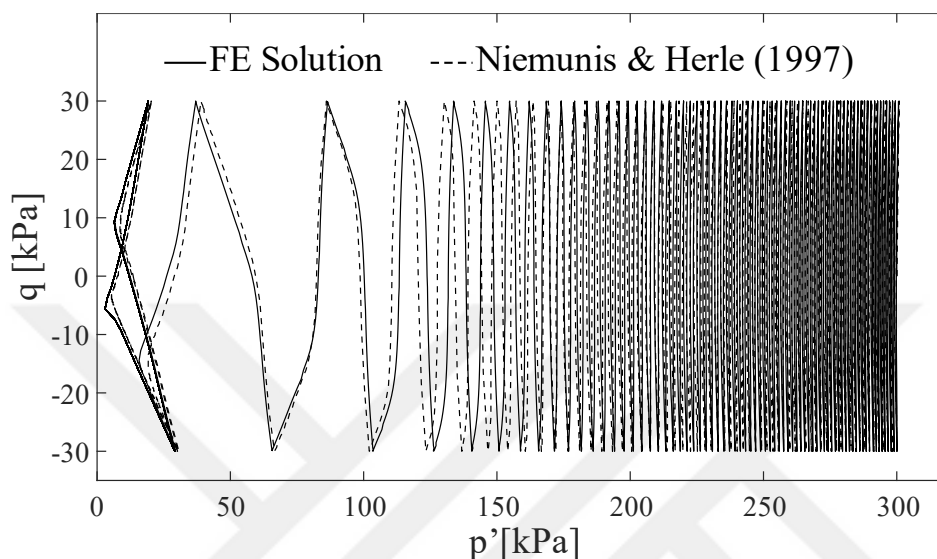

Figure 3.11. Numerical comparison of an undrained cyclic triaxial test

Since the implementation of the model in ANSYS is verified, now we can validate it using experimental test data.

3.2.1. Numerical Simulation of Cyclic Element Tests

In this part, a consolidated undrained cyclic triaxial tests and a constant volume cyclic shear test are simulated, and then numerical results are compared with the experimental data.

The first test was performed by (Wichtmann 2016). This test is labeled as test TCUI7 in the book. Karlsruhe sand with an initial relative density, $I_{D0} = 0.67$ was used in the experiment. The hypoplastic material parameters of the sand which is adopted from (Stutz 2016) are presented in Table 3.2.

Table 3.2. *Hypoplastic material parameters for Karlsruhe Sand, Sturm (2009)*

φ_c	h_s[MPa]	n	e_{d0}	e_{c0}	e_{i0}	α	β
32.8°	625	0.33	0.67	1.05	1.21	0.18	1.12

R	m_R	m_T	β_R	χ
10^{-4}	6.0	3.5	0.2	6.0

The specimen was first isotropically consolidated under 200 kPa cell pressure and then sheared with a 60 kPa amplitude cyclic deviatoric stress.
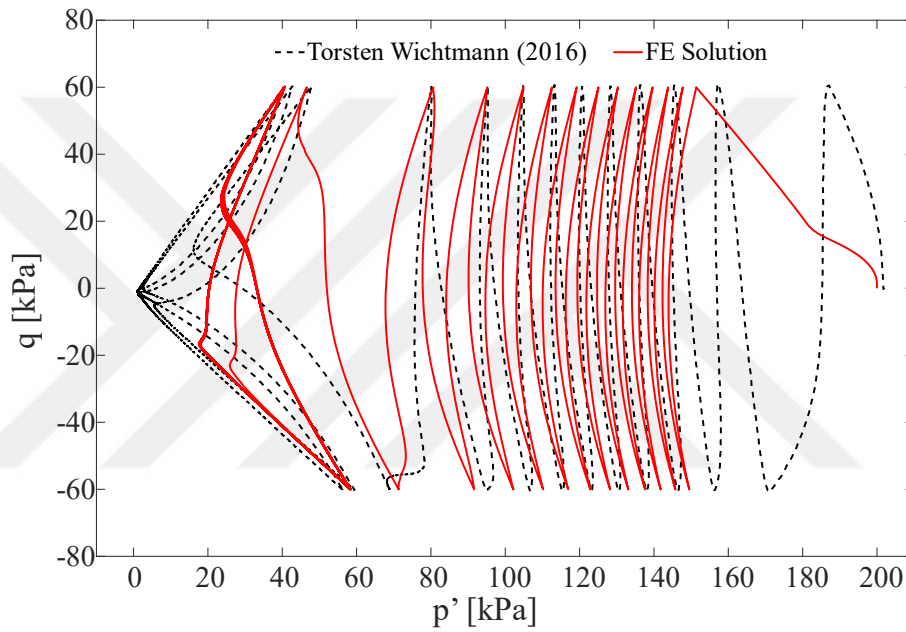

Figure 3.12. Experimental and simulation results of the undrained cyclic triaxial test

Second, an undrained cyclic simple shear test reported in (C-CORE 2004) is simulated. The Fraser River sand with an initial relative density, $I_{D0} = 0.44$ was used in the experiment. The specimen was first consolidated under 200 kPa normal stress and then sheared with a cyclic stress ratio of CSR = 0.08 as described in Figure 3.13. Note that, for a cyclic simple shear test, the cyclic stress ratio, CSR is defined as,

$$\text{CSR} = \frac{\tau_{cyc}}{\sigma'_{vc,0}} \tag{3.3}$$

τ_{cyc} : cyclic shear stress and σ'_{vc} : vertical effective stress
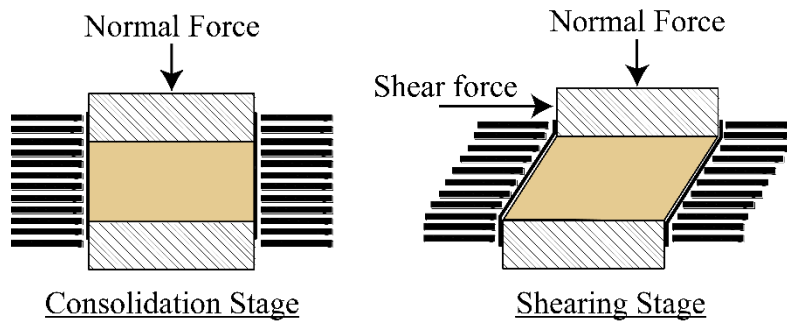
Figure 3.13. Schematic of simple shear test with stack rings

A single u20p8 finite element given in Figure 3.14 was used to simulate the cyclic simple shear test. The bottom nodes (no. 1,2,3,4,9,10,11 and 12) were fixed in all three directions. The nodes located in the middle of the element (no. 17,18,19 and 20) were modeled such that during shearing they will share the displacement equally. To do that, in ANSYS using the CP command an additional a set of coupled degree of freedom was defined for the selected nodes. The same procedure was also followed for the nodes located at the top (no. 5,6,7,8,13,14,15 and 16). During the consolidation stage, the pore pressure degree of freedoms were set free for all 8 nodes and during shearing set free option was removed so that the pore pressures started to accumulate. The boundary conditions of the element and loading configuration are illustrated in Figure 3.14.
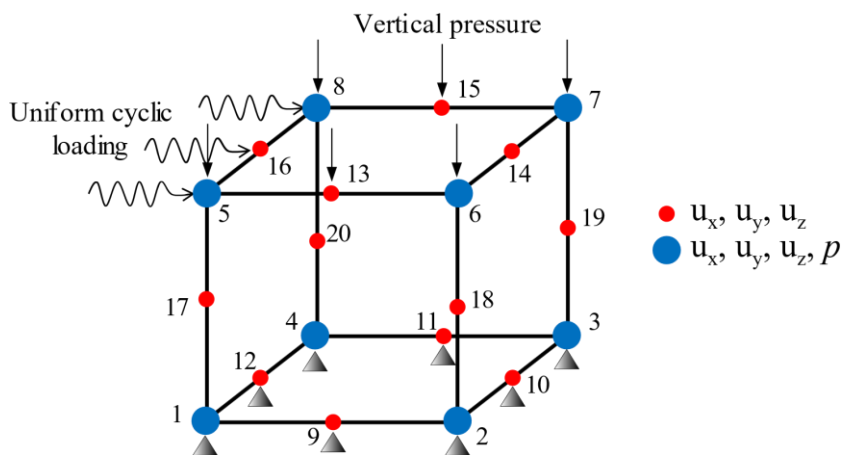

Figure 3.14. cyclic simple shear boundary conditions koy

The hypoplastic material parameters of the Fraser River sand were taken from (Holloer 2006) is given in the Table

Table 3.3. *Hypoplastic material parameters for FraserRiver Sand, Holler (2006)*

φ_c	h_s[MPa]	n	e_{d0}	e_{c0}	e_{i0}	α	β
35.0°	1600	0.39	0.62	0.94	1.08	0.20	1.0

R	m_R	m_T	β_R	χ
10^{-4}	2.5	9.0	0.25	9.0

According to (Idriss and Boulanger 2008) excess pore water ratio r_u for a cyclic simple shear test is defined as,

$$r_u = \frac{\Delta p}{\sigma'_{vc,0}} \tag{3.4}$$

using this ratio, initiation of the liquefaction (or partial liquefaction) for $r_u \cong 1.0$ is investigated in Figure 3.16. The response of the Fraser River sand to undrained cyclic shear test is given in Figures 3.15 and 3.16.
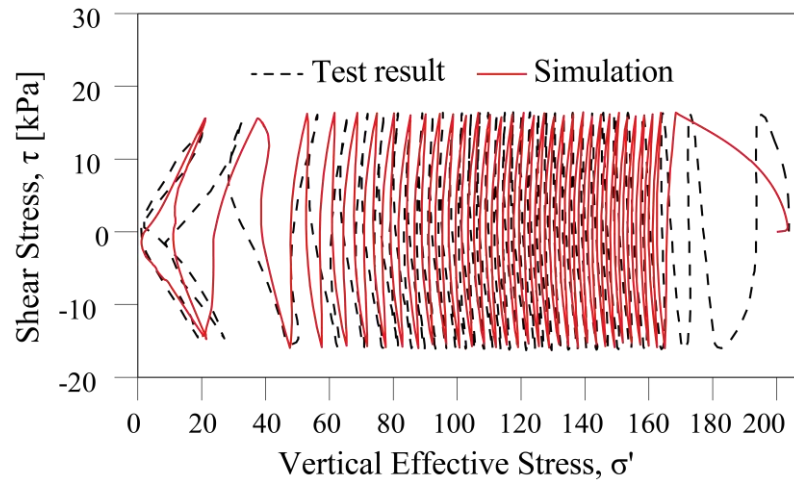

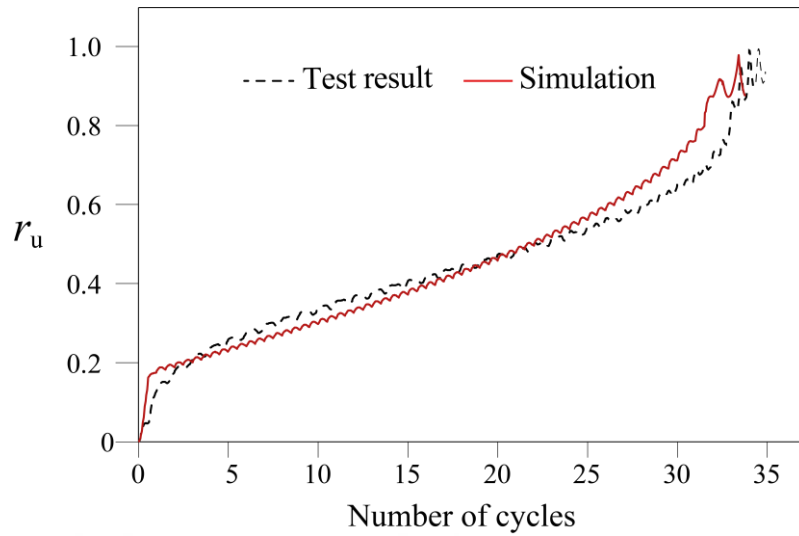*Figure 3.15.* cyclic simple shear simulation result koy

Figure 3.16. Excess pore pressure developments with increasing cycle numbers

Note that, these undrained simulations are conducted using hypoplastic constitutive model with u20p8 finite element. Referring to the formulation of the hypoplasticitiy, the failure surface and plastic potential which are emerged as by-products of the model show that the vector of plastic strain rate is not normal to the yield surface which corresponds to non-associative flow rule. The non-associative flow rule helps us to produce the volumetric contraction or dilation response induced by shear loading. Since the material is simulated with the fully coupled two-phase finite element, the contractive or dilative response produces pore water pressure changes, simulating the undrained response.

All three experiments help us to validate the coupled numerical model for the dynamic and cyclic problems.

3.2.2. Numerical Simulation of a Laboratory Experiment

The experiments in the previous part were simulated for undrained conditions. During shearing, under cyclic loading conditions, there was no in or out flow. Although these experiments show us the capability of the coupled model to accurately predict the cyclic behavior of soil; they are not suitable for the investigation of the porosity-

permeability implementation. In order to validate the porosity-permeability relationship, an experimental setup was prepared.

In this part, before discussing the result of the experiment, first, the characteristics of the sand used in the experiment and then the test setup itself will be described.

3.2.2.1. Characterization of Sand

A large amount of well-graded sand was prepared for the experiment. The particle size distribution of the soil determined by following the ASTM-D6913 is given in Figure 3.17. According to the USCS, soil is classified as well graded sand (SW).
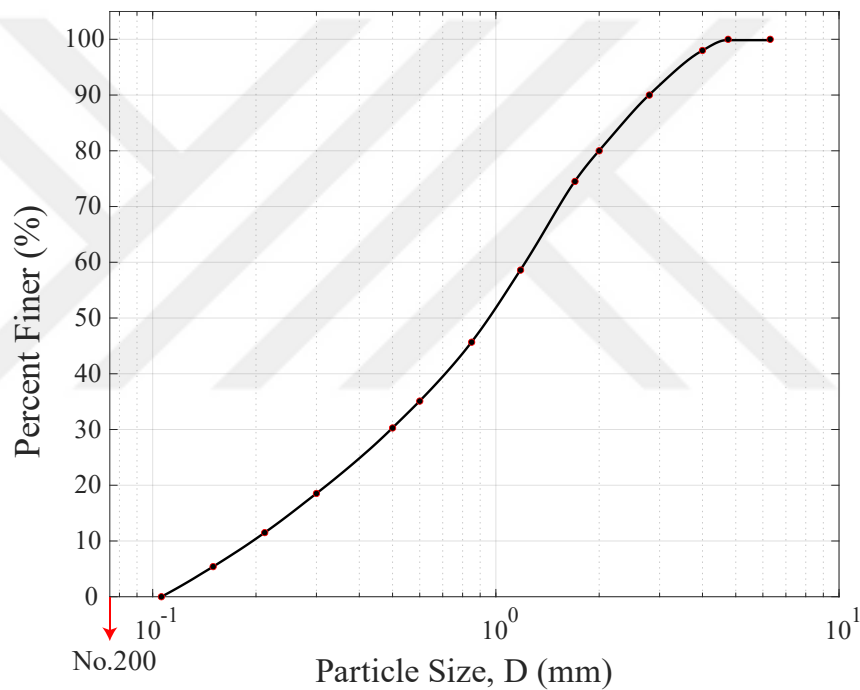

Figure 3.17. Particle size distribution of the sand

The specific gravity of the sand was determined using the ASTM-D854 standard. The test results are listed in Table 3.4.

Table 3.4. *Specific gravity of the sand*

	Test-1	Test-2	Test-3	Test-3	**Ave.**	StdV
ρ_d [g/cm³]	2.681	2.683	2.679	2.683	**2.682**	0.002

The critical friction angle of the sand is determined using the previously described image processing method. Three different angle of repose test has been conducted and as a result, φ_c (or φ_{rep}) is determined as $33.45°$ with a standard deviation of $0.01°$, Figure 3.18.
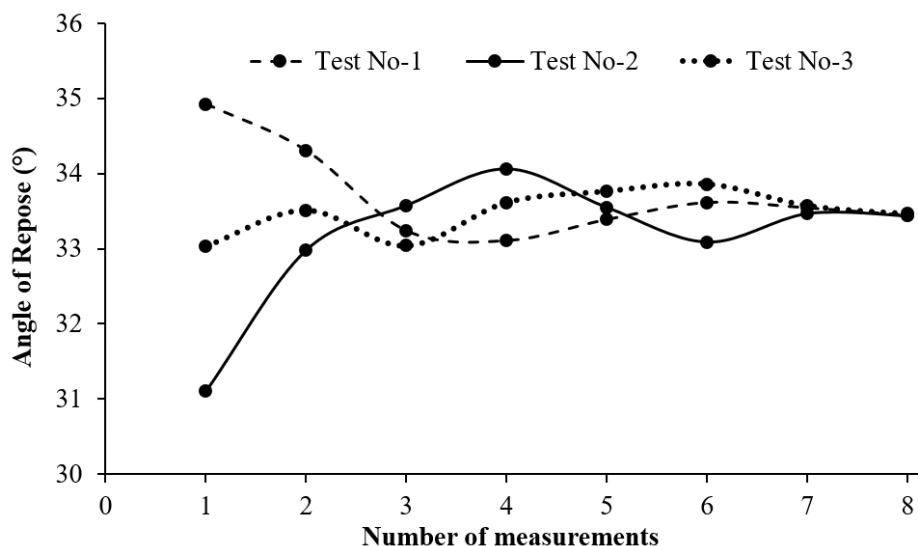

Figure 3.18. Determination of the critical friction of the sand using image processing

Minimum and maximum void ratios are determined according to the JGS 0161. The details of the test procedures are described in (Anaraki 2008). The test results are listed in Table 3.5 and 3.6.

Table 3.5. *Maximum void ratio of the sand with JGS 0161*

	Test-1	Test-2	Test-3	Test-4	Test-5	Test-6	**Ave**.	StdV
Void Ratio	0.930	0.907	0.915	0.923	0.926	0.908	**0.918**	0.009

Table 3.6. *Minimum void ratio of sand with JGS 0161*

	Test-1	Test-2	Test-3	Test-4	**Ave.**	StdV
Void Ratio	0.648	0.617	0.632	0.617	**0.629**	0.0149

In order to determine the stiffness parameters h_s, n of the sand a series of oedometer tests are performed. Among them, the one with maximum initial void ratio has been

80

selected for the calculation of h_s and n parameters. After determination of these parameters, the oedometer test was simulated and a perfect agreement was obtained as shown in Figure 3.19.
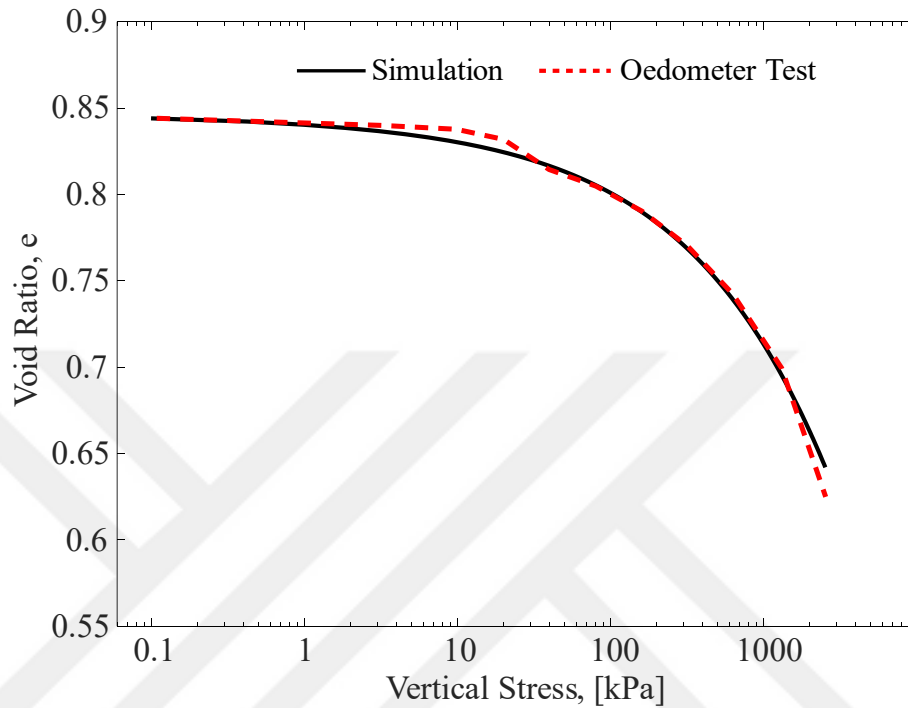

Figure 3.19. Comparison of oedometric response of the sand

For the determination of the exponent α, a triaxial test with a dense specimen has been conducted and it is determined as 0.25. Since loose sand was used for the test, the parameter β is assumed to be equal to 1.0 according to the recommendation of (Herle and Gudehus 1999). Finally, for the determination of the intergranular strains parametric calibration procedure suggested by (Masin, 2019) was followed.

The hydraulic properties of the sand at different void ratios were determined by performing a set of constant head permeability tests according to the ASTM-2434, Figure 3.20. Test results are provided in Table 3.7, Test-1 and Test-3 correspond to loosest and densest states, respectively.

81

Figure 3.20. Determination of hydraulic conductivity of sand using constant head test

Table 3.7. *Hydraulic conductivity values of the sand*

m/sec.	Test-1	Test-2	Test-3
Constant Head	$7.78E10^{-4}$	$5.12E10^{-4}$	$2.90E10^{-4}$
Kozeny-Carman	$7.65E10^{-4}$	$5.09E10^{-4}$	$3.41E10^{-4}$

The constant head permeability test results were also compared with the predicted values obtained from Kozeny-Carman relationship using Equation 2.90. Note that, particle size distribution is given in Figure 3.17. has been used for the calculation of the Kozeny-Carman predictions.

3.2.2.2. Experimental Setup

A column shape container with 18.7 cm $\times$ 18.7 cm internal cross section and 75.0 cm internal height was designed for the experiment, Figure 3.21. Inside of the container was covered with the plexiglass in order both to increase the visibility of the soil specimen during the test and decrease the total mass of the container.
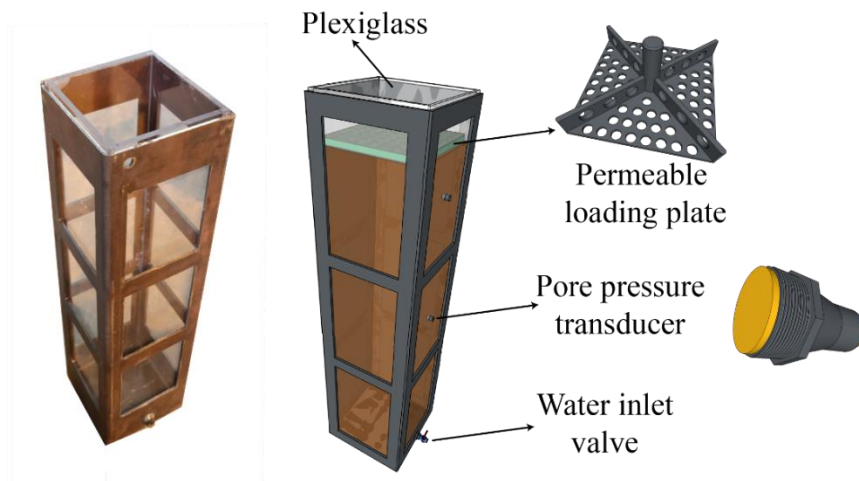
Figure 3.21. Real (left) and designed (right) container and detailed information

In order to measure the pore pressure developments, three pore pressure transducers have been located at bottom, top and middle of the specimen. Unfortunately, even though the pore pressure development trend was captured, no useful data could be obtained. The most possible reason is that the direction of the flow was parallel to the surface of the transducers, Figure 3.22, which prevented accurate pore pressure measurements.
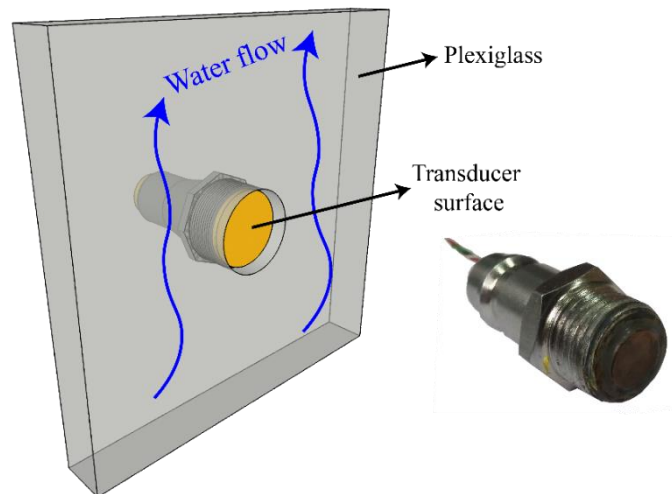

Figure 3.22. Pore pressure transducer

In order to make sure that a fully saturated soil sample is prepared, first water was added though the inlet valve located at the bottom of the container and then soil sample

was poured into the water. This procedure was repeated for every 2 cm heights. At the end of the procedure, the height of the specimen was 67.3 cm. Note that, in order to prevent the segregation of particles, the drop height kept almost zero during the procedure.

A fully automated MTS 250 kN high rate test machine was used for the application of the cyclic loading in Materials of Construction Laboratory, METU, Figure 3.23.
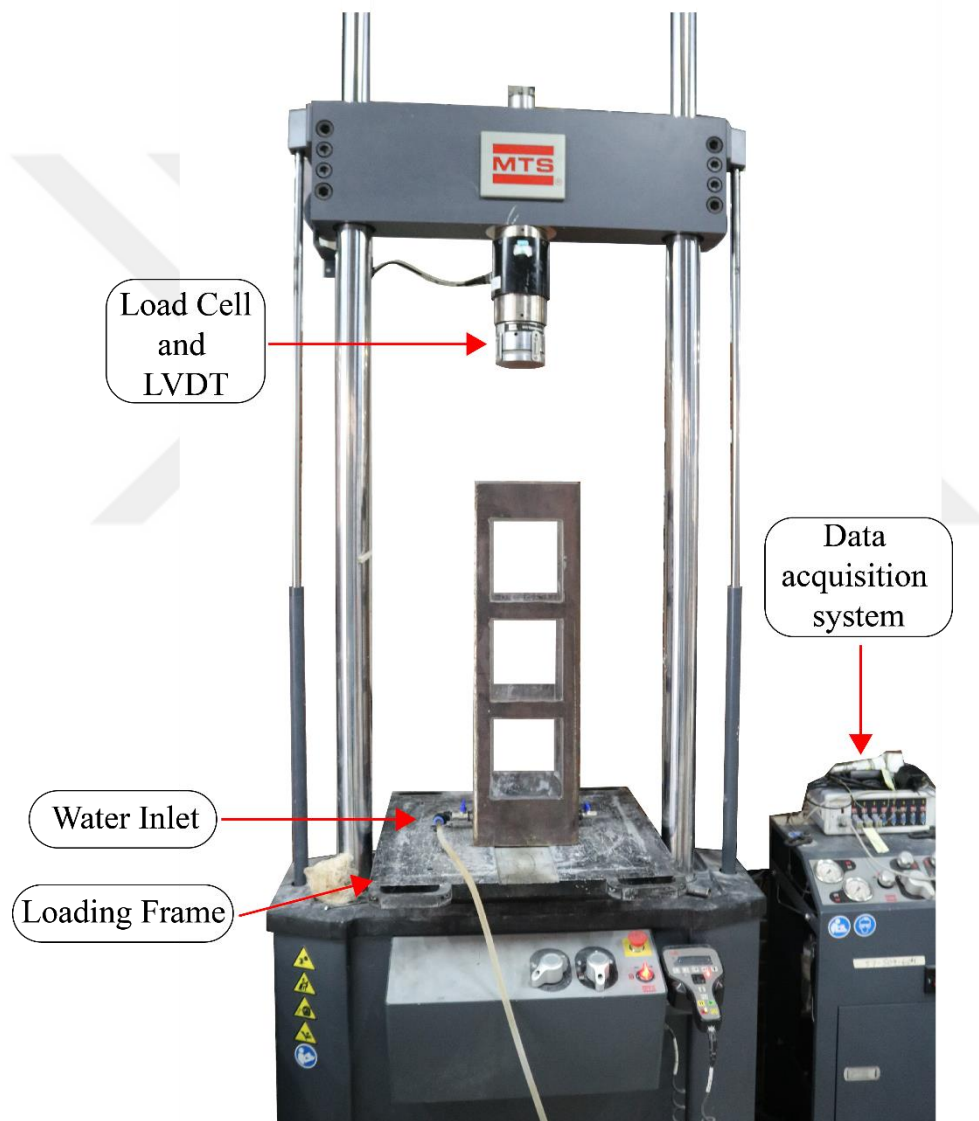

Figure 3.23. MTS high rate test system

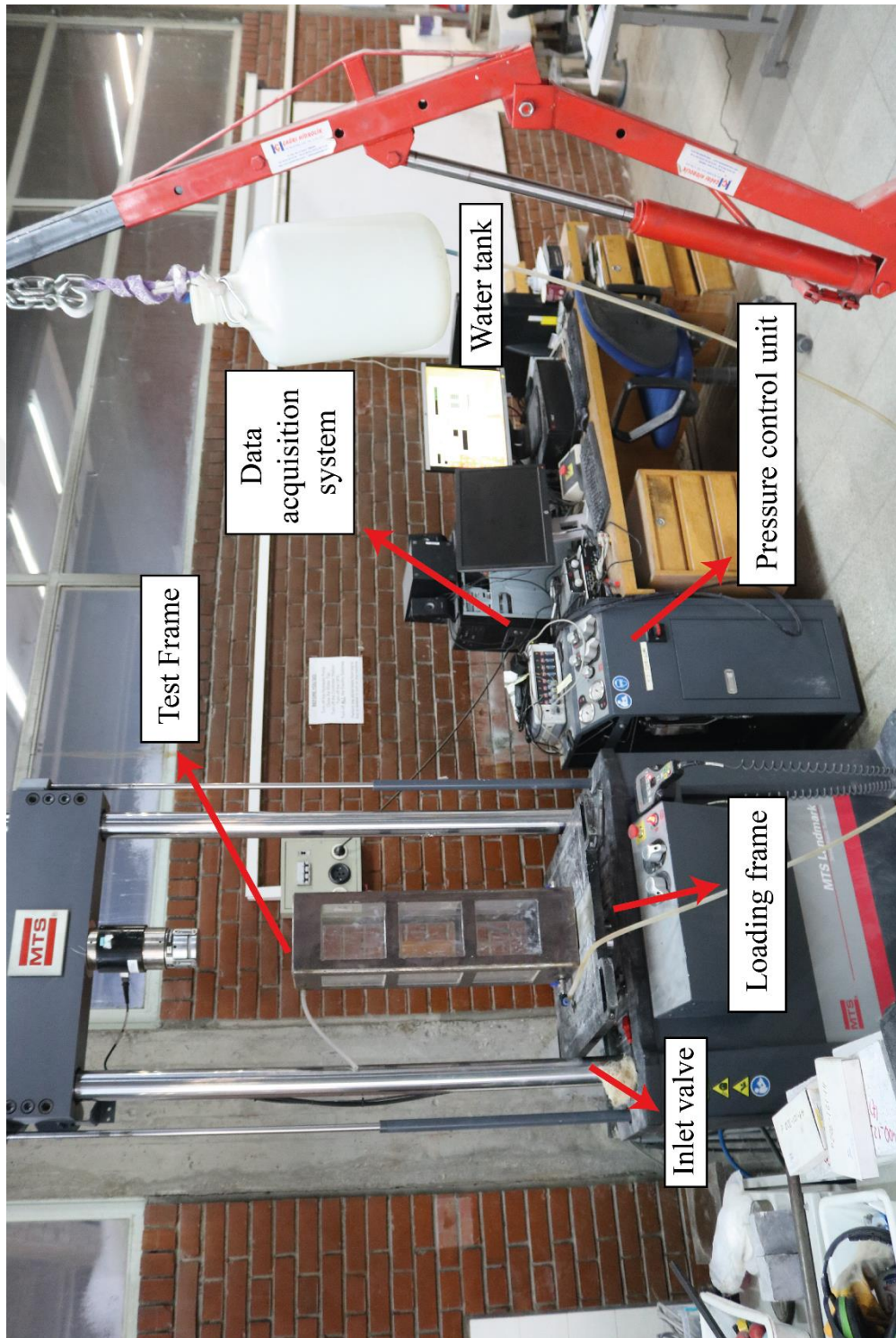Finally, an overall view of the setup is presented in the Figure 3.24.

Figure 3.24. Overall representation of the experimental test setup

3.2.2.3. Numerical and Experimental Results

In order to validate the numerical model under the drained condition above described experimental setup was prepared. After the preparation of the fully saturated sandy soil with a relative density of $I_D = 0.43$, the vertical stress given in Figure 3.25 is applied to the specimen.
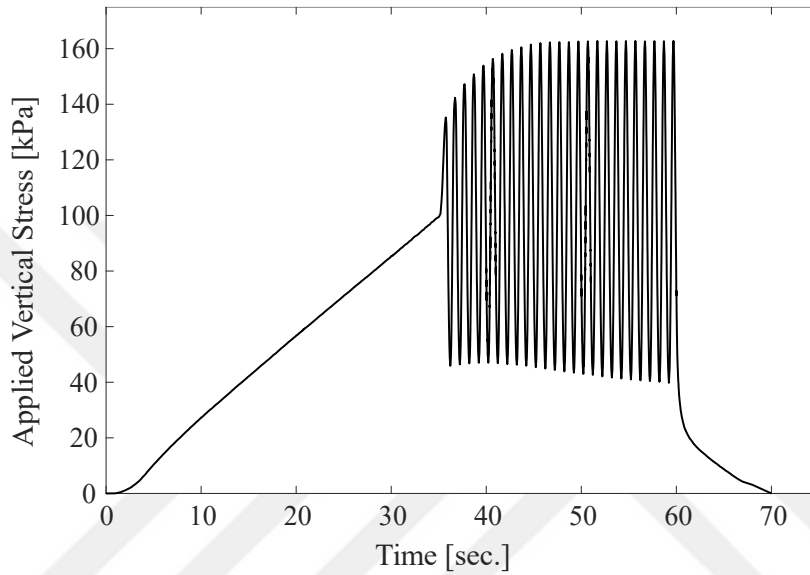
Figure 3.25. Time vs. Applied cyclic load

The hypoplastic material parameters of the sand which was obtained through following the parameter determination steps are given in the Table 3.8.

Table 3.8. *Hypoplastic parameters of the sand used in the experiment*

φ_c	h_s[kPa]	n	e_{d0}	e_{c0}	e_{i0}	α	β
33.631°	43418	0.571	0.629	0.918	1.056	0.25	1.0

R	m_R	m_T	β_R	χ
2.4×10^{-4}	5.0	2.0	0.5	5.0

The Kozeny-Carman constant which is determined from Equation 2.90 and Table 3.7 is equal to 0.001897.

During the numerical modeling of the experiments, there are some important issues needs to be considered. Due to the limitation of the MTS machine, the vertical load is

86

actually not directly applied to the specimen, but specimen (the whole frame) moved so that the loading pattern given in Figure 3.25 is formed, the position of loading frame is given in Figure 3.24. Since the specimen itself moving throughout the experiment, within the numerical analysis inertia forces were also taken into account using mass matrices.
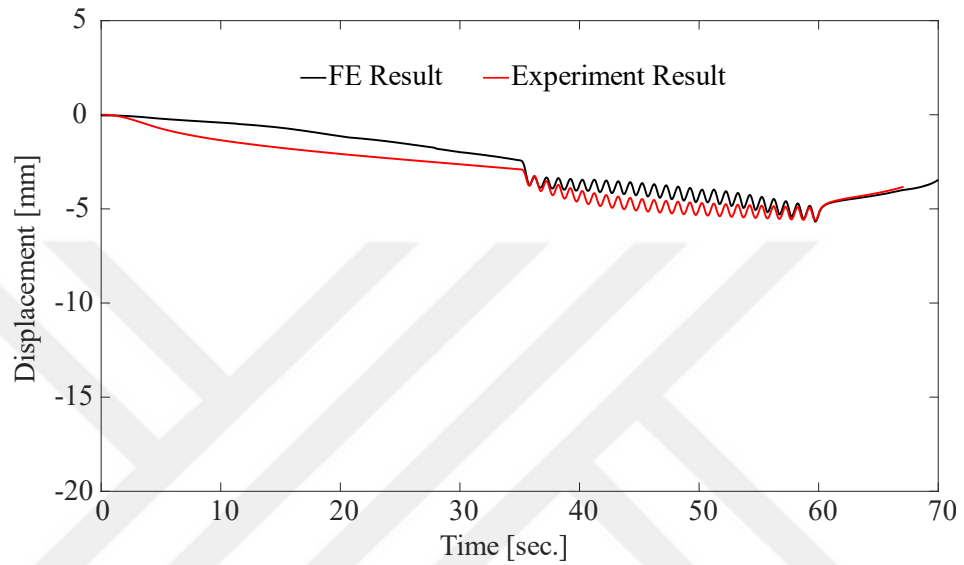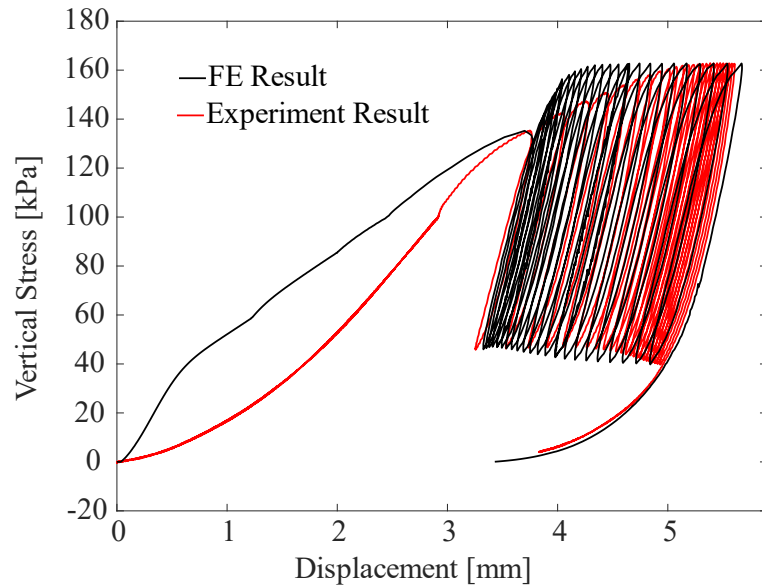

Figure 3.26. Displacement vs. time

Figure 3.27. Displacement vs. vertical stress

Although the loading condition was not ideal, still a satisfactory results have been obtained through numerical modeling as shown in Figure 3.26 and 3.27.

CHAPTER 4

CASE STUDIES

Cyclic behavior of soil is highly complex and depends on many factors such as void ratio, drainage conditions, degree of saturation, loading characteristics et cetera. In the previous chapters, how the drainage mechanisms can influence the cyclic behavior of the soil tried to be explained. In this chapter, real size geotechnical problems will be simulated, and for the various loading conditions, the effects of the porosity-permeability relationship on the mechanical behavior of the soil will be investigated.

4.1. Soil-Column Model

In order to investigate the effects of the porosity-permeability variation on the cyclic behavior of the sand, a set of simulations similar to the one performed experimentally in the previous has been conducted on a soil column model given in Figure 4.1. In these numerical simulations, Hochstetten sand was used with the parameters provided in Table 4.1.

Table 4.1. *Hochstetten sand hypoplastic material parameters, Niemunis & Herle (1997)*

φ_c	h_s[MPa]	n	e_{d0}	e_{c0}	e_{i0}	α	β
33.0°	1000	0.25	0.55	0.95	1.05	0.25	1.0

R	m_R	m_T	β_R	χ
1.0×10^{-4}	5.0	2.0	0.5	6.0

The boundary conditions were created such that the soil exposed to vertical cyclic loading in a rigid box. To do that, the nodes at the bottom of the model were fixed in Z-direction and the nodes located at the four sides of the model were fixed in the direction vertical to the surface they belong to. For example, the nodes located at $X = 0$ are fixed in the X-direction. A free drainage condition was defined at the top surface of the model by setting the pore pressure degree of freedoms of the nodes located at $z = h$ to zero and all the remaining surfaces assumed to be impermeable.
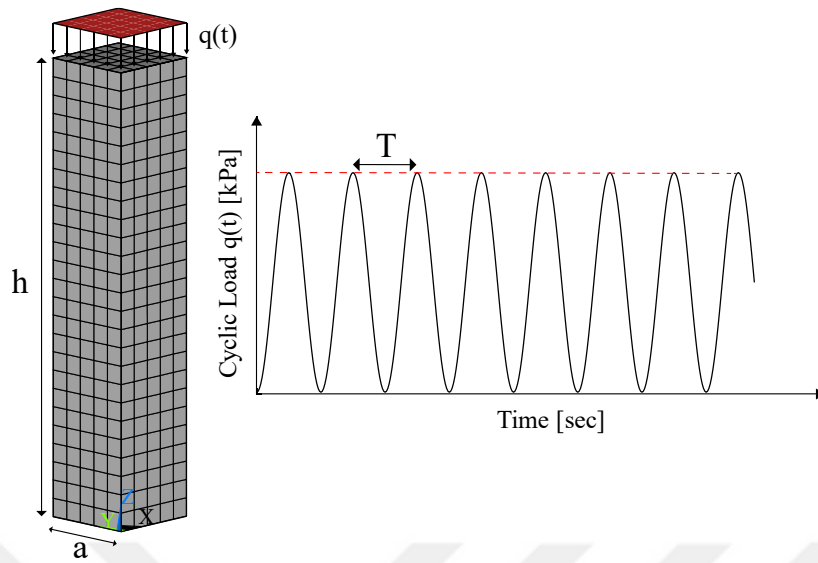
Figure 4.1. Soil column and applied cyclic load

A set of parametric analysis has been conducted to understand how the porosity-permeability variation affects the pore pressure and displacement accumulations. The first numerical simulation was performed for the geometry and the initial conditions listed in Table 4.2.

Table 4.2. *Model geometry and initial conditions*

Model Parameters	Value
a/h	0.2
h	10 m
Relative density, I_D	0.64
Period, T	6 sec.
Amplitude, σ_{amp}	400 kPa
$k_{initial}$	1×10^{-4} m/sec.
C_{KC}	5.05×10^{-4}

Two analyses, one with and another without the porosity-permeability relationship implementation have been performed. The results are provided in Figures 4.2, 4.3 and 4.4. In these figures "with KC" refers to Kozeny-Carman relationship implemented model.
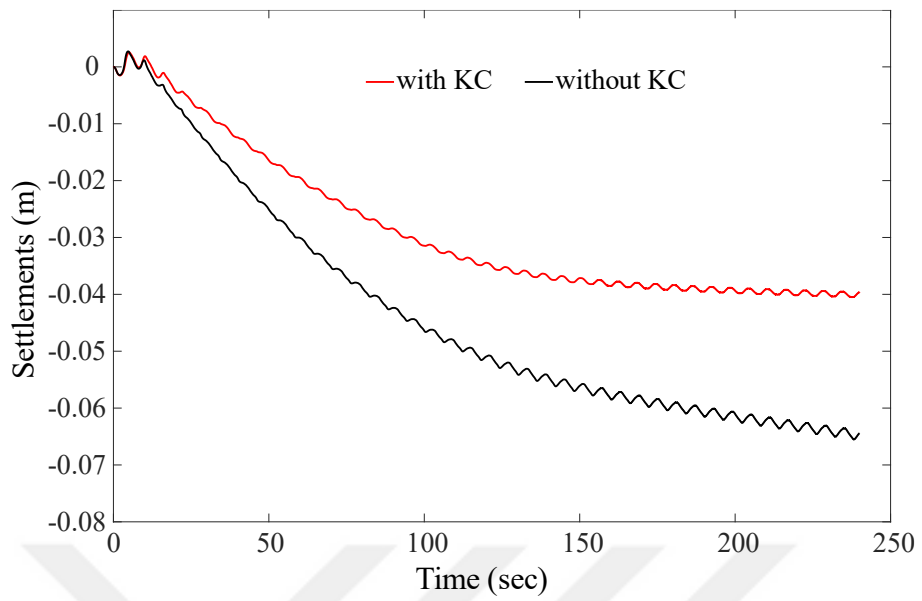
90

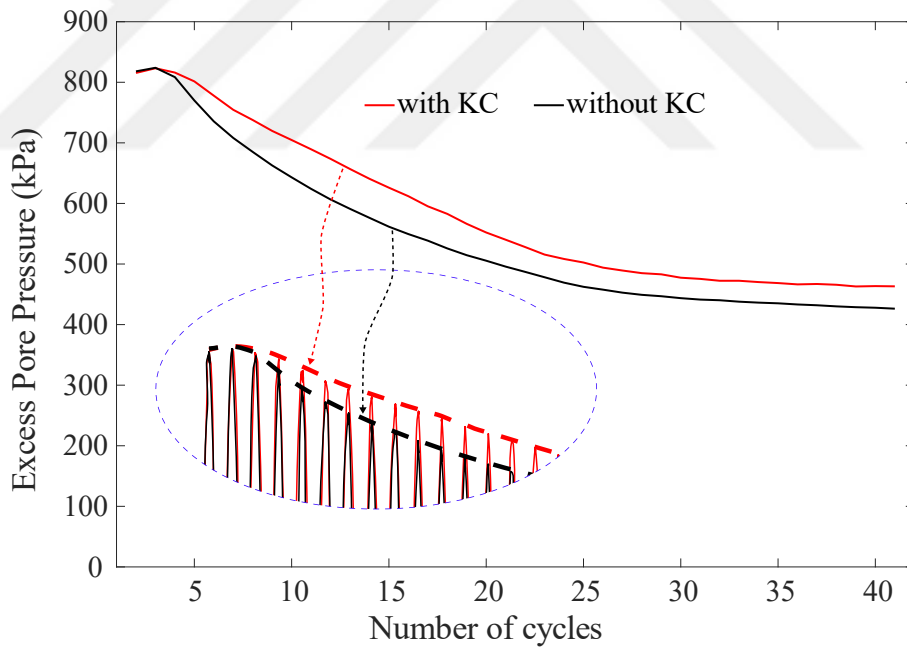*Figure 4.2.* Displacements at the mid-depth of the soil column

Figure 4.3. Excess pore pressure developments at the mid-depth of the soil column
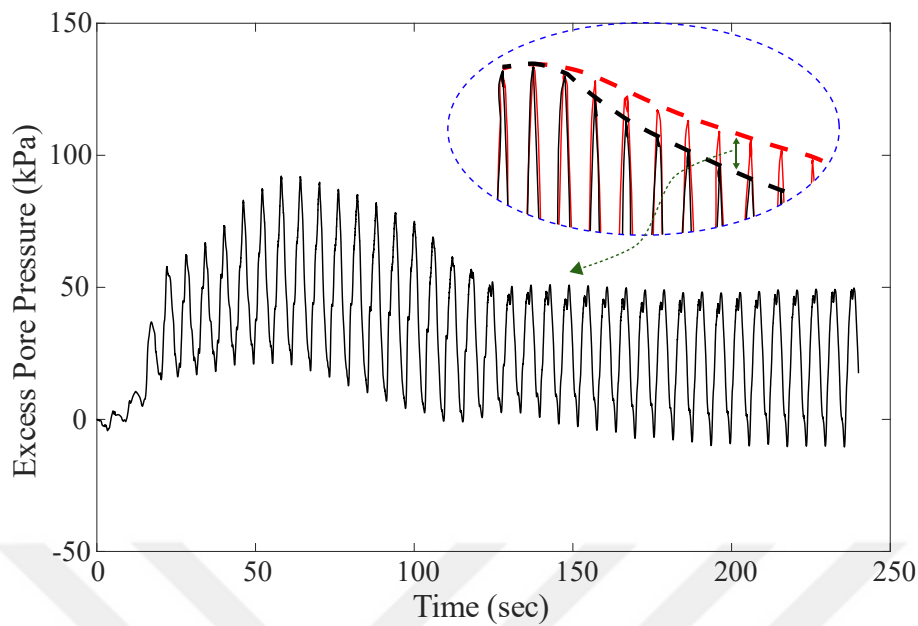
91

Figure 4.4. Excess pore pressure difference between KC and without KC simulations

The maximum value of the excess pore water pressures is reached at the first cycle of the cyclic loading in both analyses. In case of the analysis with KC, the compaction of soil within a loading cycle causes simultaneous reduction in its permeability whereby the drainage condition is affected in an unfavourable manner. Hence the excess pore pressure values of the Kozeny-Carman implemented model are higher than those without that implementation, Figure 4.3.

In Figure 4.4, the excess pore pressure developments of the two analyses are compared. In that figure, the excess pore pressure values of the model without KC implementation is subtracted from the KC implemented model. This difference can be used to compare the dissipation rate of the water during cyclic loading, because higher pressure is maintained as the permeability of the soil decreases.

According to Figure 4.4, in "without KC" case, a relatively fast dissipation occurs and as a result, larger settlements take place, Figures 4.2.

There are many parameters that affect this dynamic highly coupled dissipation procedure. For example, considering the soil-column example described above, the

increase in the ratio a/h decreases the difference between two analyses, however, increase in the frequency or amplitude of the loading increases the gap between two cases. An example simulation is provided below. The same exact model was simulated with a higher frequency and amplitude cyclic loading, T = 2 sec. and $\sigma_{amp} = 1$ MPa, and results are provided in Figures 4.5 and 4.6.
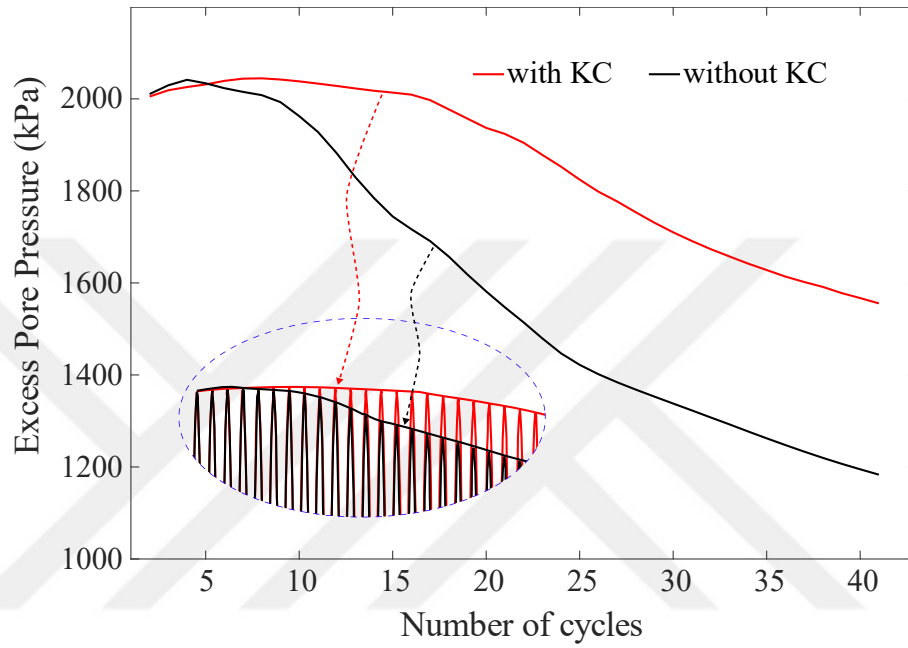

Figure 4.5. Excess pore pressure developments at the mid-depth of the soil column
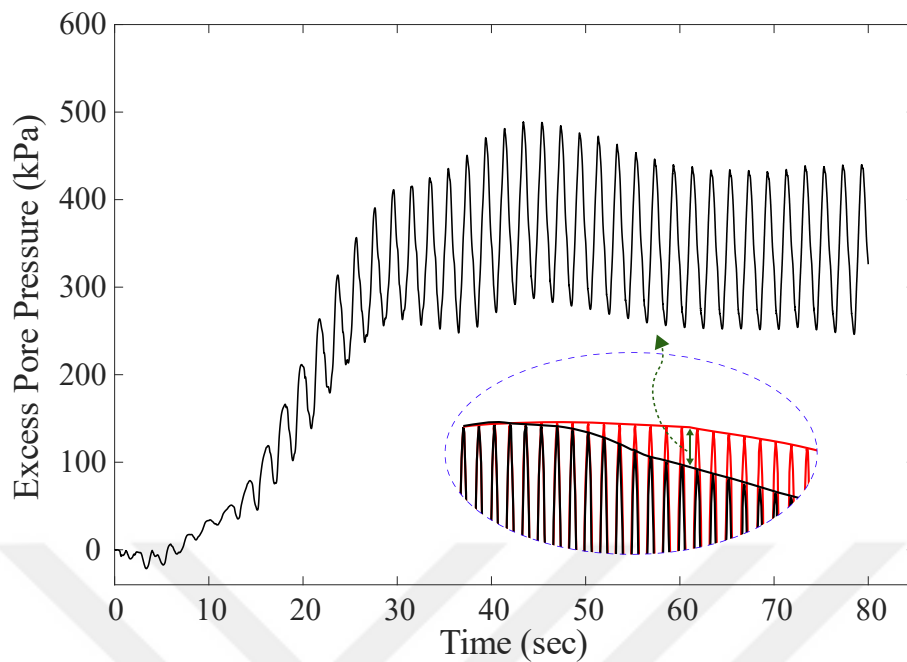
Figure 4.6. Excess pore pressure difference between KC and without KC simulations

Note that, these analyses are performed with the loading path provided in Figure 4.1. The cyclic load started from zero, increased up to its maximum value and then decreased back to zero again. So, what would happen if we monotonically increased the load up to a certain value, let's say a cyclic mean value, and then apply a cyclic loading? The answer to this question is provided in the conclusion part.

In this specific geometry, as expected the maximum deformation occurs at the top of the model where the cyclic load is applied, and it gradually decreases towards to bottom of the model. The relatively high level of deformation close to the upper surface creates a less permeable zone where the water starts to build-up pore pressure.

Comparing both analyses "with KC" and "without KC", a more rapid dissipation takes place in "without KC" case, Figure 4.6 and a higher pore pressure amplitude is maintained in "with KC" case, Figure 4.5.

94

4.2. Numerical Modeling of a Dyke Subjected to Dynamic Loading

The second case study was carried out by the Center for Cold Ocean Resource Engineering (C-CORE) in 2004. A collaborative research project was launched between the University of British Columbia (UBC), the Memorial University of Newfoundland (MUN) and C-CORE. The purpose of the project was to optimize soil liquefaction treatment using numerical and centrifuge testing and so reducing the cost associated with soil liquefaction (C-CORE 2004). A total of eight centrifuge tests have been carried out in this project and in this part, one of them was numerically modeled for the investigation of the effects of the porosity permeability relationship.

4.2.1. Description of the Model

In order to perform a numerical simulation of an experiment, the boundary and loading conditions have to be fully understood and then implemented into the model. So that, in this part, the basic mechanism of the centrifuge test will be explained briefly. Note that all this information will be used in the next part where we construct our model.

The test which has been conducted with a centrifuge having a working radius of 5.5 m with a maximum acceleration of $200g$ is shown in Figure 4.7.

Figure 4.7. C-CORE's 5.5m-radius, 200g capacity Actidyn centrifuge (C-Core)

One of the biggest challenges of the investigation of the geotechnical engineering problems in a laboratory environment is the poor representation of the field stress conditions. In other words, in the field, the behavior of the sample highly depends on the self-weight of it. But due to the obvious limitations of the facilities (both in time and space) small scale models have to be conducted. That is where the geotechnical centrifuge testing comes into play and by spinning the soil sample increases the weight so that the stress condition in the field is captured.

Although the centrifuge tests are one of the most commonly used and reliable methods for the testing physical scale models of geotechnical systems, they still have some limitations comparing the true behavior in the field. For example, in this part, a dyke consist of several layers of sand was simulated with a scale of 1:70 within a rigid frame whereas in reality soil is continuous.

In order to perform centrifuge experiment, first, the length of the centrifuge arm and target acceleration are set and then the physical model is prepared and placed into the swinging bucket, Figure 4.7. But in this experiment, an earthquake was simulated. So how to simulate an earthquake within a spinning bucket? To do that a special earthquake simulator shown in Figure 4.8 has been used.

Figure 4.8. Earthquake Simulator (C-CORE)

The 2D side view of the model is given in Figure 4.9. The model has a 51.6 m length and 20 m width in Z-direction and composed of three sand layers. At the bottom, a 1.4 m highly permeable drainage layer formed by coarse sand in order to create a one-dimensional saturation front. A 5 m of dense sand overlaid by the same type of loose liquefiable sand layer. The relative densities of these loose and dense sand layers are provided as 40% and 80% respectively (C-CORE 2004). Note that water level is 1 m above at the crest and 8 m at the toe.
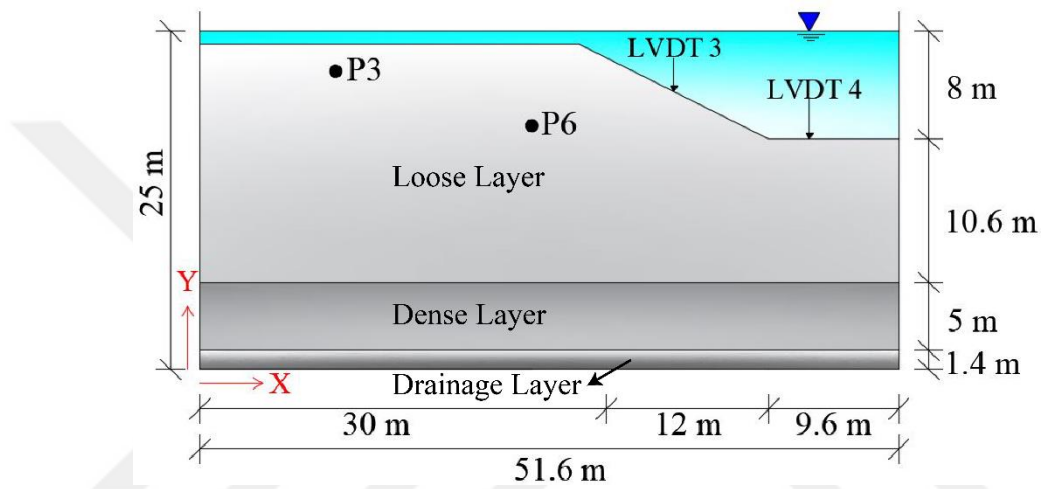
Figure 4.9. 2D model configuration

The finite element model consisting of the coupled two-phase u20p8 element is given in Figure 4.10. All the nodes at the bottom of the model were fixed in Y-direction according to the coordinate system defined in Figure 4.9 and 4.10. The sides of the model are also fixed in the relative vertical dimensions. For example, all the nodes located at the Z=0 m surface were fixed in the Z direction. Similarly, the nodes located at the remaining three sides: Z=20, X=0 and X=51.6 also fixed in the corresponding vertical directions. During the preparation of the physically reduced scale model, a stain-less steel bucket has been used. Hence, the friction between the side of the bucket and the sand was neglected in the numerical modeling. Finally, except the ground surface of the model, all the remaining boundaries are modeled as impermeable so that pore pressures could build-up.

Figure 4.10. Finite element model used in simulations with meshing structure
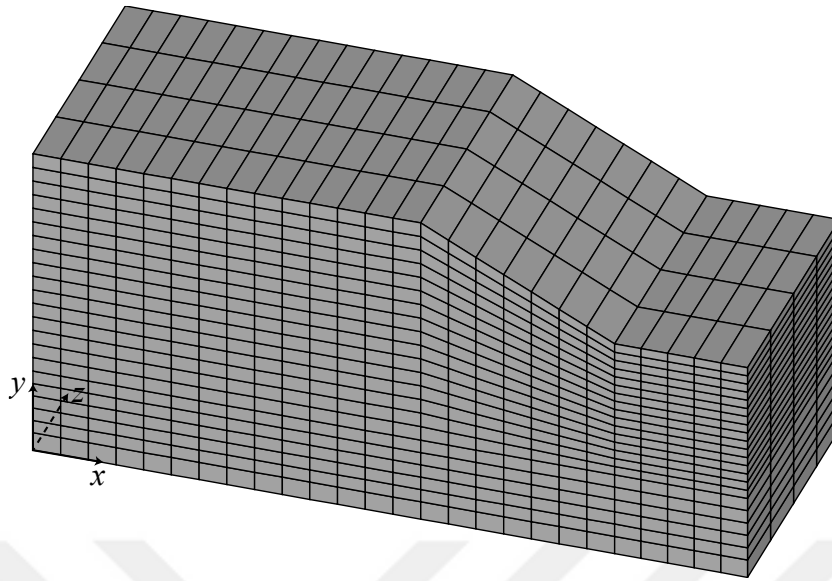
In this centrifuge experiment, the Fraser River sand that has been previously used for the simulation of the cyclic direct simple shear test has been used. The hypoplastic material parameters of the sand are given in Table 3.3. Using the material parameters and the provided relative densities, the initial void ratios of the loose and dense specimen were calculated as $e_{0,\,loose} = 0.812$ and $e_{0,\,dense} = 0.684$.

The hydraulic conductivity of the loose sand at 40% relative density was provided as $k_{d,\,loose} = 4.3 \times 10^{-4}$ m/s. And also, the particle size distribution of the Fraser river sand has been given in the C-CORE report. Using all these data and Equation 2.90, the Kozeny-Carman constant is determined as $C_{KC} = 1.455 \times 10^{-4}$ m/s. Using this constant, the initial permeability of the finite element model is set equal to the initial hydraulic conductivity of the experimental model. Note that, since dense and loose sand layers composed of same sand materials, they have same granular properties. So that, the Kozeny-Carman coefficient determined for the loose layer is also used for the dense layer. Using that coefficient, the initial permeability of the dense layer was determined as $k_{d,\,dense} = 2.76 \times 10^{-4}$ m/s.

The behavior of the coarse drainage layer is assumed to be linearly elastic with a modulus of elasticity of $E_{drainage} = 10^5$ kN/m^2 and Poisson's ratio, $v_{drainage} = 0.3$ due to missing soil data. The hydraulic conductivity of the drainage layer was set to 100 times the loose sand layer's hydraulic conductivity value, $k_{d, drainage} = 4.3 \times 10^{-2}$ m/s. This is also suggested by the C-CORE. Considering the remaining part of the system, the porosity-permeability dependence of the drainage layer is neglected.

4.2.2. Numerical Simulation and Results

Before simulating the earthquake loading conditions, the numerical analysis was performed under gravitational load only. By doing so, the required state parameters of the hypoplastic constitutive model have been obtained. After that, the earthquake load given in Figure 4.11 was applied to the system. Considering the centrifuge test and the bucket where the experiment was conducted, and keeping mind that there is no friction between the bucket and soil, the dynamic load given in Figure 4.11 was applied to the nodes located at Y=0 m surface, also both X=0 m and X=51.6 m surfaces. The reason of applying earthquake loading to the nodes located at Y=0 is the existing drainage layer at the bottom.
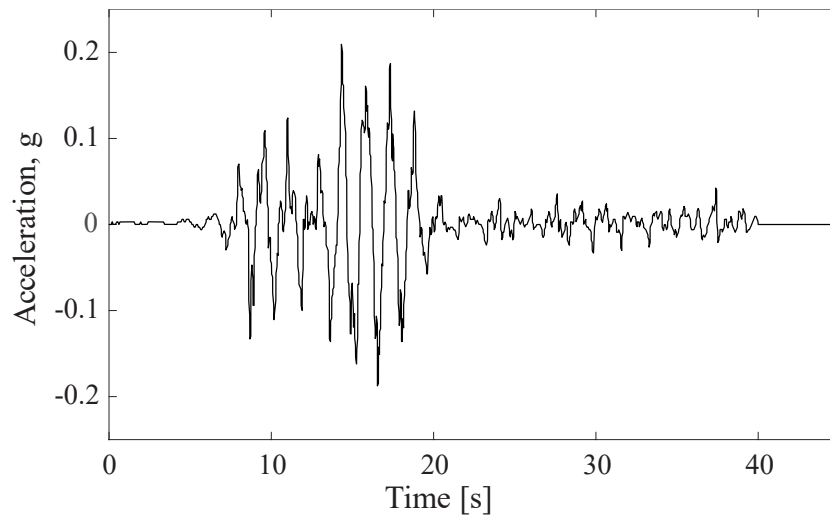

Figure 4.11. Horizontal earthquake input

99

A solid, durable data acquisition system is extremely important for a centrifuge test. Because the devices and acquisition systems used in these tests have to withstand 200 times the Earth's gravity. At least 20 times what the human body can withstand. In this experiment, some of the LVDTs are broken during the test. So that, for the comparison of the numerical results with the experimental data, P3 and P6 pore pressure transducers and for the displacements LVDT3 and LVDT4 data were used. The location of these devices is given in Table 4.3.

Table 4.3. *Location of pore pressure transducers and LVDTs*

	X	Y	Z
P3	10.0 m	22.0 m	10.0 m
P6	24.5 m	18.0 m	7.0 m
LVDT3	35.0 m	20.5 m	10.0 m
LVDT4	45.0 m	17.0 m	10.0 m

The effects of the porosity-permeability relationship were investigated using the pore pressure accumulation and displacement results given in Figures 4.12, 4.13, 4.14 and 4.15. Note that each comparison consists of two numerical simulations: one with the Kozeny-Carman implemented and another one without that implementation.
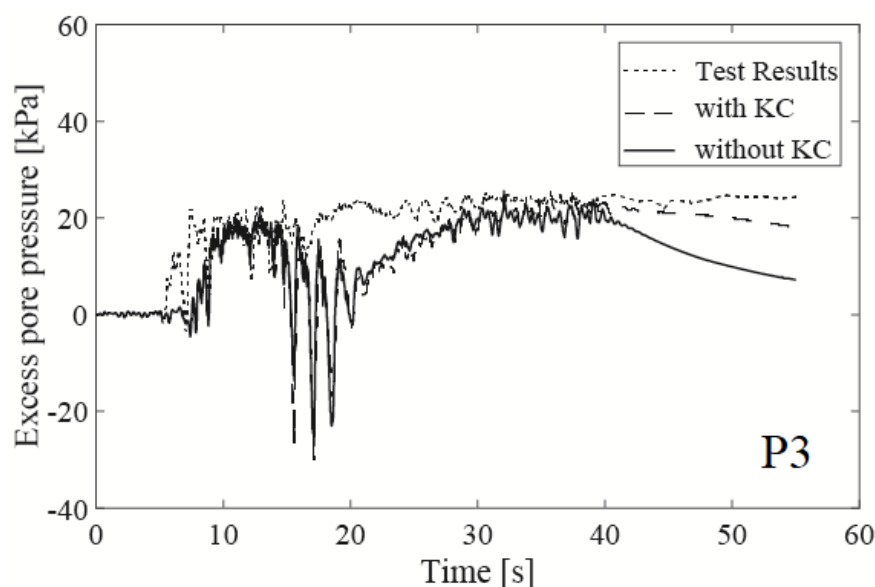

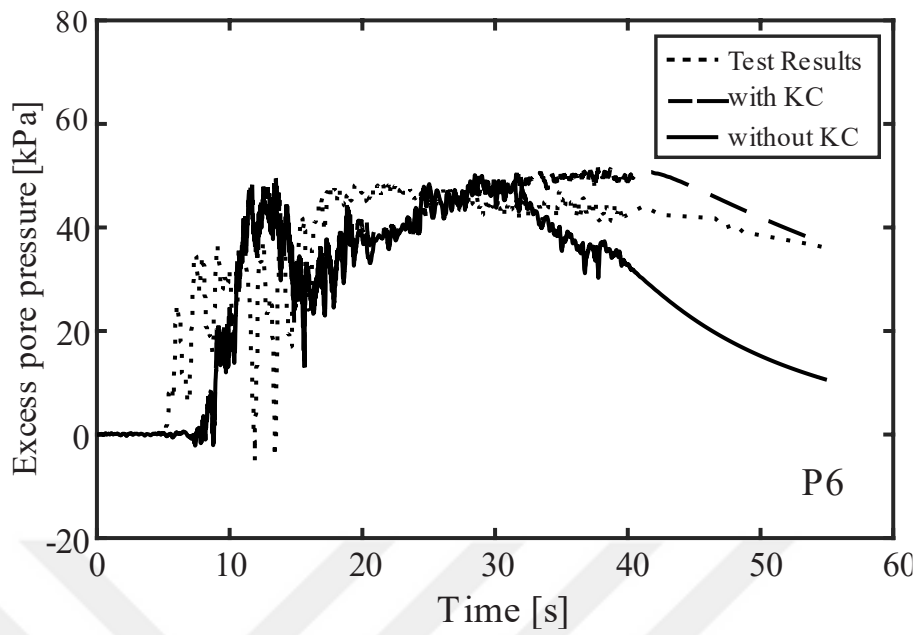Figure 4.12. Time histories of excess pore pressures at P3

Figure 4.13. Time histories of excess pore pressures at P6
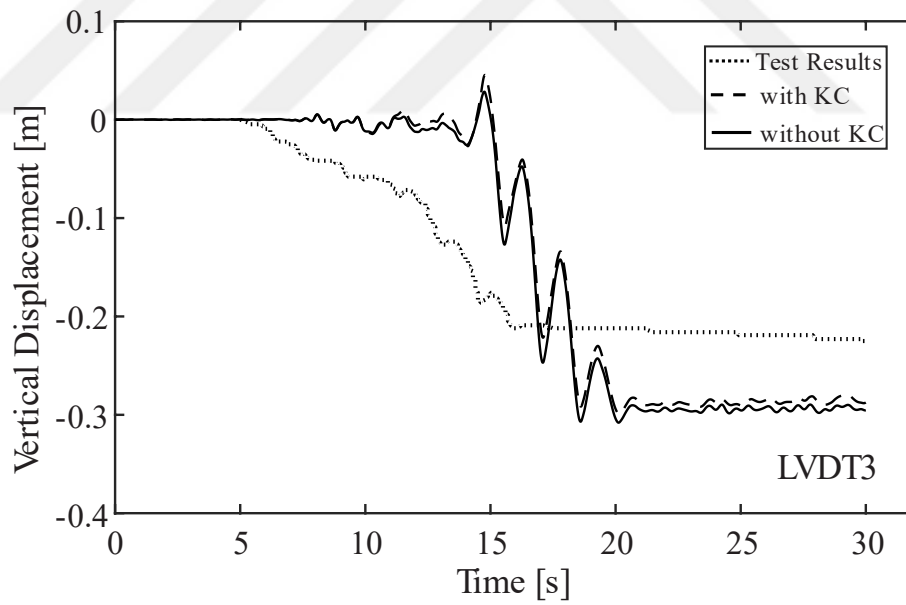
Figure 4.14. Time histories of vertical displacements at LVDT3
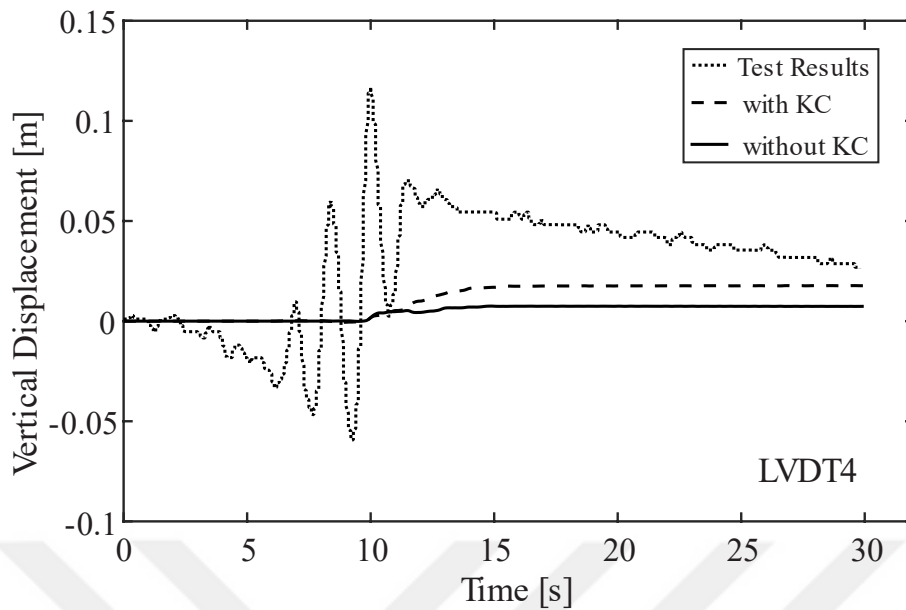
Figure 4.15. Time histories of vertical displacements at LVDT4

The quality of the excess pore water pressure predictions varies; although it is satisfactory for the given two cases. However, comparing the results obtained from the experiment, displacements are not predicted adequately in the simulations. The comparison of the experimental test with the FE results, especially the pore pressure predictions, proves that the simulations with Kozeny-Carman implementation yield more satisfactory results comparing to one without the porosity-permeability relationship implementation.

The main difference between the two simulations is, in the case of "without KC", the accumulated pore pressure starts to decrease rapidly after the completion of the dynamic earthquake loading process. However, according to the experimental test results, the simulation with the Kozeny-Carman relationship allows a more accurate pore pressure dissipation phase.

4.3. Numerical Modeling of an Offshore Gravity Foundation

A gravity-based jacket type offshore wind turbine foundation has been modeled to investigate the effects of the changing permeability on the cyclic behavior of a wind turbine foundation.

102

Offshore foundations are exposed to extreme loading conditions due to harsh and marine aggressive environment. In such a condition, depending on the number of the extreme cycles, amplitude and frequency of the loading, soil underneath these huge structures may start to build-up excess pore pressure and eventually due to the stiffness degradation severe tilts may occur. Over 25 years of design life, number of cycles an offshore structure would be subjected to is approximately 10^7 cycles of wave loading which is the dominant cyclic load component.

In this part, a true scale offshore foundation system adopted from (Sturm 2011) was numerically simulated under varying loading conditions. The geometry of the offshore structure is given in Figure 4.16. The minimum required weight of the offshore structure was determined according to the height of the 25 years returned period of the wave. All the detailed information regarding the decision of the size of the structure and the determination of the design loads are provided in the related article. In this study, rather than the realistic representation of the behavior of an offshore structure, the effects of the porosity-permeability variation were focused. In other words, the loading scenarios were not determined for the optimum design, but for the investigation of the porosity-permeability effects.
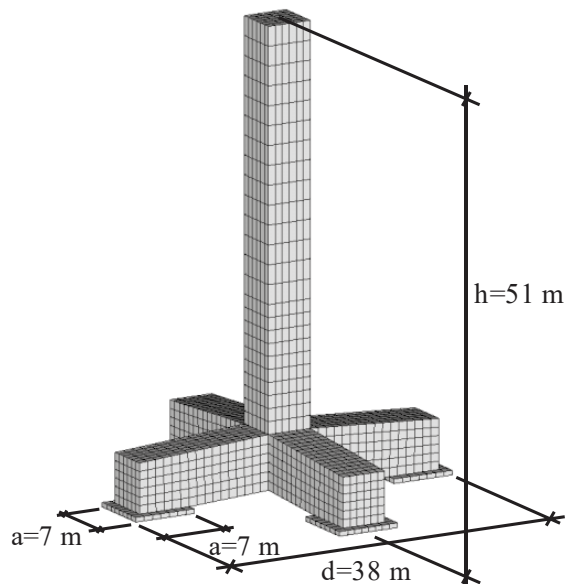

Figure 4.16. Geometry and dimensions of the concrete foundation, Sturm (2011)

The geometry of the finite element model is given in Figure 4.18. In order to eliminate the effects of the boundary conditions, the radius and the depth of the model were selected as 60 meter. Great attention was paid for an effective soil meshing, Figure 4.19.

Since the model is symmetric and loading is applied in one direction, half of the model is simulated. The boundary conditions are selected such that there will be no vertical displacement at the bottom of the model and also radial displacements are prevented at the outer radius of the soil. Since the model is symmetric, the degree of freedom of the nodes at the Y=0 is set to zero in Y direction.

In this study, the parameters of the Baskarp sand which is provided in Table 4.4 were used. According to the provided initial condition, the relative density of the sand before the placement of the offshore structure is equal to, $I_D = 60\%$ and corresponding hydraulic conductivity is given as, $k_d = 5.5 \times 10^{-5}$ m/s. Using Equation 2.90, the Kozeny-Carman constant is determined as 3.3338×10^{-4} m/s.

Table 4.4. *Baskarp sand hypoplastic material parameters, Sturm (2011)*

φ_c	h_s[MPa]	n	e_{d0}	e_{c0}	e_{i0}	α	β
32.5°	18000	0.26	0.505	0.862	0.991	0.11	1.0

R	m_R	m_T	β_R	χ
1.0×10^{-4}	6.0	6.0	0.15	1.0

Using the above provided boundary and initial conditions, the numerical model first analyzed under gravitational loading only, without any lateral loading on it. And then lateral load increased up to H_{mean} value and finally cycling loading with an amplitude of H_{cyc}^{amp} was initiated as shown in the Figure 4.17. Note that, before the initiation of the loading, a zero lateral load region is shown in the Figure 4.17. This is the time domain where the analysis was performed for the determination of the deformations due to the soil's and structure's own weights. In this numerical model, for the simplicity of the calculations, all the components of the load (e.g. wind, wave) were applied to the system from the top of the offshore structure.
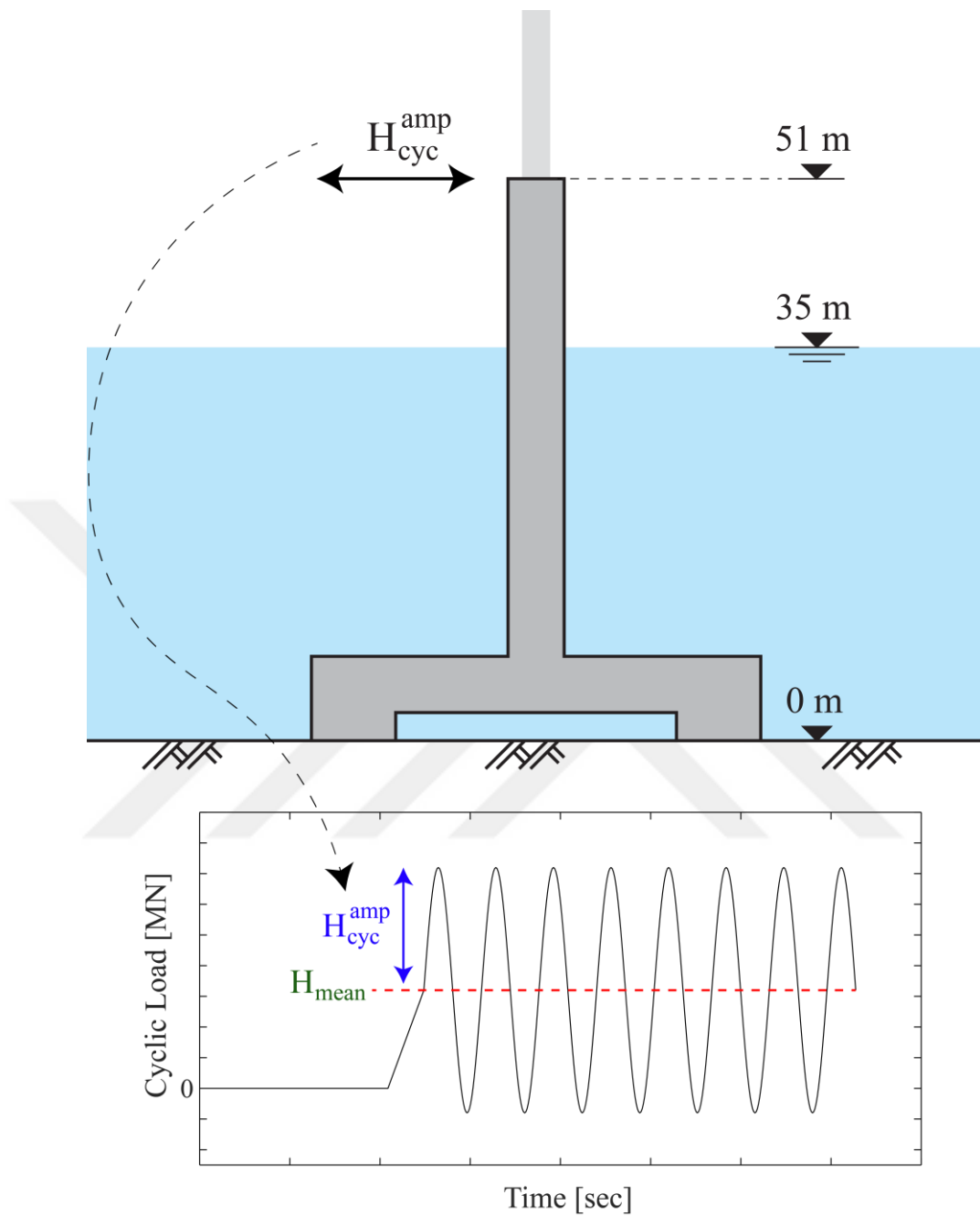
Figure 4.17. Description of idealized lateral loading on the offshore wind turbine structure

The soil structure interaction between the offshore turbine and soil was established using sophisticated CONTA174 and TARGE170 elements in ANSYS. The friction coefficient of the contact surface was assumed to be equal to the critical state soil

friction angle as suggested by the (Sturm 2011). Using these elements, after the placement of the structure an impermeable zone underneath the footings were created.

Figure 4.18. 3D FE model of offshore gravity base foundation system
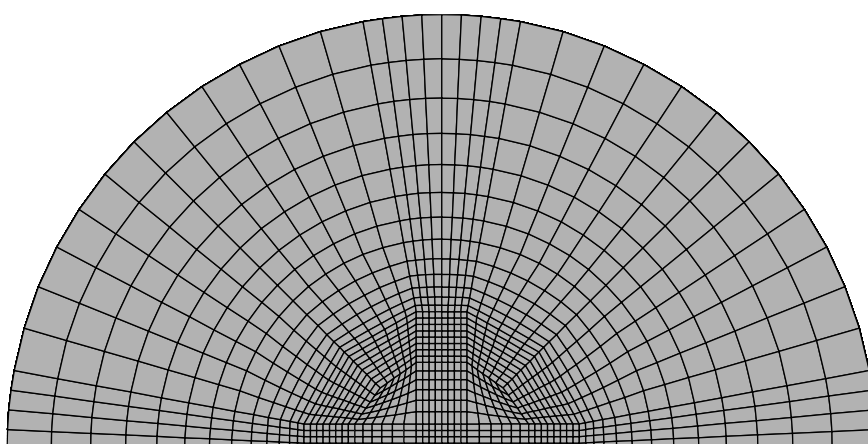
Figure 4.19. Finite element mesh of soil underneath the offshore structure

During the consolidation stage, the mass of the structure increased linearly in order to prevent possible convergence problems. To do that, the density of the structure increased linearly using MPCHG command in ANSYS. In order to minimize the effect of the inevitably accumulated rounding error, only the first 15 cycles are investigated in the numerical analyses.

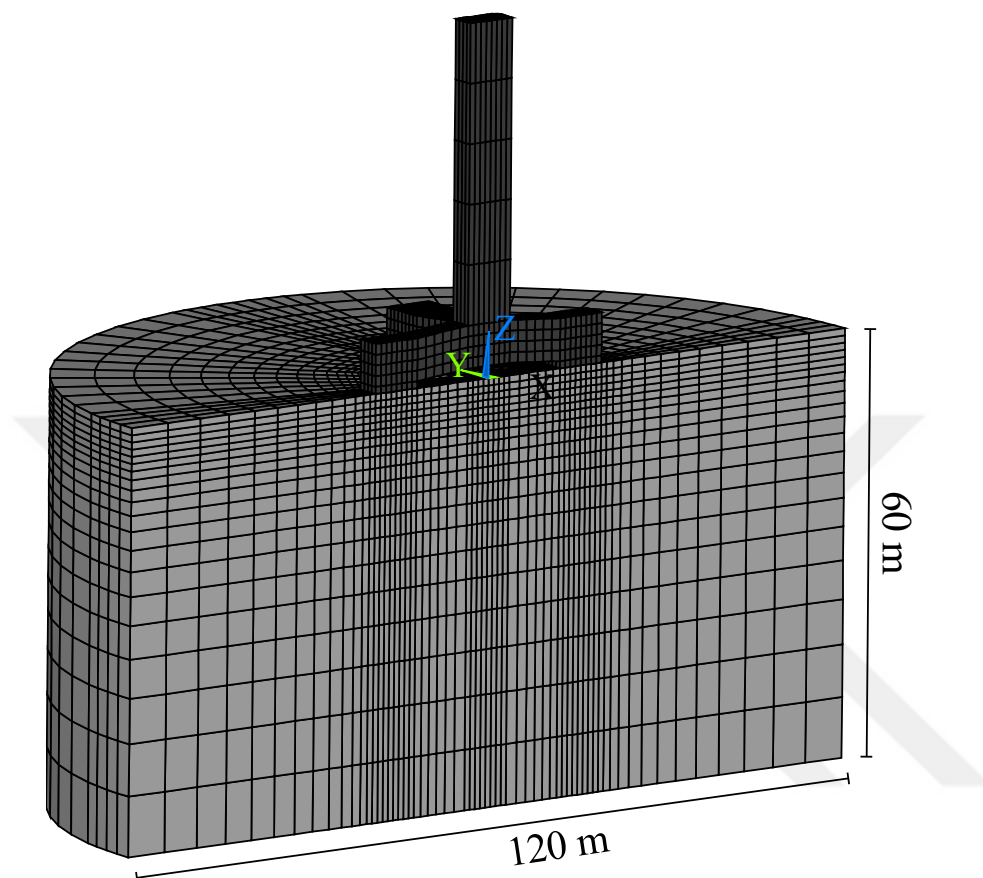Finally, hypoplastic material model together with two-phase u20p8 finite element was used for the investigation of the cyclic behavior of the soil. On the other hand, the offshore structure was modeled using a linear elastic material model with a very high elasticity modulus, simply assumed to be rigid.

The cyclic load given in Figure 4.20 is applied to the system from the top of the structure in the positive X direction according to the coordinate system defined in Figure 4.18.
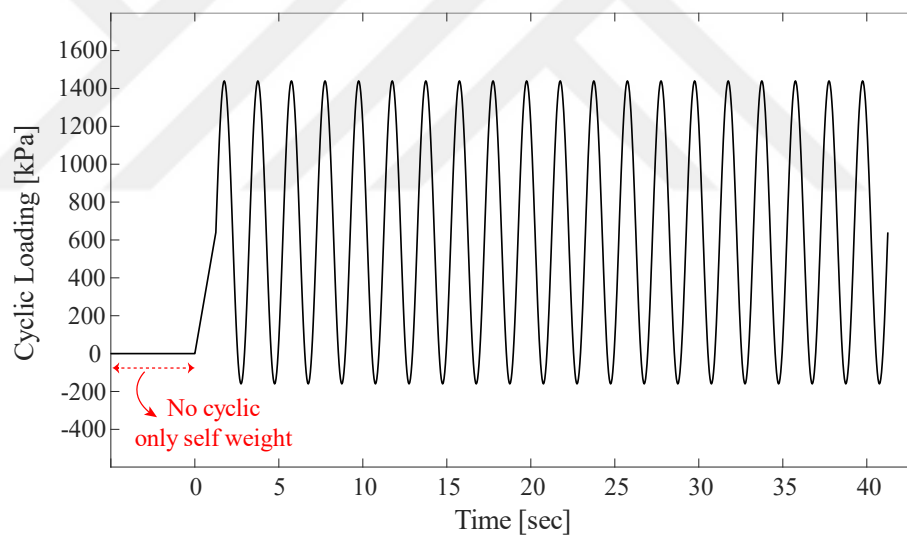
Figure 4.20. Offshore structure applied cyclic loading

The resulting displacements and excess pore pressure developments underneath the footings of the offshore structure are given in Figure 4.21, 4.22 and 4.23. In these figures, the right and left legs correspond to the half footings. The right leg is located in the positive X direction and expose to the major cyclic loading whereas the left leg is located in the negative X direction.
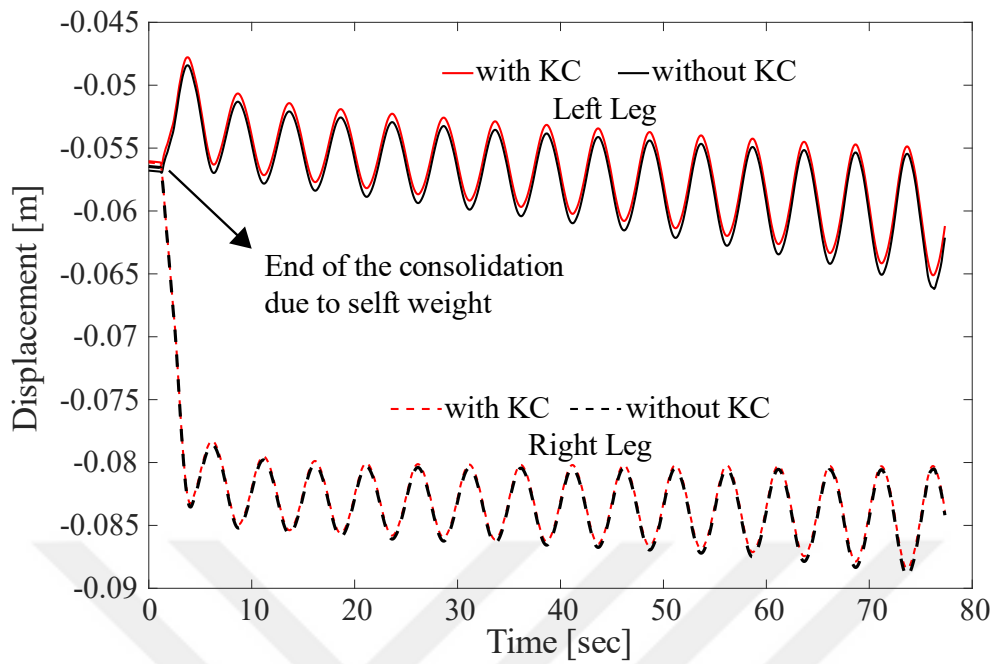
Figure 4.21. Displacements at right and left half legs of the offshore structure
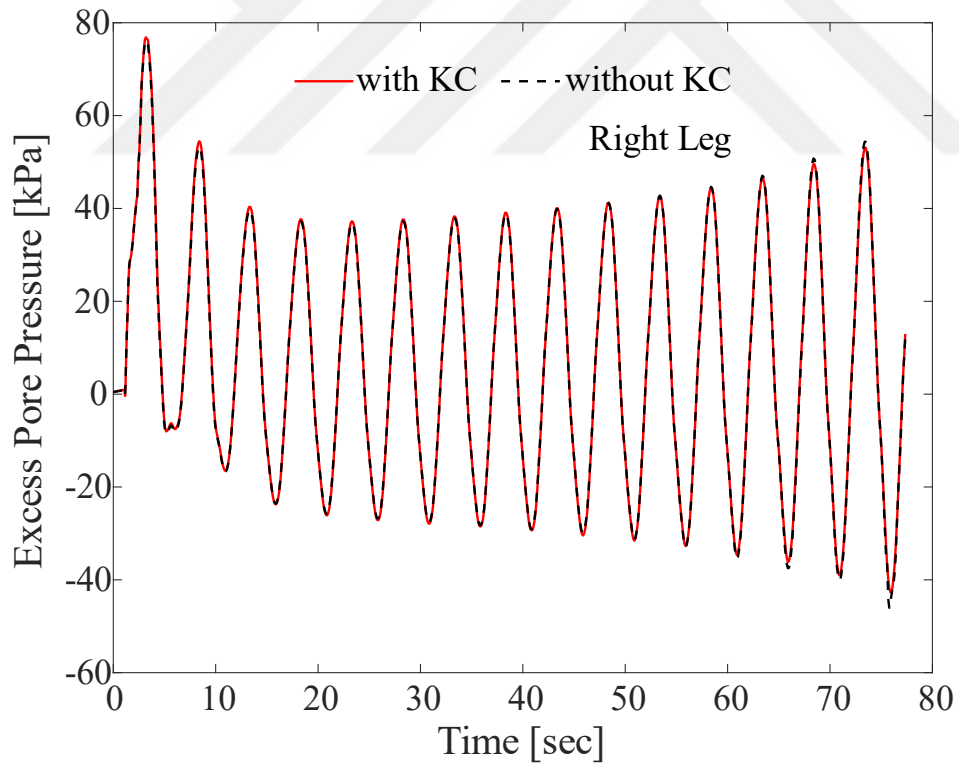
Figure 4.22. Excess pore pressure developments at the right half leg of the offshore structure

108
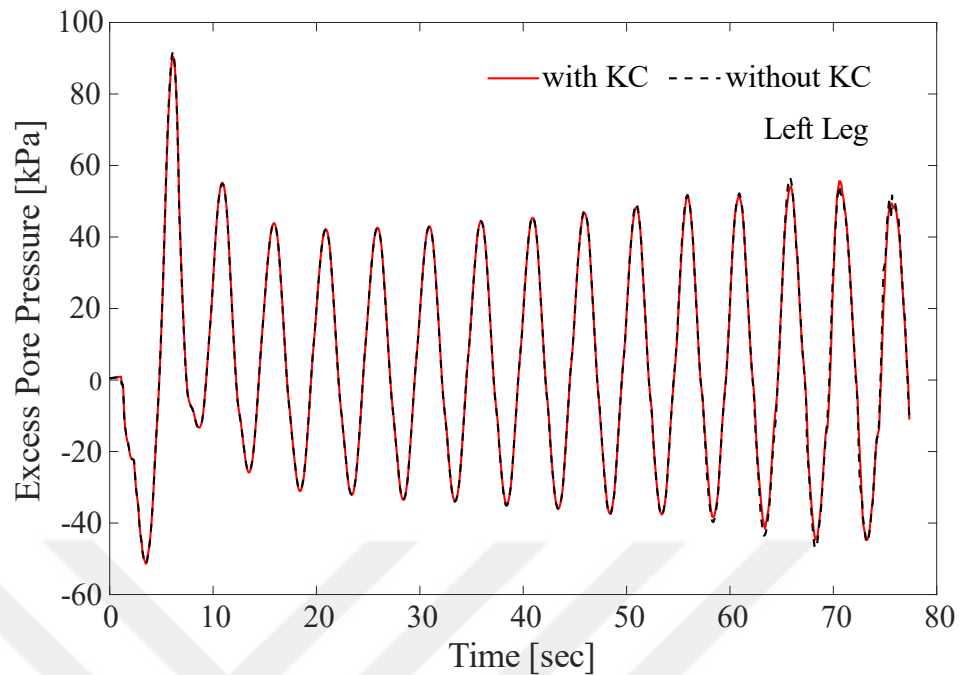
Figure 4.23. Excess pore pressure developments at the left half leg of the offshore structure

According to the results provided above, there is no significant difference between the two cases: with and without Kozeny-Carman implementation. The main reasons for this similarity are the initial condition and the consolidation stage defined before the initiation of the cyclic loading. Majority of the displacements take place during the installation (or placement) of the gravity foundation due to the self-weight of the structure. During the self-weight induced consolidation, it is assumed that there is no excess pore pressure development underneath the offshore structure. Also note that, due to the void ratio decrease around the offshore footings, the permeability of the soil in these are already reduced without any change in excess pore pressure, so that it is reasonable to have no difference between two cases. Since the permeability is directly defined by the current void ratio, the majority of the change in permeability occurred during the installation without any excess pore pressure developments.

For the illustrative purposes, the excess pore water pressure contours and lateral displacements of the offshore structure at the peaks of the 5th and 15th cycles are given in the Figures 4.24, 4.25, 4.26, 4.27, 4.28 and 4.29.
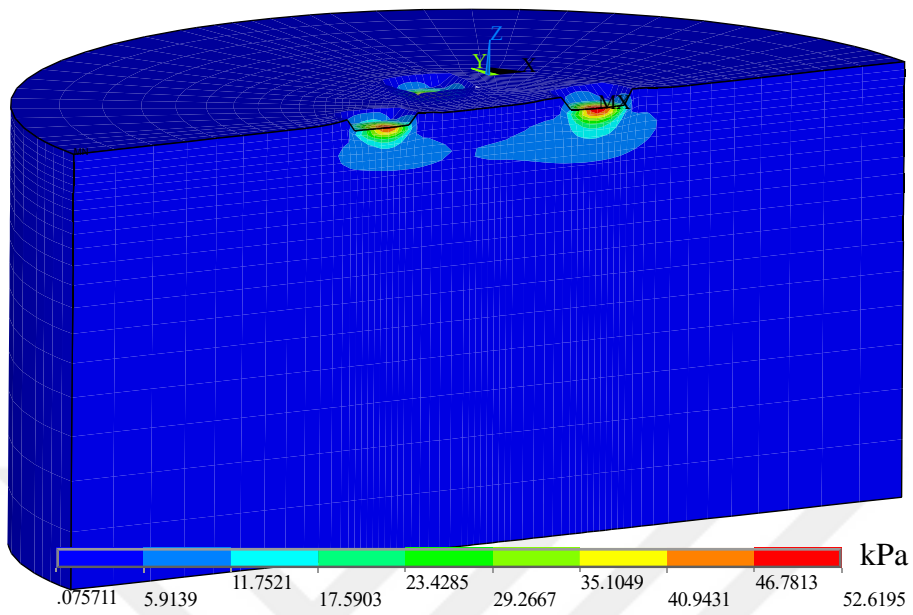
Figure 4.24. Excess pore pressure developments, 5th cycle
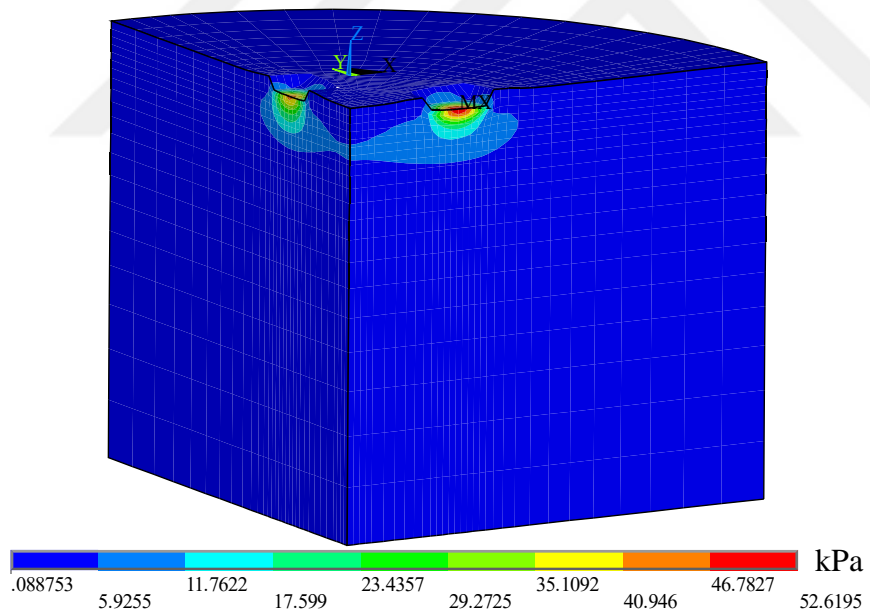
Figure 4.25. Excess pore pressure developments, 5th cycle
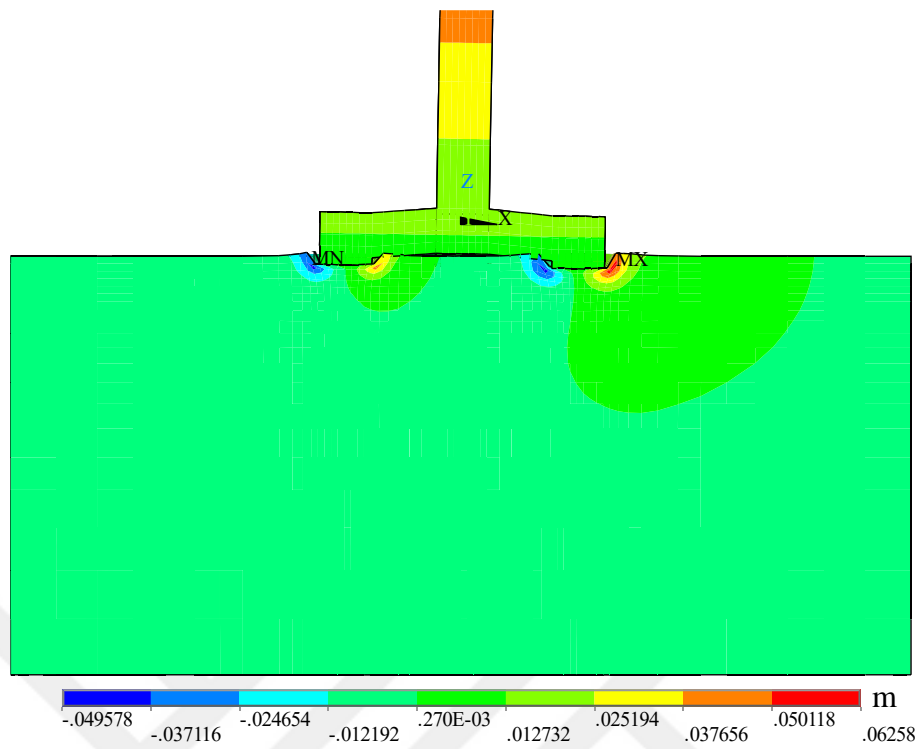
Figure 4.26. Lateral displacement in the loading direction, 5th cycle
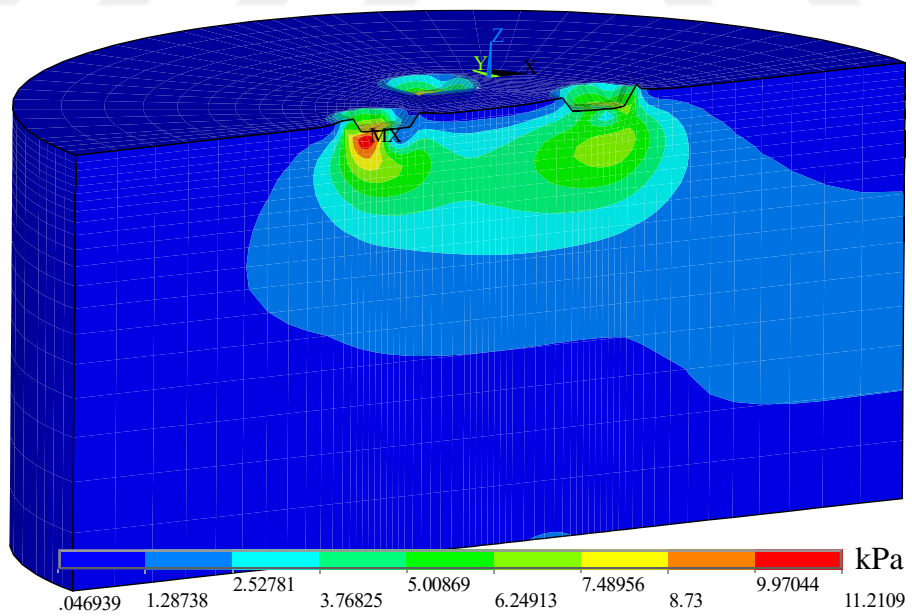
Figure 4.27. Excess pore pressure developments, 15th cycle

Color scale:

.054426		2.27735		4.50028		6.7232		8.94613	kPa
	1.16589		3.38882		5.61174		7.83467		10.0576
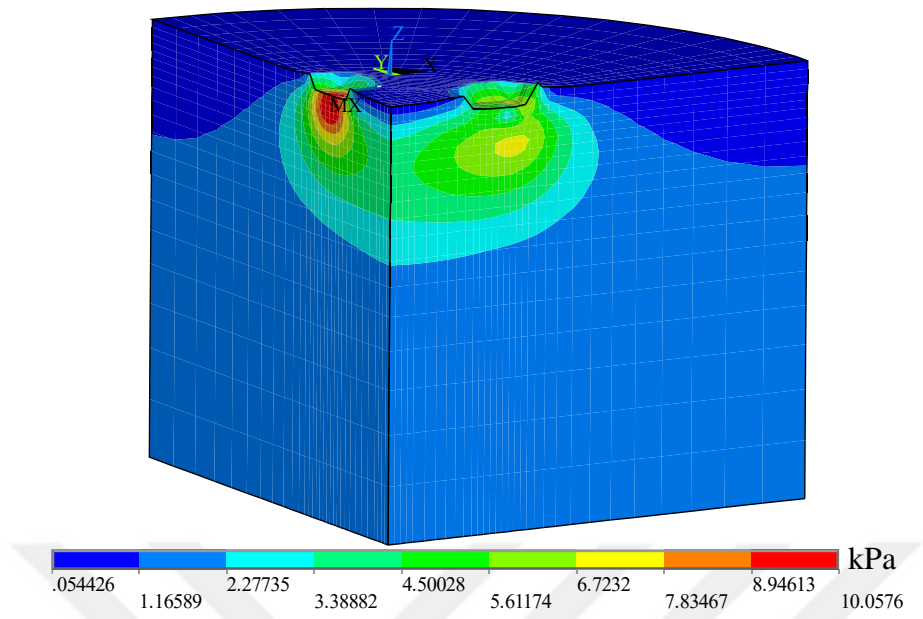
Figure 4.28. Excess pore pressure developments, 15th cycle

Color scale:

-.083623		-.046329		-.009034		.02826		.065554	m
	-.064976		-.027682		.009613		.046907		.084201
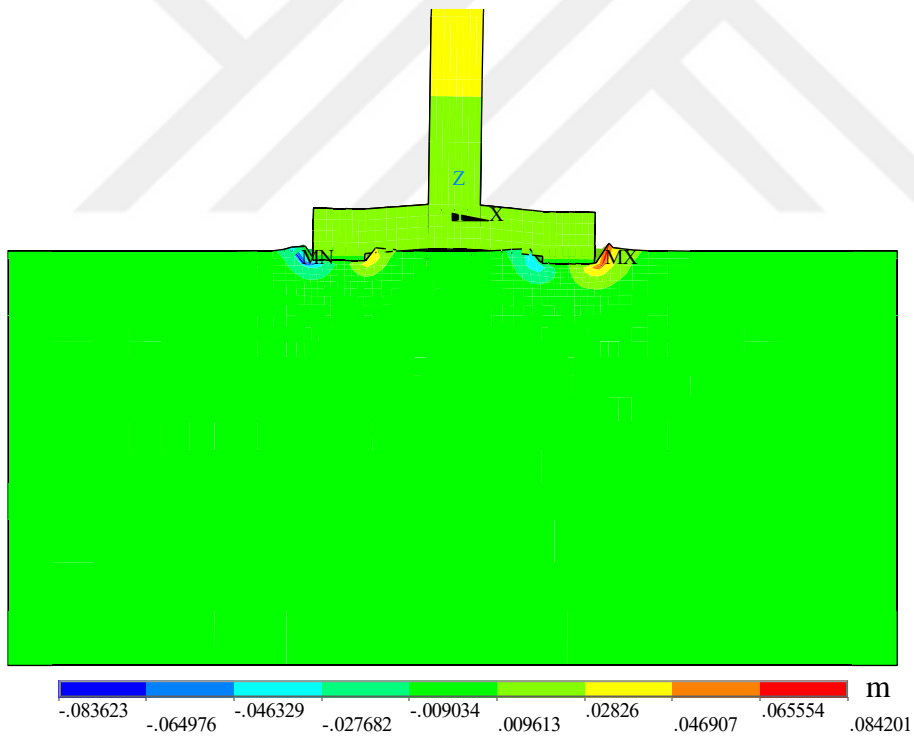
Figure 4.29. Lateral displacement in the loading direction, 15th cycle

CHAPTER 5

CONCLUSIONS AND RECOMMENDATIONS FOR FUTURE STUDIES

5.1. Summary

In this thesis, the effects of the porosity dependent permeability variation on the mechanical behavior of the soil were investigated for various type of geotechnical problems such as an earthquake induced dyke and jacket type offshore gravity foundation system. The hypoplastic constitutive model together with a fully coupled two-phase u20p8 finite element has been used for the numerical investigations. The variation of permeability is defined as a function of the current void ratio and implemented into the finite element framework using the Kozeny-Carman relationship.

Before performing the geotechnical simulations, all the steps and implementations are verified and validated one by one. The available experimental studies have been used for the validation of the hypoplasticity and the two-phase model. Finally, the Kozeny-Carman implementation is validated by conducting a laboratory experiment. During this experiment, hypoplastic material properties of the sand used in the test were determined and during this parameter determination stage, some improvements to ease the determination of these parameters were suggested such as image processing for the determination of the critical friction angle.

In the finite element model, both the solid and fluid particles are considered to be linearly elastic (compressible). The bulk modulus of the grains and water are taken as $K_s = 2 \times 10^9$ kPa and $K_w = 2 \times 10^6$ kPa, respectively. Although the compressibility of the solid and fluid particles has a negligible influence on the mechanical behavior of granular soils, their consideration enables further possible uses of the model.

The finite element software ANSYS has been used for the numerical analyses.

5.2. Conclusions

The results of this study can be summarized as follows:

- The selection of a suitable constitutive model is key for the realistic prediction of the soil behavior. Although there are many constitutive models available in the literature, developed for the granular soils, only some of them are capable of maintaining this highly nonlinear stress-strain relationship during the dynamic and cyclic loading conditions. At this point, the extended hypoplasticity provided satisfactory results and made it possible to investigate complex soil behavior. The accuracy of the model is already verified by many researchers and its popularity continuously increases. As a drawback of the model, the determination of the hypoplastic material parameters are complex and some of them have no physical corresponding which make them difficult to understand. The second difficulty in hypoplasticity is the variability of the material parameters. Hypoplastic material parameters are defined within a stress range so that it is possible to find two different sets of parameters for a single type of soil. For example, although the maximum and minimum void ratios do not vary for a single type of sand, the parameters h_s and n which are defined within a predefined stress range may vary a lot depending on the stress range selection.

- The complex fluid particle interaction in fully saturated soils is taken into account by the implementation of the two-phase model. For the numerical simulation of the water saturated sands, u20p8 finite element is used together with the hypoplastic constitutive model. Using two element test results, one undrained cyclic triaxial and undrained cyclic simple shear test, it has been shown that the complex response of the soil skeleton and its interaction with the pore water which results in pore pressure developments, can be reproduced numerically, including the liquefaction phenomena. It should be noted that the adopted two-phase model which is based on formulation developed by

Zienkiewicz & Shiomi (1984) neglects the wave propagations and considers a relatively slow speed flow in porous media. Although this assumption is valid for the static or slow speed monotonic loading conditions, the importance of the wave propagation phenomena should be investigated for a more accurate dynamic response of porous media.

- For the investigation of the porosity-permeability variation, among the many alternatives, void ratio dependent Kozeny-Carman relationship is selected. Although this relationship is developed for the slow speed laminar flow conditions, the numerical simulation of the earthquake loaded dyke proved that the Kozeny-Carman equation can still improve the dynamic prediction of the saturated soil behavior.

- Three different case studies were carried out for the investigation of the effects of the porosity-permeability variation on the fully saturated sandy soils. In the first simulation, soil in an impermeable rigid box exposing vertical cyclic loading was simulated for various conditions. Note that, this is also the geometry of the experimental setup that was used for the validation of the Kozeny-Carman relationship. Although this model does not correspond to any physical soil condition, the rather simple boundary and 1D flow conditions help carrying out parametric studies. (An example for the effects of the increasing frequency and amplitude of the cyclic loading has already provided.) Overall higher excess pore pressure generations were determined for the analysis with KC compared to the simulation without KC. And a result considerably larger settlements were generated in "without KC" case. In this part, it is found that application of any monotonic slow speed loading prior to the cyclic loading, reduces the effects of the Kozeny-Carman implementation. Note that, the development of excess pore pressure depends on the type of loading. In case of deformation without significant pore pressure development, although the permeability changes, effects of it becomes negligible. Overall higher excess pore pressure generations were determined for the analysis with

115

KC compared to the simulation without KC. And a result considerably larger settlements were generated in "without KC" case.

- The second case study was carried out for an earthquake induced dyke. In this experiment, since there was no prior significant loading before the earthquake, the effects of the implemented permeability relationship were observed more clearly. A comparatively more accurate pore pressure dissipation phase was predicted with the Kozeny-Carman implementation.

- Finally, the behavior of a jacket type offshore gravity foundation system was investigated. Before the initiation of the lateral cyclic loading, the installation procedure of the offshore structure was simulated. The results show that the majority of the loading took place during this consolidation stage. Referring to the previous explanation of the slow loading scenario, again the decrease in void ratio without a significant change in pore pressure decreased the influence of the effects of the Kozeny-Carman implementation. As a result, no significant difference could be detected with the implementation of the permeability relationship.

- The influence of the porosity permeability variation on the mechanical behavior of the soil was tired to be formulated using Kozeny-Carman equation. Together with the different size and type of case studies, the necessity of the consideration of the permeability implementation was questioned. As a result, it is suggested to consider porosity dependent permeability variation for an accurate simulation of the dynamic soil problems.

5.3. Future Studies

The particle-fluid interaction underpins the key behavior of granular soils in many applications. Conventional approaches have been based on continuum, phenomenological theories of porous media offer limited information at the microscale governing the interacted system of particles and fluid. At this point, the microscopic behavior of the fluid-particle interaction may provide insights to the

overall understanding of granular materials. The investigation of the porosity-permeability relationship not just by the void ratio but also considering other important micro level factors such as the granulometric properties of the sand and dynamic load induced wave propagation within the porous domain would definitely increase the accuracy of the model and provide a better understanding for the dynamic behavior of the soil. To do that a coupled CFD-DEM numerical tool can be developed to simulate the fluid-particle interactions in granular soils.

REFERENCES

Albers, B., Savidis, S. A., Tasan, E. H., von Estorff, O., and Gehlken, M. (2012). "BEM and FEM results of displacements in a poroelastic column." *International Journal of Applied Mathematics and Computer Science*, 883-896. doi:10.2478/v10006-012-0065-y

Alyamani, M. S., and Sen, Z. (1993, July). "Determination of hydraulic conductivity from complete grain-size distribution curves." *Groundwater, 31*, 551-555. doi:10.1111/j.1745-6584.1993.tb00587.x

Anaraki, K. E. (2008). *"Hypoplasticity Investigated: Parameter Determination and Numerical Simulation."* Delft: Delft University of Technology. Retrieved from http://resolver.tudelft.nl/uuid:71e5eb73-06ca-48d2-b442-ce2639f995fc

Anaraki, K. E. (2008). *"Hypoplasticity investigated-parameter determination and numerical simulation."* Delft University of Technology.

Andersen, K. H. (2007). "Bearing capacity under cyclic loading – offshore, along the coast, and on land." *Canadian Geotechnical Journal*, 513-535.

ANSYS. (2018). *"ANSYS® Academic Research Mechanical, Release 18.1, Help System, Coupled Field Analysis Guide, ANSYS, Inc."* ANSYS Inc.

Atkinson, J. H., Richardson, D., and Stallebrass, S. E. (1990, January). "Effect of recent stress history on the stiffness of overconsolidated soil." *Géotechnique*, 531-540. doi:10.1680/geot.1990.40.4.531

Aubram, D., Rackwitz, F., Wriggers, P., and Savidis, S. (2015, April). "An ALE method for penetration into sand utilizing optimization-based mesh motion." *Computers and Geotechnics*, 241-249. doi:10.1016/j.compgeo.2014.12.012

Barbour, S. L., and Krahn, J. (2004). *"Numerical Modelling – Prediction or Process?"* Geotechnical News. BiTech Publishers Ltd

Bauer, E. (1995). "Constitutive modeling of critical states in hypoplasticity." *Numerical Models in Geomechanics - NUMOG V*, Rotterdam, 15-20.

Bauer, E. (1996, March). "Calibration of a comprehensive hypoplastic model for granular materials." *Soils and Foundations, 36*(1), 13-26. doi:10.3208/sandf.36.13

Bauer, E., Wu, W., and Huang, W. (2003). "Influence of initially transverse isotropy on shear banding in granular materials." In J. F. Labuz, and A. Drescher (Ed.), *Proceedings of the International Workshop on Bifurcations and Instabilities in Geomechanics*, Balkema: Rotterdam 161-172.

Bayraktaroglu, H., and Taşan, E. H. (2018). "Effects of sandy soils permeability variation on the pore pressure accumulation due to cyclic and dynamic loading." *9th European Conference on Numerical Methods in Geotechnical Engineering*, CRC Press: Porto, Portugal 443-449.

Bayraktaroglu, H., Taşan, H. E., and Huvaj, N. (2018). "Determination of the hypoplastic constitutive model parameters for the sandy soils." *17th National Soil Mechanics and Geotechnical Engineering Conference (ZMGM 2018)*, Istanbul, 285-298.

Been, K., Jefferies, M., and Hachey, J. (1991, September). "The critical state of sands." *Géotechnique, 41*(3), 365-381. doi:10.1680/geot.1991.41.3.365

Biot, M. A. (1941). "General theory of three-dimensional consolidation." *Journal of applied physics*, 155-164.

Biot, M. A. (1956). "Theory of propagation of elastic waves in a fluid-saturated porous solid." *The Journal of the Acoustical Society of America, 28*(2), 168-191. doi:10.1121/1.1908239

Biot, M. A. (1962). "Mechanics of deformation and acoustic propagation in porous media." *Journal of Applied Physics, 34*, 1254-1264. doi:10.1063/1.1728759

Bocchi, F. (2014, October 16). *https://www.comsol.nl/*. Retrieved from Comsol Blog: https://www.comsol.nl/blogs/yield-surfaces-plastic-flow-rules-geomechanics/

Booker, J. R. (1974). "The consolidation of a finite layer subject to surface loading." *International Journal of Solids and Structures, 10*(9), 1053-1065. doi:10.1016/0020-7683(74)90011-0

Burland, J. B. (1987). "Nash lecture: the teaching of soil mechanics—a personal view." *Proceedings of the 9th European Conference on Soil Mechanics and Foundation Engineering*, Dublin, *3*, 1427-2447.

Carman, P. C. (1937). "Fluid flow through a granular bed." *Transaction of the Institution of Chemical Engineers*, 150-156.

Carman, P. C. (1956). *"Flow of gases through porous media."* New York: Academic Press.

Carter, J. P. (2006). "Who needs Constitutive Models?" *Australian Geotechnics*, 1-27.

Cary, C. E., and Zapata, C. E. (2016). "Pore water pressure response of soil subjected to dynamic loading under saturated and unsaturated conditions." *International Journal of Geomechanics*.

C-CORE. (2004). *"Earthquake Induced Damage Mitigation from Soil Liquefaction-Data Report of Centrifuge Test CT1 and CT2."* Centre for Cold Ocean Resources Engineering, C-CORE: Canada

Chatra, A. S., and Dadagoudar, G. R. (2010). "Numerical simulation of hypoplastic constitutive model for sand." *Indian Geotechnical Conference 2010.*, Department of Civil Engineering IIT Chennai: Mumbai

Chavez Abril, M. (2017). *"Numerical simulations of static liquefaction in submerged slopes."* Delft: Delft University of Technology. Retrieved from http://resolver.tudelft.nl/uuid:0a9b2bec-eb67-4954-b5aa-083913be3f38

Di, Y., and Sato, T. (2003). "Liquefaction analysis of saturated soils taking into account variation in porosity and permeability with large deformation." *Computers and Geotechnics*, 623-635. doi:10.1016/S0266-352X(03)00060-0

Dung, P. H. (2010). *"Modelling of Installation Effect of Driven Piles by Hypoplasticity."* Delft: Delft University of Technology. Retrieved from http://resolver.tudelft.nl/uuid:6e96c83c-7116-444f-a011-1cefb52eab5f

Fair, G. M., Hatch, L. P., and Hudson, H. E. (1933). "Fundamental factors governing the stream-line flow of water through sand." *American Water Works Association*, 1551-1565. Retrieved from https://www.jstor.org/stable/41225921

Gambolati, G., Perdon, A. M., and Ricceri, G. (1984). "A Coupled Finite Element Model of Flow in Porous Layered Media." *Finite Elements in Water Resources*, 25-36. doi:10.1007/978-3-662-11744-6_3

Gudehus, G. (1996). "A comprehensive constitutive equation for granular materials." *Soils and Foundations, 36*(1), 1-12. doi:10.3208/sandf.36.1

Gudehus, G. (2011). *"Physical soil mechanics."* Springer-Verlag Berlin Heidelberg. doi:10.1007/978-3-540-36354-5

Hazen, A. (1892). *"Some physical properties of sands and gravels: with special reference to their use in filtration."*

Heeres, O. M. (2001). *"Modern strategies for the numerical modeling of the cyclic and transient behavior of soils."* Delft: Delft University Press. Retrieved from http://resolver.tudelft.nl/uuid:77aea749-0836-49cc-bac6-a8d4ce44962e

Herle, I. (1997). *"Hypoplastizität und granulometrie einfacher korngerüste."* Inst. für Bodenmechanik und Felsmechanik: Karlsruhe

Herle, I. (1997). "Hypoplastizität und Granulometrie einfacher Korngerüste." *Veröffentlichungen des Institutes für Bodenmechanik und Felsmechanik der Universität Fridericiana in Karlsruhe*.

Herle, I. (2008). "On basic features of constitutive models for geomaterials." *Journal of Theoretical and Applied Mechanics, 38*, 61-80.

Herle, I., and Gudehus, G. (1999). "Determination of parameters of a hypoplastic constitutive model from. properties of grain assemblies." *Mechanics of Cohesive-Frictional Materials, 4*, 461-486.

Herle, I., and Mayer, P. M. (2009). "Calculation of deformations of an underwater excavation using parameters of Berlin sand from a hypoplastic model." 75-85. doi:10.1002/bate.200910044

Hofstetter, G., Kolymbas, D., and Gajo, A. (2016). *" EUROMECH Colloquium 572 - Constitutive Modelling of Soil and Rock."* Innsbruck.

Holloer, S. (2006). *"Dynamisches Mehrphasenmodell mit hypoplastischer Materialformulierung der Feststoffphase."* Köln: Rheinisch-Westfälischen Technischen Hochschule Aachen.

Hussain, F., and Nabi, G. (2016). "Empirical formulae evaluation for hydraulic conductivity determination based on grain size analysis." *Pyrex Journal of Research in Environmental Studies*, 26-32.

Idriss, I. M., and Boulanger, R. (2008). *"Soil liquefaction during earthquakes."* Earthquake Engineering Research Institute.

Ishihara, K. (1994). "Review of the predictions for model 1 in the VELACS Program." *Verification of numerical procedures for the analysis of soil liquefaction problems*, 1353-1368.

Ishihara, K., Tatsuoka, F., and Yasuda, S. (1975). "Undrained deformation and liquefaction of sand under cyclic stresses." *Soils and Foundations, 15*(1), 29-44. doi:10.3208/sandf1972.15.29

Jardine, R. J., Symes, M. J., and Burland, J. B. (1984). *The measurement of soil stiffness in the triaxial apparatus* (Vol. 34). Géotechnique. doi:10.1680/geot.1984.34.3.323

Jardine, R. J., Symes, M. J., and Burland, J. B. (1984, September). "The Measurement of soil stiffness in the triaxial apparatus." *Géotechnique, 34*(3), 323-340. doi:10.1680/geot.1984.34.3.323

JGS. (1996). *"Japanese Geotechnical Society, Soil Testing Standards, chapter Test Methods for the Minimum and Maximum Densities of Sands,."*

Kenney, T. C., Lau, D., and Ofoegbu, G. I. (1984). "Permeability of compacted granular materials." *Canadian Geotechnical Journal, 21*, 726-729. doi:http://doi.org/10.1139/t84-080

Kolymbas, D. (1985). "A generalized hypoplastic constitutive law." *Proceedings of the 11th international conference on soil mechanics and foundation engineering.*, Balkema: San Francisco *5*, 2626.

Kolymbas, D. (1993). *"Modern Approaches to Plasticity 1st Edition."* (D. Kolymbas, Ed.) Karlsruhe, Germany. doi:https://doi.org/10.1016/C2009-0-09122-3

Kolymbas, D. (1999). *"Introduction to Hypoplasticity: Advances in Geotechnical Engineering and Tunnelling 1."* New York: Taylor & Francis.

Kolymbas, D., Herle, I., and Von Wolffersdorff, P. A. (1995). "Hypoplastic constitutive equation with back stress." *Numerical and Analytical Methods in Geomechanics, 19*(6), 415-436. doi:10.1002/nag.1610190604

Kozeny, J. (1927). "Uber kapillare leitung des wassers im boden." *Akad. Wiss. Wien*, 271-306.

Kozeny, J. (1927). "Ueber kapillare Leitung des Wassers im Boden." *Sitzungsber Akad. Wiss., Wien*, 271-306.

Lala, A. S. (2017, February). "Modifications to kozeny–carman model to enhance petrophysical relationships." *Solid Earth Discussions*. doi:10.5194/se-2017-8

Lee, K. L., and Seed, H. B. (1967). "Drained strength characteristics of sands." *Journal of the Soil Mechanics and Foundations Division, 93*(6), 117-141.

Lewis, R. W., and Schrefler, B. A. (1998). *"The Finite Element Method in the Static and Dynamic Deformation and Consolidation in Porous Media."* John Wiley & Sons.

Li, C., and Borja, R. I. (2005). *"Finite Element Formulation of Poro-Elasticity Suitable for Large Deformation Dynamic Analysis."* Thesis, Stanford University, Department of Civil and Environmental Engineering, Stanford.

Liang, F., Song, Z., and Jia, Y. (2017). "Hydro-mechanical behaviors of the three-dimensional consolidation of multi-layered soils with compressible constituents." *Ocean Engineering*, 272-282.

Luijendijk, E., and Gleeson, T. (2015, September). "How well can we predict permeability in sedimentary basins? Deriving and evaluating porosity–permeability equations for noncemented sand and clay mixtures." *Geofluids, 15*, 67-83. doi:10.1111/gfl.12115

Malvern, L. E. (1969). *"Introduction to the mechanics of a continuous medium."* New Jersey: Englewood Cliffs, Prentice-Hall.

Martin, G. R., Finn, L., and Seed, H. B. (1975). "Fundamentals of liquefaction under cyclic loading." *Journal of the Geotechnical Engineering Division*, 423-438.

Masin, D. (2012). *"PLAXIS Implementation of Hypoplasticity."* Charles University of Prague

Mašín, D. (2019). *"Modelling of soil behaviour with hypoplasticity."* Springer. doi:10.1007/978-3-030-03976-9

Matsuoka, H., and Nakai, T. (1974, December). "Stress deformation and strength characteristics of soil under three different principal stresses." *Proceedings of the Japanese Society of Civil Engineers*, *232*, 59-70. doi:10.2208/jscej1969.1974.232_59

Meißner, S. (2014). *"Numerische Studien zum in-situ Setzungsverhalten von Gründungssystemen unter zyklischer Einwirkung in nichtbindigen Böden."* Technische Universität Darmstadt: Darmstadt

Meroi, E., and Schrefler, B. A. (1995). "Large Strain Static and Dynamic Hydro-Mechanical Analysis of Porous Media." *Modern Issues in Non-Saturated Soils, 357*, 397-447. doi:10.1007/978-3-7091-2692-9_9

Miura, K., Maeda, K., and Toki, S. (1997). "Method of measurement for the angle of repose of sands." *Soils and Foundations, 37*(2), 89-96. doi:10.3208/sandf.37.2_89

Molenkamp, F., Brinkgreve, R., and Galavi, V. (2010). "Modeling liquefaction behavior of sands by means of hypoplastic model." *Numerical Methods in Geotechnical Engineering (NUMGE)*, Trondheim, Norway, 81-87. doi:10.1201/b10551-16

Nader, J. J. (2012). "A simple model for the small-strain behaviour of soils." doi:2012arXiv1201.0897N

Niemunis, A. (2002). *"Extended hypoplastic models for soils."* Bochum: Inst. für Grundbau und Bodenmechanik.

Niemunis, A., and Herle, I. (1997, December 4). "Hypoplastic model for cohesionless soils with elastic strain range." *Mechanics of Cohesive-frictional Materials, 2*(4), 279-299. doi:10.1002/(SICI)1099-1484(199710)2:4<279::AID-CFM29>3.0.CO;2-8

Niemunis, A., Wichtmann, T., and Triantafyllidis, T. (2005). "A high-cycle accumulation model for sand." *Computers and Geotechnics*, 245-263.

Papadrakakis, M., and Stavroulakis, G. M. (2009). "Solution of large-scale porous media problems." *ECCOMAS Multidisciplinary Jubilee Symposium*, Springer: Dordrecht 79-93. doi:10.1007/978-1-4020-9231-2_6

Pena, A. A., Herrmann, H. J., Lizcano, A., and Alonso-Marroquin, F. (2005). "Investigation of the asymptotic states of granular materials using a discrete model of anisotropic particles." *International Conference on Powders & Grains*, Stuttgart, Germany, 697-700.

Potts, D. M., and Zdravković, L. (1999). *"Finite element analysis in geotechnical engineering: theory."* London: Thomas Telford.

Puzrin, A. (2012). *"Constitutive modelling in geomechanics: Introduction."* Springer-Verlag Berlin Heidelberg. doi:10.1007/978-3-642-27395-7

Qi, J., Wang, S., and Yu, F. (2013). "A review on creep of frozen soils." *Constitutive Modeling of Geomaterials*, 129-133. doi:10.1007/978-3-642-32814-5_13

Ren, X., Zhao, Y., Deng, Q., Kang, J., Li, D., and Wang, D. (2016, November). "A relation of hydraulic conductivity — void ratio for soils based on Kozeny-Carman equation." *Engineering Geology, 213*, 89-97. doi:10.1016/j.enggeo.2016.08.017

Reyes, D. K., Marek, A. R., and Lizcano, A. (2009, January). "A hypoplastic model for site response analysis." *Soil Dynamics and Earthquake Engineering, 29*(1), 173-184. doi:10.1016/j.soildyn.2008.01.003

Runesson, K. (2006). *"Constitutive modeling of engineering materials - Theory and computation (Lecture notes)."* Goteborg: else.

Santamarina, J. C., and Cho, G. C. (2001, June). "Determination of critical state parameters in sandy soils-simple procedure." *Geotechnical Testing Journal, 24*(2), 185-192. doi:10.1520/GTJ11338J

Shahir, H., Pak, A., Taiebat, M., and Jeremić, B. (2012, March). "Evaluation of variation of permeability in liquefiable soil under earthquake loading." *Computer and Geotechnics, 40*, 74-88. doi:10.1016/j.compgeo.2011.10.003

Siu, W., and Lee, S. H. (2004, February). "Transient temperature computation of spheres in three-dimensional random packings." *International Journal of Heat and Mass Transfer, 47*(5), 887-898. doi:10.1016/j.ijheatmasstransfer.2003.08.022

Sturm, H. (2011). "Geotechnical performance of a novel gravity base type shallow foundation for offshore wind turbines." *Geotechnik, 34*(2), 85-96. doi:10.1002/gete.201100013

Stutz, H. H. (2016). *"Hypoplastic models for soil-structure interfaces-modelling and implementation."* Kiel: Kiel University.

Tang, T., and Hededal, O. (2014). "Simulation of pore pressure accumulation under cyclic loading using Finite Volume Method." *8th European Conference on*

Numerical Methods in Geotechnical Engineering, CRC Press: Delft 1301-1306.

Taşan, E. H. (2016). "Zum tragverhalten von suction-buckets unter zyklisch lateralen einwirkungen." *Bauingenieur*, 496-505.

Taşan, H. E. (2011). *"Zur Dimensionierung der Monopile-Gründungen von Offshore-Windenergieanlagen."* Technischen Universität Berlin: Berlin doi:10.14279/depositonce-2786

Tatsuoka, F. (1988). "Some recent developments in triaxial testing systems for cohesionless soils." *Advanced Triaxial Testing of Soil and Rock*, 7-67. doi:10.1520/STP29068S

Tejchman, J. (2008). *"Shear localization in granular bodies with micro-polar hypoplasticity."* Berlin: Springer-Verlag Berlin Heidelberg. doi:10.1007/978-3-540-70555-0

Terzaghi, K., Peck, R. B., and Mesri, G. (1964). *"Soil mechanics in engineering practice."* John Wiley and Son.

Truesdell, C., and Noll, W. (1965). *"The non-linear field theories of mechanics."* Springer Berlin Heidelberg. doi:10.1007/978-3-642-46015-9_1

Truesdell, C., and Noll, W. (1965). *"The non-linear field theories of mechanics."* (S. Flügge, Ed.) Berlin: Springer Verlag.

Ueng, T. S., Wang, Z. F., and Ge, L. (2015). "Tests of permeability in saturated sand during liquefaction." *6th International Conference on Earthquake Geotechnical Engineering.*, Christchurch, New Zealand

Vakili, K. N., Barciaga, T., Lavasan, A. A., and Schanz, T. (2013). "A practical approach to constitutive models for the analysis of geotechnical problems." *The Third International Symposium on Computational Geomechanics (ComGeo III)*, Rhodes, Greece, 738-749.

Viggiani, G., and Atkinson, J. H. (1995). "Interpretation of bender element tests." *Géotechnique, 45*(1), 149-154. doi:10.1680/geot.1995.45.1.149

von Terzaghi, K. (1936). "The shearing resistance of saturated soils and the angle between the planes of shear." *1st International Conference on Soil Mechanics and Foundation Engineering*, Cambridge, *1*, 54-56.

von Wolffersdorff, P. A. (1996, July). "A hypoplastic relation for materials with a predefined limit state surface." *Mechanics of Cohesive-Frictional Materials, 1*(3), 251-271.

von Wolffersdorff, P. A., and R. S. (2009, August). "The Uelzen I Lock – Hypoplastic finite-element analysis of cyclic loading." *Bautechnik*, 64-73. doi:10.1002/bate.200910043

Wichtmann, T. (2005). *"Explicit Accumulation Model for Non-cohesive Soils under Cyclic Loading."* Bochum: Publications of the Institute of Soil Mechanics and Foundation Engineering, Ruhr-University Bochum.

Wichtmann, T. (2016). *"Soil behaviour under cyclic loading: experimental observations, constitutive description and applications."* Karlsruher Institut für Technologie (KIT).

Winde, E. (2015). *"Finite element modelling for earthquake loads on dykes."* Delft: Delft University of Technology. Retrieved from http://resolver.tudelft.nl/uuid:9b83301b-efdc-408c-9d62-5be6a1508e2b

Winde, H. P. (2015). *"Finite element modelling for earthquake loads on dykes."* Delft: Delft University of Technology. Retrieved from http://resolver.tudelft.nl/uuid:9b83301b-efdc-408c-9d62-5be6a1508e2b

Wu, W. (1992). *"Hypoplastizität als mathematisches Modell zum mechanischen Verhalten granularer Stoffe."* Institute of Soil Mechanics and Rock Mechanics, University of Karlsruhe.

Wu, W., and Bauer, E. (1994, December). "A simple hypoplastic constitutive model for sand." *Numerical and Analytical Methods in Geomechanics, 18*(12), 833-862. doi:10.1002/nag.1610181203

Wu, W., Bauer, E., and Kolymbas, D. (1996, May). "Hypoplastic constitutive model with critical state for granular materials." *Mechanics of Materials, 23*(1), 45-69. doi:10.1016/0167-6636(96)00006-3

Wu, W., Bauer, E., Niemunis, A., and Ivo, H. (1993). "Visco-Hypoplastic Models for Cohesive Soils." *Workshop, Modern approaches to plasticity*, Greece, 365-384.

Youd, T. L. (1972). "Compaction of sands by repeated shear straining." *Journal of Soil Mechanics and Foundations*, 709-725.

Yun, T. F., Han, K. N., Li, C. F., and Owen, R. (2008, May). "Discrete thermal element modelling of heat conduction in particle systems: Basic formulations." *Journal of Computational Physics, 227*(10), 5072-5089. doi:10.1016/j.jcp.2008.01.031

Zhao, J., and Shan, T. (2013). "Discrete modeling of fluid-particle interaction in soils." *Constitutive Modeling of Geomaterials*, 297-301. doi:10.1007/978-3-642-32814-5_40

Zienkiewicz, O. C. (1982, August). "Basic formulation of static and dynamic behaviours of soil and other porous media." *Applied Mathematics and Mechanics, 3*(4), 457-468.

Zienkiewicz, O. C., and Shiomi, T. (1984). "Dynamic behaviour of saturated porous media; the generalized Biot formulation and its numerical solution." *International Journal for Numerical and Analytical Methods in Geomechanics, 8*(1), 71-96.

Zienkiewicz, O. C., Chan, A., Pastor, M., and Schrefler, B. A. (1999). *"Computational geomechanics with special reference to earthquake engineering."* John Wiley&Sons.

Zienkiewicz, O. C., Chang, C. T., and Bettess, P. (1980). "Drained, undrained, consolidating and dynamic behaviour assumptions in soils." *Géotechnique*, 385-395. doi:10.1680/geot.1980.30.4.385

Zienkiewicz, O. C., Qu, S., Taylor, R. L., and Nakazawa, S. (1986). "The patch test for mixed formulations." *International Journal for Numerical Methods in Engineering, 23*(10), 1873-1883. doi:10.1002/nme.1620231007

A. Triaxial Test Results

In this part, the undrained cyclic triaxial test data used to calibrate hypoplastic material parameters of the sand are presented. All three triaxial test specimens with different initial relative densities were first consolidated under 150 kPa cell pressure and then sheared with a 50 kPa cyclic deviatoric stress.
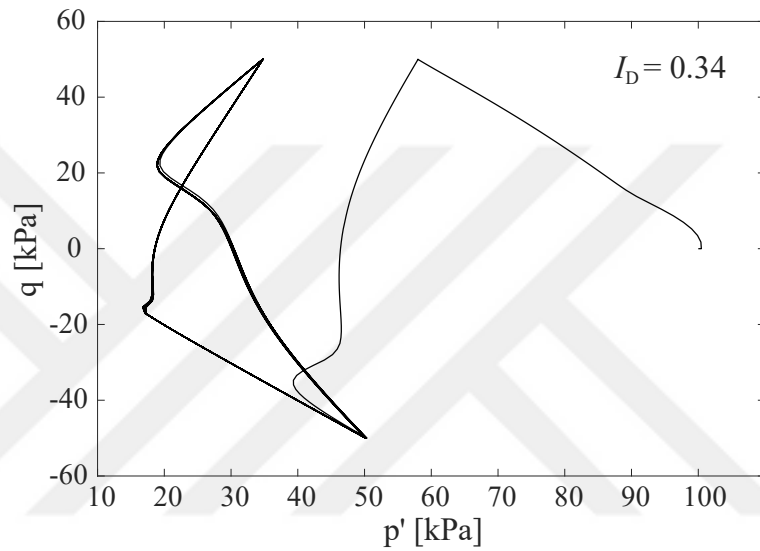

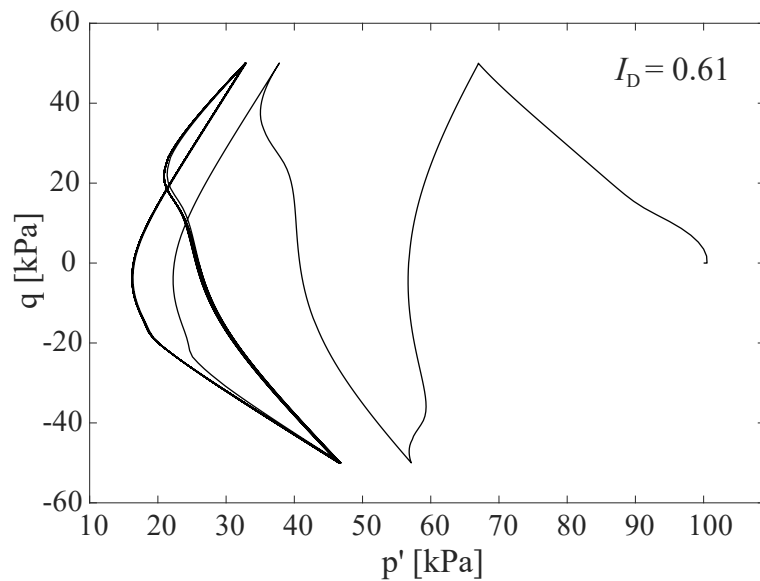*Figure 5.1*. The undrained cyclic triaxial test results with a relative density of 0.34.

Figure 5.2. The undrained cyclic triaxial test results with a relative density of 0.61.
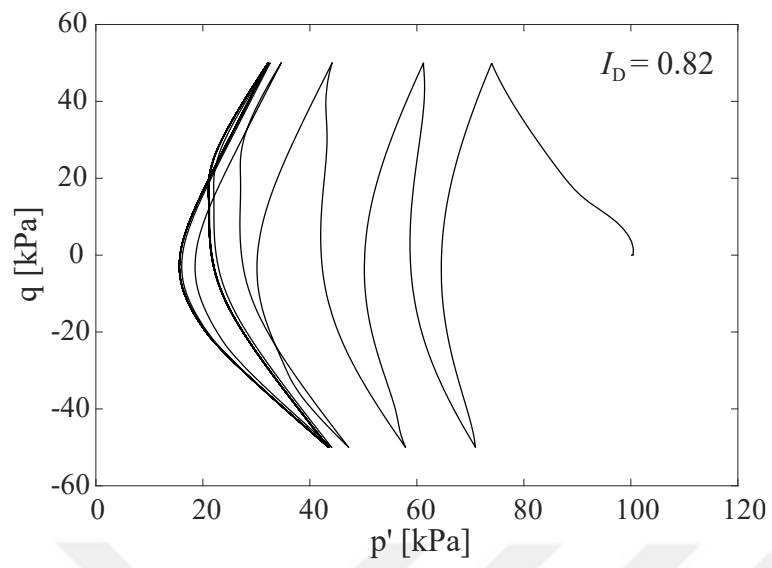
Figure 5.3. The undrained cyclic triaxial test results with a relative density of 0.82.